

## Master Thesis

# An Investigation of the Impact of Feeder Fluctuations on the Content Uniformity of Hot-Melt Extruded Drug Products

Theresa R. Hörmann

---

Institute for Process and Particle Engineering  
Graz University of Technology

Supervisor:

Univ.-Prof. Dipl.-Ing. Dr. techn. Johannes Khinast  
Institute for Process and Particle Engineering

Technical Advisor:

Dipl.-Ing. Daniel Franz Treffer  
Institute for Process and Particle Engineering

Project Advisor:

Dipl.-Ing. Dr. techn. Gerold Koscher  
Research Center Pharmaceutical Engineering GmbH

Graz, 09.Mai 2014

## Abstract

This thesis investigates the extrusion process, which became a well-established manufacturing technology in the pharmaceutical industry over the past few years. High demands in content uniformity, as well as very low API (active pharmaceutical ingredient) concentrations, in many cases, require accurate processes and good process understanding. The critical step concerning content uniformity is the feeding process. As powders exhibit a complex flow behavior, the dosing step shows certain mass flow variability. After the feeder, the powder is processed into a continuous melt stream in different process sections of the extruder. Due to the conveying, kneading and shearing effect of the screws, the material passes through the extruder with a specific residence time distribution (RTD) for a given set-up. Thus, back-mixing compensates the variations of the feeder mass flow to a certain degree. The specific mixing behavior can be derived from the RTD. The RTD depends on the screw design, rotational speed, the total flow rate, the filling ratio and a few more parameters. Thus, the mixing behavior of the extruder is adjustable through process parameters like the screw configuration, throughput and screw rotation speed, for example.

The aim of this work is to describe the dampening behavior based on the RTD, which corresponds to the impulse response and the transfer function of the system. Therefore, three different experiments are conducted with the material system paracetamol – calcium stearate. First, the feeding accuracy is evaluated with catch scale feeding experiments for both feeders, which are used for dosing the pure raw substances in subsequent extrusions. Second, color tracer experiments with video analysis are performed on the extrusion line, in order to receive the RTD of the system. Third, experiments designed especially for system identification purposes are carried out. In the extrusions, the API concentration is determined at the extruder outlet via near-infrared (NIR) spectroscopy and a multivariate data analysis (MVDA) model.

The evaluation of the feeders illustrates inaccuracies typical for feeding powders with poor flow behavior. Especially, bridging in the hopper and its effects are discussed on the basis of experimental data. The feeder accuracy is found to be rather good, looking at the feed rates displayed by the feeders. The feed rates calculated from the weight increase on the catch scales, on the other hand, point out significant discrepancies to the displayed feed rates. Hence, measurement uncertainties like the dynamic behavior of the scale and the influence of sampling rate and scale resolution on the results are discussed.

The color tracer experiment reveals a dependency of the RTD on the API content in the melt. The Peclet number derived from the fitting procedure with the axial dispersion model identified medium to intensive dispersive mixing in the extruder. System identification was carried out using data from the color tracer experiment and delivered a Box-Jenkins transfer function model. In order to compare this model to the RTD model, they were both used to simulate the output API concentration for the data set originally designed for system identification. The result of both simulations showed good accordance to the experimental data.

The shown methodology enables description of the complex mixing during extrusion with simple models and key figures. The key figures can be used to compare screw designs quantitatively and to adapt them for known feeder accuracies. The mixing models can be applied to predict the product concentration for fluctuating input concentrations. Both, can be utilized for process development and control purposes.

## Zusammenfassung

Diese Arbeit befasst sich mit der Schmelzextrusion, die sich innerhalb der letzten Jahre als Herstellungsprozess für pharmazeutische Produkte etabliert hat. Die hohen Qualitätsansprüche bezüglich exakter Wirkstoffmengen, sowie häufig sehr geringe Mengen, verlangen präzise Prozesse und fundiertes Prozessverständnis. Der kritische Prozessschritt für konstante Wirkstoffmengen ist das Dosieren. Da Pulver ein komplexes Fließverhalten aufweisen, liegen gewisse Dosierschwankungen in der Natur des Prozesses. Nach dem Eindosieren in den Extruder wird das Pulver über verschiedene Verfahrenszonen hinweg in einen kontinuierlichen Schmelzestrom verarbeitet. Aufgrund der Förder-, Knet- und Scherwirkung der Extruderschnecken, durchläuft das Material den Extruder mit einer spezifischen Verweilzeitverteilung (VZV). Folglich, kann Rückvermischung Dosierschwankungen gewissen Ausmaßes kompensieren. Ausgehend von der VZV ist es möglich dieses spezifische Mischverhalten abzuleiten. Die VZV wird, unter anderem, vom Schneckendesign, von der Schneckendrehzahl, dem Gesamtdurchsatz und dem Füllgrad bestimmt. Folglich, kann das Mischverhalten eines Extruders anhand von Prozessparametern, wie der Schneckenkonfiguration, dem Durchsatz, oder der Schneckendrehzahl eingestellt werden.

Ziel dieser Arbeit ist es, das Mischverhalten anhand der VZV, welche der Impulsantwort, sowie der Übertragungsfunktion des Prozesses entspricht, zu beschreiben. Dafür werden drei Experimente mit dem Stoffsystem Paracetamol - Calciumstearat durchgeführt. Zuerst wird die Genauigkeit beider Dosierer, welche für die Dosierung der Reinstoffe in den Extrusionen eingesetzt werden, in Feedingversuchen mit einer Auffangwaage untersucht. Zweitens, werden Farbtracerversuche am Extruder durchgeführt und per Videoanalyse ausgewertet, um die VZV des Systems zu erhalten. Drittens, werden Experimente designt, die den Anforderungen der Systemidentifikation entsprechen. Während der Extrusionen wird die Wirkstoffkonzentration am Ende des Extruders mit Hilfe von NIR Spektroskopie und einem Multivariate Data Analysis Modell bestimmt.

Die Auswertung der Feedingversuche zeigt Dosierungenauigkeiten auf, welche für das Dosieren von Pulvern mit schlechtem Fließverhalten üblich sind. Besonders Brückenbildung in der Dosiervorlage und deren Auswirkung wird anhand der experimentellen Daten diskutiert. Ausgehend von den, am Dosierer angezeigten Förderraten wird die Dosiergenauigkeit als gut eingestuft. Die, aus der Gewichtszunahme auf der Waage errechneten Förderraten hingegen, weisen hohe Abweichungen dazu auf. Es werden Messunsicherheiten wie das dynamische Verhalten der Waagen und der Einfluss von Abtastfrequenz und Waagenpräzision erörtert.

Der Farbtracerversuch macht einen Zusammenhang zwischen der VZV und dem Wirkstoffanteil sichtbar. Die Peclet Zahlen aus den Fits mit dem Axial-Dispersionsmodell, weisen darauf hin, dass mittleres bis intensives dispersives Mischen stattfindet. Die Systemidentifikation mit den Daten aus dem Farbtracerversuch durchgeführt und liefert ein Box-Jenkins Übertragungsfunktionsmodell. Um dieses Modell mit dem VZV-Modell vergleichen zu können, werden beide verwendet, um die Wirkstoffkonzentration am Austritt für den ursprünglichen Systemidentifikationsdatensatz zu simulieren. Das Ergebnis beider Simulationen wies gute Übereinstimmung zu den experimentellen Daten auf.

Die gezeigte Methodik ermöglicht die Beschreibung des komplexen Mischverhaltens im Extruder anhand von einfachen Modellen und Kennzahlen. Die Kennzahlen können genutzt werden um Schneckenkonfigurationen quantitativ zu vergleichen und diese für gegebene Dosiergenauigkeiten anzupassen. Die Modelle ermöglichen die Vorhersage der Produktzusammensetzung unter dem Einfluss von Dosierschwankungen. Die Anwendung der Ergebnisse kann in den Bereichen Prozessentwicklung und Kontrolle erfolgen.

Deutsche Fassung:  
Beschluss der Curricula-Kommission für Bachelor-, Master- und Diplomstudien vom 10.11.2008  
Genehmigung des Senates am 1.12.2008

## EIDESSTATTLICHE ERKLÄRUNG

Ich erkläre an Eides statt, dass ich die vorliegende Arbeit selbstständig verfasst, andere als die angegebenen Quellen/Hilfsmittel nicht benutzt, und die den benutzten Quellen wörtlich und inhaltlich entnommenen Stellen als solche kenntlich gemacht habe.

Graz, am .....

.....

(Unterschrift)

Englische Fassung:

## STATUTORY DECLARATION

I declare that I have authored this thesis independently, that I have not used other than the declared sources / resources, and that I have explicitly marked all material which has been quoted either literally or by content from the used sources.

.....

date

.....

(signature)

## **Acknowledgement**

First of all, I want to thank my technical supervisor Daniel Treffer for his extraordinary support and the freedom he gave me during my thesis. His trust in my abilities and way to think out of the box gives me the courage to be creative in my work. Moreover, I want to thank Daniel Markl, Patrick Wahl and Andreas Eitzlmayr, who supported me with their knowledge and help. Also, I am very grateful to be part of the extrusion team at the RCPE because working with them is always a great time.

Finally, I want to thank my family for keeping me grounded all the time and for standing behind me in all my plans.

# Table of Content

1	Introduction.....	1
1.1	Special Features of the Pharmaceutical Industry .....	2
1.1.1	Process Analytical Technology (PAT).....	3
1.2	Evaluation of Mixing in an Extrusion Process.....	5
1.3	Aim of this work .....	9
2	Theory and Literature Review .....	10
2.1	The Extrusion Process.....	10
2.1.1	The Dosing Unit.....	11
2.1.2	The Extruder .....	13
2.1.3	The Downstream Processing Unit.....	24
2.1.4	Process Monitoring System .....	24
2.2	System Identification .....	26
2.2.1	Process Parameters in the Extrusion Process .....	28
2.2.2	Requirements on System Identification Experiments .....	29
2.2.3	Relevant Models .....	29
3	Materials, Methods and Experimental Design .....	37
3.1	Materials .....	37
3.2	Methods and Process Equipment .....	37
3.2.1	Extruder.....	37
3.2.2	Light Microscopy.....	39
3.2.3	Catch Scale for Feeder Evaluation.....	39
3.2.4	Real-Time Monitoring of the Experiments .....	40
3.2.5	NIR Spectroscopy .....	40
3.2.6	Chemometric Model .....	40
3.2.7	Optical RTD Measurements.....	41
3.2.8	Data Analysis and System Identification .....	42
3.3	Experimental Design.....	43
3.3.1	Feeding Experiments.....	43
3.3.2	Extrusion Step-Change Experiment.....	44
3.3.3	System Identification Experiment.....	45

4	Results and Discussion .....	46
4.1	Feeding Experiments .....	46
4.1.1	Matrix Feeder (Ktron KT20).....	46
4.1.2	API Feeder (Brabender MT-S Hyg).....	51
4.2	Extrusion Step-Change Experiment.....	54
4.3	System Identification Experiment.....	63
4.4	Comparison and Discussion.....	70
5	Summary and Conclusions.....	72
6	Appendix.....	74
6.1	List of Tables .....	74
6.2	List of Equations .....	74
6.3	Literature.....	75

## Table of Figures

Figure 1: Schematic presentation of a twin-screw extruder set-up with possible application of PAT tools (adapted from [9]).....	3
Figure 2: Schematic integration of the extruder and additional sensors in SIPAT [12] .....	4
Figure 3: Influence of sample size on the relative standard deviation [13] .....	4
Figure 4: Possible integration of the extrusion process into a pharmaceutical manufacturing line [33] ....	10
Figure 5: Dosing accuracy with tolerance band (according to [34]).....	11
Figure 6: Sketch of a loss-in-weight feeder .....	12
Figure 7: Effect of ideal mixing behavior in an extruder on fluctuating inlet concentrations .....	13
Figure 8: Classification of extruders [8] .....	14
Figure 9: Processing zones illustrated along a specific screw configuration, adapted from [8] .....	14
Figure 10: Extrusion screw geometry [38] .....	15
Figure 11: Conveying elements with different pitch size, conveying direction (forward, forward, backward) .....	16
Figure 12: Kneading elements with identical disc widths, but varying pitch sizes, and conveying directions (forward, backward, neutral).....	16
Figure 13: Mixing elements with different pitch sizes.....	16
Figure 14: Illustration of an intake zone .....	16
Figure 15: Kneading blocks in a plastification zone.....	17
Figure 16: Conveying elements with different pitches in a melt conveying zone .....	17
Figure 17: Conveying (dark blue) and re-conveying (light blue) kneading elements with different disc widths in a mixing zone .....	17
Figure 18: Dispersive and distributive mixing [40] .....	18
Figure 19: Example of dispersive and distributive mixing elements [41] .....	18
Figure 20: Conveying elements with big pitch in a devolatilization zone .....	18
Figure 21: Illustration of a pressure build-up zone before the die plate .....	19
Figure 22: Residence time distributions for different screw configurations .....	19
Figure 23: Residence time density function with dead time and tailing .....	20
Figure 24: Step response with characteristic parameters [8] .....	23
Figure 25: A schematic showing the balance of energy input and heat history with the extreme combinations of these, resulting in either degradation or inhomogenous material (adapted from [4]).....	23
Figure 26: Several downstream processing options for an extrusion line (adapted from [43]) .....	24
Figure 27: Schematic of a basic data acquisition and process control system for a continuous manufacturing line consisting of several processes (i. e., feeding, extrusion, downstream, etc.) [43] .....	25
Figure 28: The system identification loop, adapted from [48].....	27
Figure 29: Input and output parameters for the extrusion process, adapted from [8] .....	28
Figure 30: Every response can be regarded as a series of impulse responses.....	30
Figure 31: The process model containing the feeder, extruder and NIR estimation model [8] .....	31
Figure 32: Identification and prediction stage of the chemometric model [8].....	32
Figure 33: Process model in identification and prediction stage [8].....	33
Figure 34: Illustration of the experimental set-up.....	38

Figure 35: Die section of the extruder where a NIR probe is situated. The black flow profile represents the pressure-driven pipe flow of a Newtonian melt with the maximal velocity $u_{\max}$ in the center. The red velocity profile represents the case of perfect plug flow with $u_{\text{av}}$ . (adapted from [29])	39
Figure 36: Modification of the die section and probe: (A) Filling the large melt volume with a tapered metal cylinder (“Apollo” capsule, radius $R_i$ ) forming an annular channel at the walls. (B) Turning the 45° face of the probe 1 mm to ensure a nearly planar transition between the probe and the barrel wall. (C) This leads to an annular flow of the melt [29]	39
Figure 37: Set-up for feeding experiments	40
Figure 38: PC1 and PC2 of the model spectra. The PCA was performed in the same spectral range as the model [29]	41
Figure 39: Chemometric model in [29] from 0 to 60 % API (paracetamol) content in the melt with $R^2=0.999$ (black), $Q^2=0.974$ (blue) and four latent variables. Due to the non-linear behavior at a low API content, the cross validation (blue) of the 0% group failed.	41
Figure 40: Set-up for optical RTD measurements	41
Figure 41: Color tracer experiment with 20% API content and the outlet valve open	42
Figure 42: Experimental design for feeding experiments	44
Figure 43: Step experiment design for color tracer experiments with simultaneous NIR estimation	44
Figure 44: Experimental design for system identification	45
Figure 45: Matrix feeder and catch scale data comparison including set-point and 5% tolerance band	47
Figure 46: Boxplots for each feed rate level (5 s smoothing) for the matrix feeder	48
Figure 47: Frequency analysis of the matrix feeding signal for steps one (0.4 kg/h) to four (0.25 kg/h)	50
Figure 48: API feeder and catch scale data comparison including set-point and 5% tolerance band	51
Figure 49: Cohesive powders tend to build bridges in the hopper, causing formation of an empty hole around the agitator	52
Figure 50: Boxplots for each federate level for the API feeder	52
Figure 51: Frequency analysis of the API feeding signal for steps one (0.1 kg/h) to four (0.25 kg/h)	54
Figure 52: Fit and detected RTD curves during different step changes	55
Figure 53: Fit and detected RTD curves for different API concentrations	55
Figure 54: Comparison of RTD curves during different step changes	55
Figure 55: Comparison of RTD curves for different API concentrations	55
Figure 56: Influence of the Peclet number ( $Pe$ ) on the shape of the model curve ( $\theta$ = dimensionless time, $\tau$ = mean residence time, $t$ = time, $C_\theta$ = tracer concentration)	57
Figure 57: Overview of the extrusion run with color tracer experiments	58
Figure 58: Boxplots for the API concentration calculated from the feeder’s displayed feed rates, the API concentration estimated by NIR spectroscopy, the pressure and the torque during the experiments	59
Figure 59: Paracetamol crystals, raw material (50 x)	60
Figure 60: Extrudate with 20% paracetamol (50 x)	60
Figure 61: The axial dispersion model fits (blue) to concentration step changes from the experiment (red)	61
Figure 62: Overview of the system identification experiment	63
Figure 63: Color tracer experiment used for system identification	64

Figure 64: Identification (left) and validation (right) data sets for system identification with the input $u_1$ being the API concentration as indicated by the feeders and the output $y_1$ the concentration estimated via NIR at the extruder outlet .....	65
Figure 65: Process time delay estimation by performing correlation analysis .....	65
Figure 66: The ARMAX model with the model order selected using the AIC and the “best-fit” criterion used for simulating the output of the validation data set .....	66
Figure 67: Simulated output for the dynamic and the disturbance ARMAX models .....	67
Figure 68: The Box-Jenkins model with the model order selected using the AIC and the “best-fit” criterion used for simulating the output of the validation data set .....	68
Figure 69: Simulated output for the dynamic and the disturbance Box-Jenkins models .....	69
Figure 70: Comparison of modeling approach using the RTD and a Box-Jenkins model without the disturbance model .....	70

## List of Abbreviations

FDA	Food and Drug Association
GMP	Good Manufacturing Practice
HME	Hot-Melt Extrusion
CU	Content Uniformity
PAT	Process Analytical Technology
QbD	Quality by Design
EMA	European Medicines Agency
API	Active Pharmaceutical Ingredient
AV	Acceptance Value
TPP	Target Product Profile
NIR	Near-Infrared (spectroscopy)
GC	Gas Chromatography
SWAXS	Small and Wide Angle X-Ray Scattering
HPLC	High-Performance Liquid Chromatography
CQA	Critical Quality Attributes
VRR	Variance Reduction Ratio
RTD	Residence Time Distribution
PFR	Plug Flow Reactor
CSTR	Continuous Stirred-Tank Reactor
FOPDT	First-Order Plus Dead Time (model)
SE	Specific Energy (input)
RVD	Residence-Volume Distribution
RRD	Residence-Revolution Distribution
MVDA	MultiVariate Data Analysis
MRT	Mean Residence Time

OPC	Object linking and embedding for Process Control
LTI	Linear Time Invariant
ARMAX	Auto Regressive Moving Average models with eXternal input
AIC	Akaike's Information Criterion
YIC	Young's Information Criterion
MIMO	Multiple-Input Multiple-Output
SISO	Single-Input Single-Output
PRBS	Pseudo Random Binary Sequence
SNR	Signal-to-Noise Ratio
PCA	Principal Component Analysis
PLS-R	Partial Least Square Regression
SNV	Standard Normal Variate
RGB	red-green-blue
Pe	Peclet number
CaSt	Calcium Stearate
IQR	Interquartile Range
DT	Dead Time

# 1 Introduction

Since the US *Food and Drug Association* (FDA) published a new framework for *Good Manufacturing Practice* (GMP) in 2004 [1], the pharmaceutical industry undergoes a drastic change. With this framework, the FDA switched direction away from batch processing and opened the door to continuous manufacturing in the pharmaceutical industry. With that change began the rise of the *Hot-Melt Extrusion* (HME) technology for solid drug manufacturing. McKelvey et al. [2] state that almost every major pharmaceutical company invests in development of solid solution formulations. Among other motivations, a shift of promising drug substances to less soluble drugs, patent expiry and established equipment vendors for pharmaceutical melt extruders are given as factors, besides the shift in the manufacturing philosophy of the FDA and industry.

Since the last three decades a steady improvement of extrusion manufacturing processes and monitoring strategies and tools took place. Recently, Repka et al. [3] published an extensive work about melt extrusion in the pharmaceutical sciences. It covers the manifold applications for extrusion with its advantages and challenges. A main advantage is the ability to produce molecular dispersions with enhanced bioavailability. Another advantage of the extrusion technology is its compact design, incorporating solid dispersion mixing, metering, blending, melting and shaping in one step. Therefore, it is possible to have only one production step from the raw materials to the finished dosage form. In order to meet the quality specifications concerning *Content Uniformity* (CU) of a pharmaceutical product, the powder feeding process becomes a crucial step.

To meet quality specifications from the regulatory agencies good process understanding and tight process control are necessary. Within the framework, the FDA also promoted the *Process Analytical Technology* (PAT) initiative. This is a guideline away from end-of-pipe testing toward built-in quality (*Quality by Design*, QbD) using new in-line monitoring methods of key parameters. These emerging manufacturing methods, combined with the PAT tools became a new platform technology for the pharmaceutical industry [4]. Still there are many challenges, which have to be overcome. Accurate and consistent powder feeding with relatively small feed rates is one of those challenges. Due to the often difficult flow behavior of pharmaceutical powders, sophisticated feeding strategies have to be applied. The extrusion process is insensitive to high frequency variations in the feed stream, because of its back-mixing capability. Slow drifting or oscillations, however, cannot be evened out. In order to control and predict product quality, the behavior of the feeding system and the characteristic mixing capability of an extrusion line must be evaluated according to the requirements of the regulatory agencies.

## 1.1 Special Features of the Pharmaceutical Industry

As the pharmaceutical industry supplies people with products that can be harmful as well as healing, it is monitored and controlled very strictly. This causes a conservative mindset and strict manufacturing restrictions compared to other industry branches [5]. These special requirements concern purity in the process as well as very consistent product.

Controlling organs are e.g. the FDA in the United States of America and the *European Medicines Agency* (EMA) in Europe. These organs define technical guidelines and award admissions for new pharmaceuticals. One such guideline is the GMP framework for manufacturing. Definitions concerning pharmaceutical standards for substances and dosage forms can be found in the European Pharmacopoeia.

One part of the European Pharmacopoeia deals with testing the constancy of the concentration of an active substance in pharmaceuticals (Active Pharmaceutical Ingredient – API) in different dosage units. The “UNIFORMITY OF DOSAGE UNITS” (04/2012:20940) section in the European Pharmacopoeia 7.8 defines the test method for CU tests of dosage units. Moreover, definitions for the term dosage units and CU are given. According to this section, a dosage unit is a dosage form where each dosage unit contains a single dose, or part of a dose of an active substance. The “uniformity of dosage units” means the degree of uniformity concerning the amount of active substance among the dosage units [6]. The Pharmacopoeia gives a detailed instruction on how this property has to be tested.

The CU can be demonstrated in two ways: either using the content uniformity method or the mass variation method. The content uniformity method can be applied for all dosage forms, the mass variation method only for several defined dosage forms. For the content uniformity method, a minimum of 30 units must be selected. Then the procedure for the accordant dosage form follows. For solid dosage forms 10 units must be analyzed with an appropriate method. The result of the test is an *Acceptance Value* (AV). The AV gives the averaged deviation for the analyzed units. This value must be below 0.15, if no other specification is given. If this test fails, the remaining 20 units must also be analyzed. The requirements for the second test are met, when the final AV is again equal to, or below 0.15. Moreover, no individual unit is allowed to be outside the range of 0.75 to 1.25 times the target value. Thus, there are three critical main factors investigated: the mean of the samples, the individual deviation for each tablet and, especially in process development, also the coefficient of variation [7].

These tests are performed to check the CU in every batch of drugs. While this is a method to ensure that no failed batch is brought to the market, it does not contain any information about the process itself. The testing is only product focused. These standards represent the traditional approach of quality assurance in the pharmaceutical industry. With the PAT initiative the testing becomes process-focused. Through enhanced process understanding and tight process control, product quality becomes the result of a well-managed process.

### 1.1.1 Process Analytical Technology (PAT)

The PAT initiative promotes several tools for full quality control of materials and processes, in order to guarantee a final *Target Product Profile* (TPP). The measurements are carried out in real-time and contain univariate (e.g., temperature, pressure), or multivariate (e.g., spectra) data. Some attributes can be measured directly and others only indirectly via combinations of direct measurements. Common PAT tools are listed below [8]:

- Direct Measurements:
  - *Near-Infrared* (NIR) Spectroscopy
  - Raman Spectroscopy
  - Chemical Mapping
  - UV-Vis Spectroscopy
  - Mass Spectroscopy
  - *Gas Chromatography* (GC)
  - *Small and Wide Angle X-Ray Scattering* (SWAXS)
  - Terahertz Spectroscopy
  - Optical Coherence Tomography
  - *High-Performance Liquid Chromatography* (HPLC)
- Indirect Measurements:
  - Generic Sensors
    - \* Physical Attributes (size, shape, temperature, pressure, etc.)
    - \* Chemical attributes (pH value, etc.)

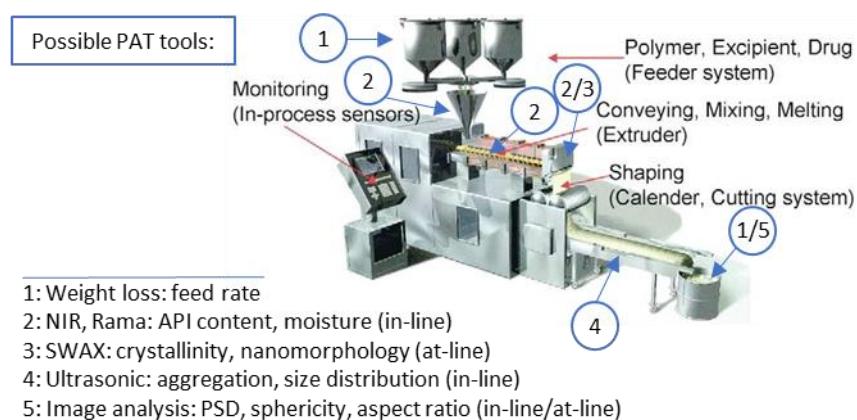


**Figure 1: Schematic presentation of a twin-screw extruder set-up with possible application of PAT tools (adapted from [9])**

Figure 1 illustrates several possible applications of PAT tools in an extrusion process.

The integration of the tools into one overall data acquisition system is essential in order to enable time-aligned, immediate analysis and control of the process.

Siemens developed a PAT software solution, called SIPAT (Siemens AG, Belgium). It allows monitoring and identification of *Critical Quality Attributes* (CQA) in the process, as well as process control, prediction and optimization. Data from different sensors is collected and time-aligned to a chosen reference collector via an aggregation function on the data. Integration of sensors from different manufacturers is possible,

because it offers standardized communication interfaces (e.g., OPC technology) as well as customized communication interfaces (Figure 2). Moreover, SIPAT is able to integrate in-line, at-line, on-line and off-line data [10], [11].

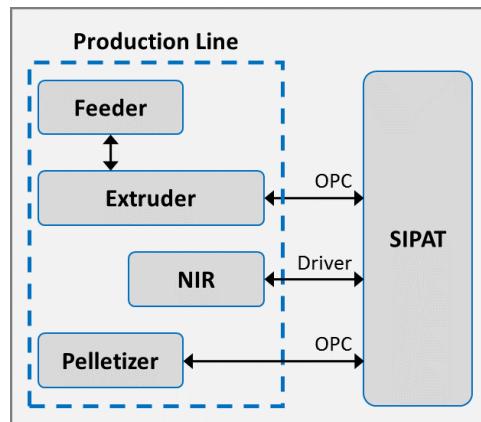


Figure 2: Schematic integration of the extruder and additional sensors in SIPAT [12]

The advantage of PAT tools is the possibility to measure CU continuously. In that way problems in evaluating CU, like scrutiny of scale are overcome. Scrutiny of scale means, that the scale of the analyzed unit determines the relevance of the measurement (Figure 3). It is not useful to measure the API content averaged over a whole batch ( $m_s = 64$ ), for example, because this gives no information about the uniformity in smaller scales. Also, analysis of single particles ( $m_s = 1$ ) is not sensible, because the scale resolution is too big. Therefore, the sample size should match the product size.

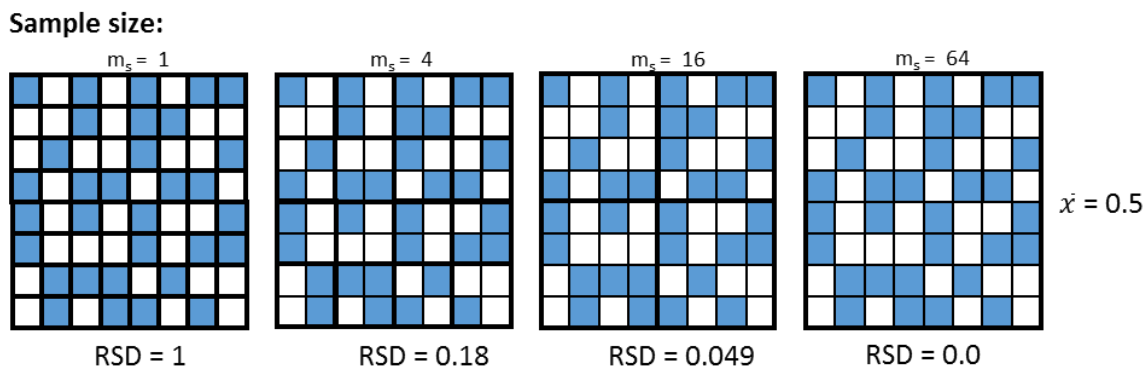


Figure 3: Influence of sample size on the relative standard deviation [13]

Still, there are challenges also in continuous in-line measurements. NIR spectroscopy is only able to measure the spectra for a certain sampling volume depending on optical properties of the material. Thus, the sampling position is crucial. In extrusion processes, for example, the material exchange at the walls in a pipe flow is limited due to laminar flow regime. Ideal sampling would be done over the whole cross-section, a segment of the cross-section, or at least over the whole circumference of the inner barrel wall, but the NIR probes are only able to detect spectra directly in front of the probe at the wall. Also, the integration time for the spectra is a trade-off between high resolution for fluctuations and noise reduction.

## 1.2 Evaluation of Mixing in an Extrusion Process

The target of a mixing process is to provide a product with homogenous composition. In solid drug production this means that powders should be blended in a way that the desired mixture quality is reached. Furthermore, time stability of the mixing process is required and sensitivity to process perturbations should be known [7].

A traditional approach to evaluating CU after mixing steps is to perform a statistical analysis of concentration fluctuations in several samples. In 1948, Beaudry [14] defined the mixing efficiency for continuous blenders using the *Variance Reduction Ratio* (VRR). This sets the variance of input streams in relation to the variance of output streams. Moreover, the mean value for a test run and deviations from the target value for each sample are evaluated according to specifications from regulating agencies [7], [15]. This approach is only suitable to evaluating a mixing process, but neither offers a contribution to better process understanding, nor facilitates process control. Danckwerts [16] introduced the idea of characterizing continuous flow systems with an axial dispersion model using the *Residence Time Distribution* (RTD) in 1953. The RTD evaluates the axial mixing capability of a system. The characteristics of experimental RTD curves can be linked to delay and dead volume models connecting *plug flow reactor* (PFR) and *continuous stirred-tank reactor* (CSTR) units in a system [17], or to dispersion models [18]–[20], for example. In general there are two approaches to modeling the RTD: theoretical (mechanistic), or empirical models. While theoretical models possess the advantage to provide insight in basic mechanisms of the process, empirical models usually permit easy application of mathematical tools, like convolution, to control and predict process outcome. Pernenkil and Cooney [21] published a review about continuous blending of powders in 2006. As the characterization of the mixing behavior in the extruder can be done analogue to the evaluation methods for powder blenders, and Pernenkil and Cooney gives a nice overview of the approaches reported in literature so far (Table 1).

**Table 1 Theoretical modeling methodologies for continuous blending.** [21]

<b>Objective</b>	<b>Method</b>	<b>Comments</b>	<b>References</b>
Performance of blenders	Mass balance on continuous blenders based on pulsed inputs is used in a statistical formulation	Gives an index of performance of semi-continuous and continuous blenders.	Baudry (1948)
Characterization of mixing processes	Mass balance on continuously operated vessel with impulse and step inputs	Defines segregation mathematically. Explanation of the intensity and scale of scrutiny discussed.	Danckwerts and Sellers (1951)
Performance of continuous blenders	Response stimulus method	An expression for performance of a mixer based on fraction of mixer acting ideally was derived and phenomenological explanations were not provided.	Williams and Rahman (1971)
Improvement over batch blending	Statistical analysis	Theoretical performance of semi-continuous blending operation was derived and found to be two times that of a batch blender. Moreover, ironing out of the batch to batch variations reduces the volume of failed product units considerably.	Goldsmith (1966)
Characterization of the random variations in a blender output	Power density spectrum analysis, variographic analysis	The assumption of VRR of a continuous blender to be the sum of a random background band limited white noise and a reduction variance of the feed induced fluctuations was theoretically and experimentally justified.	Ghaderi (2003), Weinekötter and Reh (1995)
Characterization of blender performance using a dispersion model	Stimulus response analysis: RTD analysis	A dispersion model for free-flowing powders in continuous blenders was developed based on the continuum approximation. This approximation relies on the diffusion mechanism of the powder in the free surface and the dilation on the part of the mixture due to agitation.	Sherrit et al. (2003), Sudah et al. (2002)

<p>Characterization of a blender using a Fokker – Planck model</p>	<p>Stimulus response analysis: RTD analysis</p>	<p>Fokker-Planck equations were used to determine the output concentration distribution for an impulse input and this was related to the residence time distribution and its statistical moments.</p> <p>Fokker-Planck equations were used to determine the random mixing of powders. The same theory was used to define segregations kinetics during mixing.</p> <p>Two Fokker-Planck equations were solved numerically for two components. One component was fed sinusoidally to control the disturbance entering the blender. Ratio of the feed disturbance was found to be a critical parameter.</p>	<p>Molerus (1966)</p> <p>Sommer (1981)</p> <p>Kehlenbeck and Sommer (2003)</p>
<p>Blending modeling using Markov Chains</p>	<p>Markov Chains</p>	<p>The blender was modeled as a Markov process. The transition probabilities for the blenders used by Weinekotter and Reh (1995) was used in determining the transition probability matrix. The design of the outlet along with the residence time and time period of oscillation of the feed were found to be critical parameters.</p>	<p>Berthiaux et al. (2004)</p>

A general observation from the mixing models is that mixers act as low-pass filters. This means, that high frequency fluctuations in the inlet stream can be evened out, while slow changes pass on to the outlet.

These findings are also applicable to extrusion processes. RTD-based characterization methods are common for evaluating the dampening behavior of extruders. In 1991, Curry, Kiani and Dreiblatt [22] investigated the dampening of feed variations for a plasticizing compounding extruder using transfer functions. Also for applications in the food industry, system identification approaches are used [23], [24] to regulate certain product properties, like extrudate density, or water content, for example. In pharmaceutical applications McKelvey et al. [2] (2007) modeled the step responses of an extruder using a *First-Order Plus Dead Time* (FOPDT) model. Then model predictive process monitoring was implemented performing numerical convolution of time-discretized inputs with the differential form of the FOPDT model. In a second step, the experimental RTD was determined using NIR spectroscopy and the FOPDT model in the approach was replaced by the experimental RTD, in order to evaluate the dampening ability of feeder input noise. Troup et al. [25] (2011) also used NIR measurements for process model identification and to understand disturbance rejection capabilities. The disturbance rejection capability was determined by calculating the periodogram of the time derivative of the identified FOPDT process model. A critical frequency of 0.05 cycles/second was found, above which fluctuations are dampened for the exemplary extruder set-up (extruder, screw configuration, throughput, etc.).

Several methods to measure the experimental RTD are reported in literature. If the RTD is used to investigate the influence of process parameters, usually tracer pulse experiments [26], [27], [28], or washout experiments [17] for different configurations are performed. Then the shape of the curve and the time constants for the model are compared. Throughput, screw speed and screw configuration were identified as the most influential process parameters on the RTD. If the RTD is used for system identification approaches in order to extract the transfer function to facilitate a process control application step-change experiments [29], [8], [22], [2], or sinusoidal excitation signals [22] are also used.

In 2012 Gao et al. [30] published a review of RTD applications in solid unit operations. Two kinds of tracer detection methods applied: in-line and off-line detection. In-line methods are optical, thermal or electrical signals from inline probes (e.g., NIR spectroscopy). Off-line methods (e.g., optical RTD measurement using digital imaging) are used when sample acquisition, signal conversion, or data storage cannot be performed with sufficient velocity.

Besides evaluating the mixing capability, the RTD also allows to evaluate *Specific Energy* (SE) input for the extruded material. With this knowledge, the process can be designed to minimize degradation of sensitive material [31].

Gao, Walsh and Bigio [32] extended the RTD concept by introducing a *Residence-Volume Distribution* (RVD) and *Residence-Revolution Distribution* (RRD), which makes the RTD independent of material properties, as well as operating conditions and provides a single master curve for a certain screw configuration.

### 1.3 Aim of this work

This introduction gave a rough overview over the manufacturing environment in the pharmaceutical industry. Moreover, an overview of modeling approaches for mixing processes in general and extrusion in particular are given. The following sections will go into functionalities and individual processing tasks of extrusion lines. Especially the extruder and its processing zones will be treated. Characteristics and process parameters will be given and their interpretation discussed. The models chosen from literature to estimate mixing are reviewed and discussed regarding advantages and disadvantages.

The aim of this work is to describe the dampening behavior of the process based on the RTD. The RTD corresponds to the system's impulse response and transfer function. This shall enable the prediction of the output API concentration for given feed rates in future applications. The API concentration during step changes is determined at the extruder outlet via NIR spectroscopy and a *Multivariate Data Analysis* (MVDA) model. Moreover, optical RTD measurements are performed using color tracer and video analysis. The resulting RTDs from both methods are compared.

Therefore, three different experiments are conducted. First, the feeders' performance is evaluated in feeding experiments using a catch scale. Second, color tracer experiments are performed, in order to receive the RTD over several concentration levels. Third, an experiment is done using an experimental design taking into account especially the requirements for system identification.

Then, the characteristic dampening behavior is obtained using two different approaches. The first approach uses the averaged RTD from the color tracer experiments to predict the output variation via numerical convolution. The second approach derives the transfer function, using the MATLAB toolbox system identification to identify a data-based linear process model. The approaches will be validated by comparing simulated and experimental data.

## 2 Theory and Literature Review

This chapter provides the reader with fundamental knowledge of the investigated subject and shall help to understand the subsequent investigations. The first section of this chapter discusses the extrusion process. Individual processing steps, like dosing, processing and downstream processing are introduced. The mechanisms and influential parameters for each unit are given and characterization concepts from the literature reviewed. In addition, a process monitoring system is introduced at the end.

The second section of this chapter introduces the idea of system identification. The essential process parameters used for the model are identified and an introduction to the concept of transfer functions is given. Then the important aspects in experiments used for system identification are summarized. The section concludes with a detailed description of the models applied in this thesis.

### 2.1 The Extrusion Process

Extrusion is an established manufacturing process in the plastics industry since the second half of the 20<sup>th</sup> century [13]. The extrusion process became an important production method also for solid drugs lately because of its capability to combine continuous solid dispersion mixing, metering, mixing, blending, melting and shaping in a single step. Moreover, it reduces waste due to steady-state production and lowers the need for storage space for intermediate products compared to traditional batch process manufacturing. Figure 4 shows a possible application of an extrusion process in a pharmaceutical production. Ideally the extrusion process is the only process step from the raw materials to the capsule filling machine. However, an extrusion process line consists of a dosing system, the extruder, a downstream processing unit and a monitoring system. The units are discussed in the following subsections.

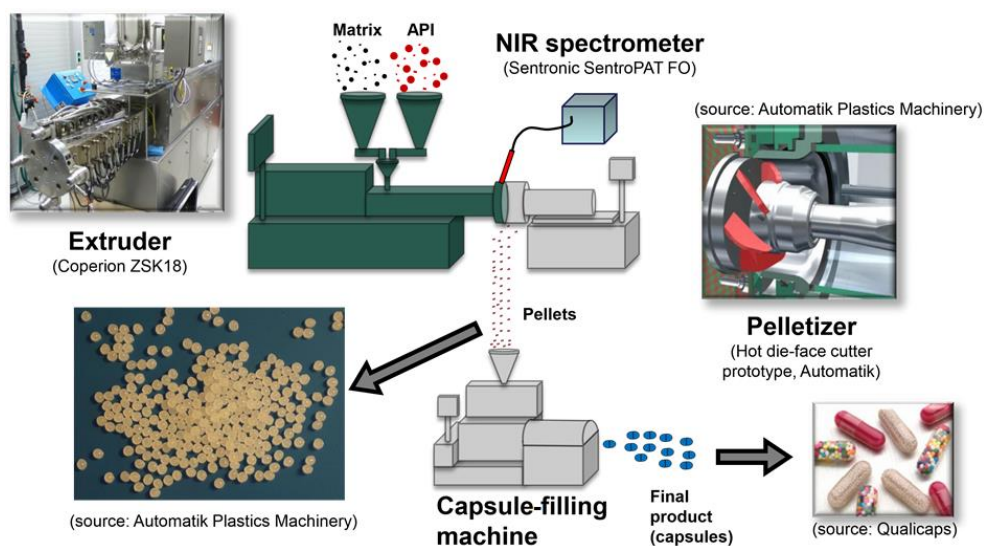


Figure 4: Possible integration of the extrusion process into a pharmaceutical manufacturing line [33]

### 2.1.1 The Dosing Unit

Raw materials for solid drug manufacturing are mainly solid and sometimes also liquid. Dosing of liquids is very well known and can be done very accurately. The dosing of solids and, especially, powders, on the other hand, is not so trivial due to their complex flow behavior. In principle, a dosing unit has to fulfill several tasks simultaneously. It has to measure, convey and control the current feeding stream [34]. In general, there are volumetric and gravimetric feeding systems. In volumetric feeding systems a volume flow is set and the feeder doses the powder constantly with process parameters determined in a calibration run (e.g. screw speed, vibrational power, belt velocity, etc.). Gravimetric feeding systems, on the other hand, control the feeding rate by measuring the weight of the feeding stream continuously. In loss-in-weight feeders, the hopper is placed on a scale. The scale measures continuously the loss-in-weight time curve and calculates the current feed rate from that. The types of feeding systems are screw feeders, vibrating feeders, rotary valve feeders, belt feeders, rotary table feeders, rotary ring groove feeders, chamber feeders and piston feeders, most of them able to operate in both ways, volumetric and gravimetric.

The dosing unit is evaluated by dosing accuracy. First of all, the dosing accuracy results from the combination of material, feeder type and its parameter set. This accuracy equals the biggest acceptable deviation of the feed rate from the set-point within a defined time interval. Figure 5 shows detected feed rates averaged over  $\Delta t$  displayed as points in the graph. The feed rate set-point ( $\dot{m}_{Set}$ ) is indicated with a solid line. The tolerated dosing accuracy is indicated with dashed lines above and below the set-point. This tolerance band ( $\dot{m}_{Set} \pm \Delta\dot{m}$ ) limits the feed rates accepted in a certain feeding application. In case of drug manufacturing, the deviation is given indirectly by the European Pharmacopoeia 7.8. The dosing accuracy is tested with standardized content uniformity tests on the final dosage. Thus, no strict limits on feeding accuracy exist.

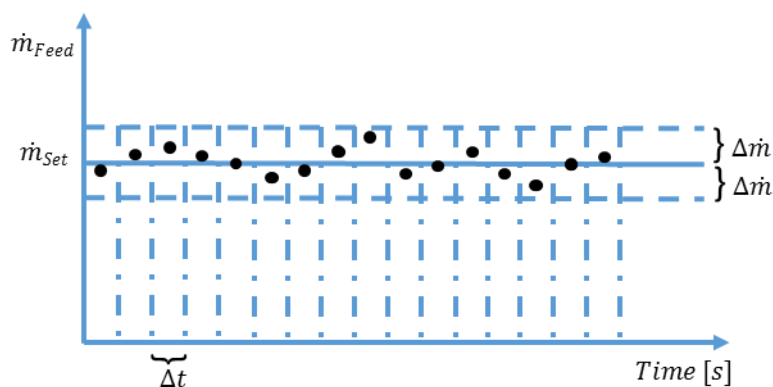


Figure 5: Dosing accuracy with tolerance band (according to [34])

The challenge is to find the optimal method for a certain dosing problem among this wide range of feeding principles. As mentioned before, an essential selection criterion is the material which has to be fed. Powders are characterized according to their bulk density, compressibility, electrostatic properties and flow behavior, which is influenced by particle distribution, size and shape, moisture content, presence of flow agents, temperature and chemical composition. The flow behavior is either free-flowing, or cohesive, whereas cohesive behavior can cause bridging or rat-holing in the feed hopper. Often, free-flowing powders can be dosed at sufficient accuracy with volumetric feeders. For cohesive powders, on the other hand, it is necessary to use gravimetric feeders. Moreover, agitators, constructed as rotating blades, can be installed

in the feed hopper to break bridges and rat-holes and ensure a steady flow of material into the conveying screw. The pharmaceutical industry usually uses loss-in-weight screw feeders with rotating blades in the hopper as depicted in Figure 6.

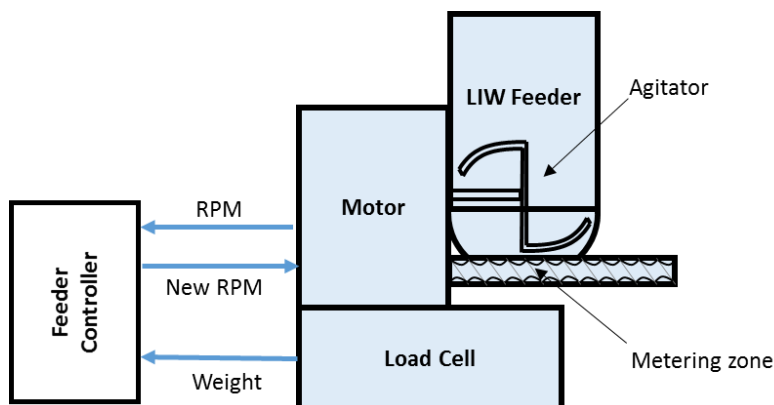
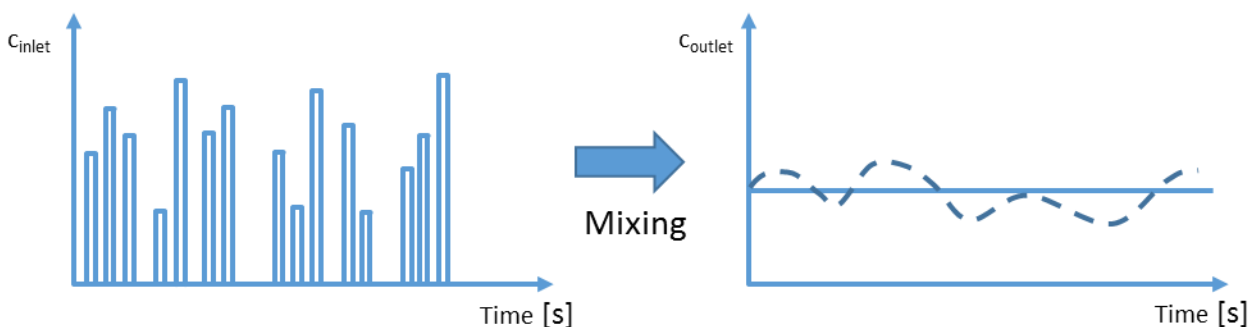


Figure 6: Sketch of a loss-in-weight feeder

Extruded dosage forms consist typically of several components, e.g. matrix carrier, API, plasticizer etc. Thus, there exist two feeding strategies to supply the extruder with a multicomponent formulation, namely: premix feeding and split-feeding. In the plastics industry, normally, split-feeding is applied [22], [35] and premix feeding is a characteristic of the pharmaceutical industry [31]. Premix feeding means, that a mixture with a certain API content is blended before the extrusion and the mixture is then filled into the hopper of the feeding system. In this case, the advantage of combining several steps, including mixing in one extrusion process is lost and the risk of segregation in the hopper is present. An advantage of premix feeding is that the feed rate for the mixture is higher, as only one inlet stream is required, compared to feeding all the components separately. Small feed rates are a challenge for dosing [36]. The smaller the feed rates get, the less continuous is the powder flow and the relative size of disturbances becomes bigger. Especially when using cohesive materials, the powder is not flowing out of the screw but rather falling down in separate agglomerates every other instant of time. As the extruder dampens such high-frequency fluctuation though, this behavior should not be a problem, if the overall feed rate is correct. Figure 7 shows schematically the damping effect of an extruder after a discontinuous powder feeding step. The bars in the left graph represent agglomerates of differing mass falling out of the feeder every other instant of time. The right graph illustrates the result after a perfect mixing process (solid line) and an imperfect mixing process (dashed line), like an extruder.



**Figure 7: Effect of ideal mixing behavior in an extruder on fluctuating inlet concentrations**

Another influential factor on the dosing accuracy of feeders is the refilling cycle of the feed hopper. If a big amount of material has to be processed, it is common to refill the hopper from time to time. During these refill actions, the feeder changes into a certain refill mode, mostly using volumetric feeding.

There are different types of dosage errors. First, a deviation of the mean of the measured values from the set-point over a longer period, e.g. 30 minutes. This can occur permanently, due to wrong calibration or set-point, or because of drifting after a certain time caused by material consolidation. Thus, it is possible to divide the errors into feeding accuracy and feeding stability.

In this thesis two loss-in-weight, twin-screw feeders are used in split-feeding mode. Both feeders are characterized by determining their mean feed rates and standard deviation, as well as the deviation from the set-point for several flow rates. The feed rates displayed by the feeder are compared to the feed rates calculated from the mass increase on a catch scale underneath the feeder outlet. Additionally, a frequency analysis of the measured feed rate is performed. Further information on dosing can be found in [34].

### 2.1.2 The Extruder

Generally, an extruder consists of one, two, or more screws, which rotate inside a tight-fitting cylindrical or conical housing. Figure 8 illustrates the classification of extruders according to screw arrangement. Single screw extruders are mainly used for melting, mixing and pressure build-up. The mixing capability of such machines is very limited. One application is injection molding, for example. Twin-screw extruders have two parallel rotating screws, which can be counter- or co-rotating and closely intermeshing or non-intermeshing. Counter-rotating screws can rotate at limited speed only, because of the outward-pushing effect when material is squeezed in the gap between the screws. Intermeshing extruders are not limited in rotation speed and, furthermore, exhibit the advantage of self-wiping behavior of the screws, due to the small clearance between them. Multiple-screw extruders are used for special applications in the plastics industry only. Thus, the twin-screw, co-rotating, closely-intermeshing extruder is the most popular choice for pharmaceutical applications.

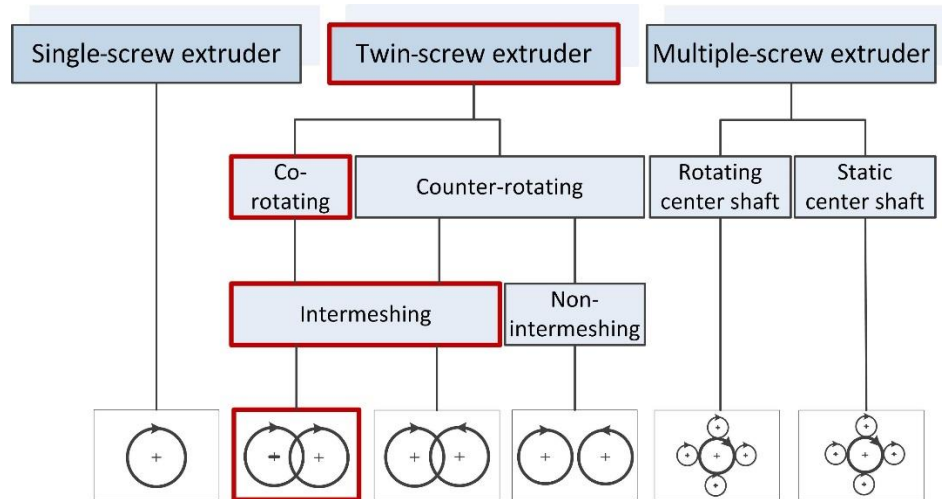


Figure 8: Classification of extruders [8]

### Requirements for the Extruder

Extruders are used for pre-processing of materials, like production of specific types of solid dispersions e.g. solid solutions, or modifying the particle size of the material (powder to pellets), or producing premixes in desired handling forms, as well as for the final production step, when combined with certain downstream processing units like hot-die face pelletizing, for example. In recent work extrusion is applied to stabilize nanoparticles [37]. For heat-sensitive products, on the other hand, it might be necessary to keep the thermal stress during the process under a certain level. To meet so many different needs, the extruder is divided into processing zones, which can be combined according to the current task.

### Processing Zones [13]

The processing zones of an extruder consist of certain combinations of screw elements and barrel configurations. These zones provide a characteristic effect for the processed material.

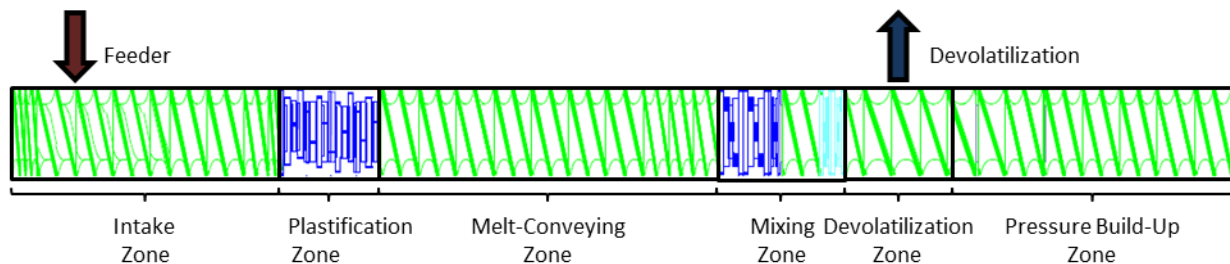


Figure 9: Processing zones illustrated along a specific screw configuration, adapted from [8]

Thus, by varying these zones, desired product attributes can be achieved. Temperature or shear stress restrictions of processed material can be met in order to avoid degradation. The zones, again, consist of modular combinations of screw elements, so that intensity and length of the zones is variable.

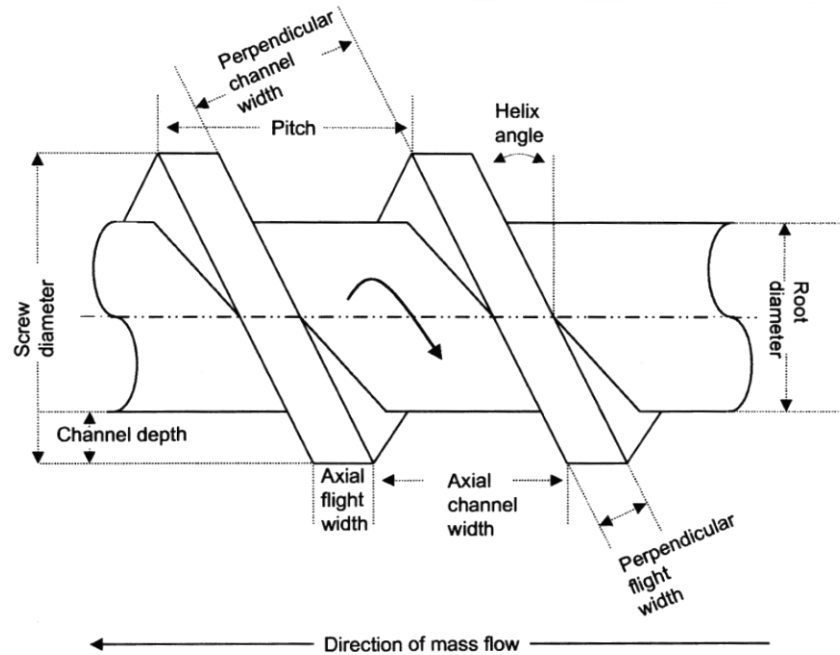


Figure 10: Extrusion screw geometry [38]

The most common elements are conveying, re-conveying, kneading and toothed elements. Basically, they vary in pitch size, conveying direction and free cross-section, that is channel depth, or number of flights. The realizable channel depth is limited by the extruder geometry, though.

Conveying elements can be realized with a big or small pitch, resulting in a variation of conveyable material and filling grade. Elements with small pitches convey the material with higher force and thus higher pressure build-up at the same length. Re-conveying elements convey material in the counter direction and are used to increase the filling grade of the previous processing zone. Still, the re-conveying effect must be weaker than the pressure-driven flow, so that a positive flow in the conveying direction is present. Kneading blocks are used to introduce shear forces into the material and mix due to parting and recombining of flow currents. The kneading elements can be designed in conveying or re-conveying mode and, additionally, neutral, without any conveying effect. The small, or big pitch is realized with narrow and wide discs in this case, where wide discs introduce bigger shear rates, but less mixing than the narrow discs. Kneading blocks can also be double- or triple-flighted, resulting in an increase of the characteristic effect. Then, there are certain special elements like toothed elements, for example, which are designed specifically for a certain task like mixing, for example.



**Figure 11: Conveying elements with different pitch size, conveying direction (forward, forward, backward)**

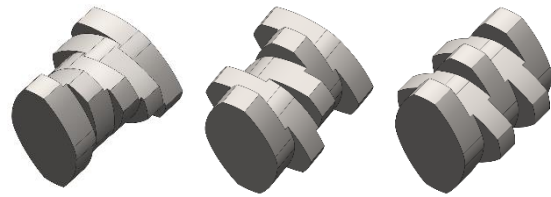


**Figure 12: Kneading elements with identical disc widths, but varying pitch sizes, and conveying directions (forward, backward, neutral)**

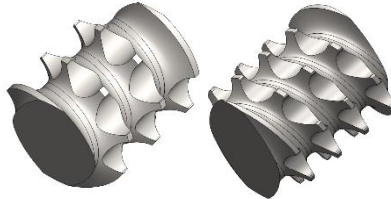


**Figure 13: Mixing elements with different pitch sizes**

In the following paragraphs, typical processing zones are illustrated [13]. All the zones influence each other and all are highly dependent on screw speed and throughput, so they cannot be viewed separately. Still, to give an overall idea of these zones, they are listed in the following section.

### Intake Zone

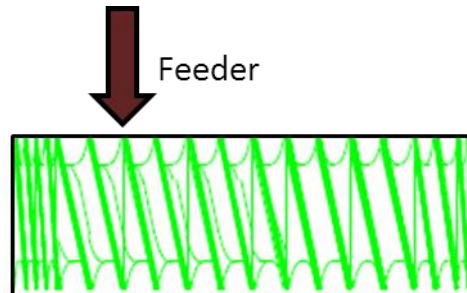


**Figure 14: Illustration of an intake zone**

The intake zone is located at the beginning of the extruder, where the material is fed into the screw. The tasks of the intake zone are conveying and compressing of solids. The influential parameters in this zone are, besides screw speed and throughput, the free screw volume, the pitch, the bulk density of the fed material and the friction of the material to the barrel wall. Therefore, the intake process is limited by the available volume. The elements in the intake zone should provide a large free cross-section and the ability to convey the material effectively. Especially at the feeding inlet, the screw is only partially filled, so that air or evaporated water, which is brought in with the powder, can escape through the unfilled parts of the screw and the powder inlet. Moreover, the intake zone is cooled, so that no material sticks to the wall in the intake barrel or the feed hopper. At the end of the intake zone, elements with a small pitch compress the material for the plastification zone.

### Plastification Zone

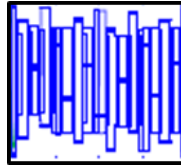


**Figure 15: Kneading blocks in a plastification zone**

In the plastification zone the material is molten and solids pre-dispersed. The key parameters are the screw geometry, the heat flux, combined with throughput and screw speed, the specific heat capacity, the heat conduction, the melting enthalpy and the particle size of the material. In general, the melting process is influenced by residence time and degree of filling. A high degree of filling enhances the melting and the melting starts when the screw is initially fully filled. The energy for the melting is basically brought in by the screw and varying the barrel temperature in the plastification zone has barely any effect. The barrels are heated only to get a melt film on the wall, which creates adhesion between the polymer and the wall. In that way, a shear gradient is generated, which further accelerates the melting. The required melting length is governed by the melting enthalpy of the material, the melt viscosity and the screw geometry. A low melting enthalpy, a high melting viscosity and narrow kneading discs on the screw accelerate the melting. Through these elements a first homogenization of the material takes place also. This zone requires the biggest amount of mechanical energy input over the whole process.

### Melt-Conveying Zone

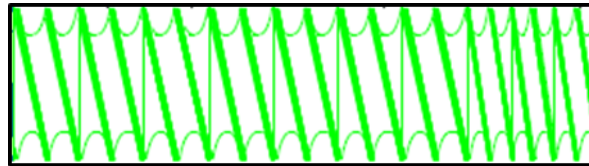


**Figure 16: Conveying elements with different pitches in a melt conveying zone**

In the melt conveying zone the material is already molten and conveyed forward. The parameters governing this zone are the screw speed, the throughput, the pitch and the material properties. Usually, this zone is only partially filled and transports the material from one processing zone to the next. The energy input should be minimized. Depending on the following processing zone, the last elements, again, compress the material due to smaller pitch sizes.

### Mixing Zone

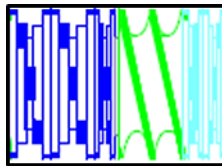


**Figure 17: Conveying (dark blue) and re-conveying (light blue) kneading elements with different disc widths in a mixing zone**

The main mixing mechanism in an extruder can be distinguished between distributive and dispersive mixing [13]. The two mixing mechanisms are illustrated in Figure 18. Distributive mixing is caused by macroscopic rearrangements. It is based on kinematic processes and is independent from the rheological behavior of the

material. In the extruder, which typically inhibits a laminar flow regime, this is realized by parting and reunion of melt flows and by back-mixing in zones of back-pressure. Thus, many rearrangement sequences and long mixing time enhance the homogeneity of the material. *Distributive mixing* is homogenization of material and temperature due to shear forces. The target is to distribute solid agglomerates or fluid droplets over the shortest possible mixing length with the minimum energy input. To break up such agglomerates, or overcome the surface tension of a phase interface, a minimum shear and strain rate must be reached. No dispersion of multiphase systems occurs beneath these critical flow forces. A certain minimum residence time in the stress zone is required. Thus, dispersive mixing, in contrast to the distributive mixing, is influenced by the melt viscosity. The shear forces, most relevant to mixing, occur in the gap between ridge and wall as illustrated in Figure 19 and the highest extension forces before the ridge [39].

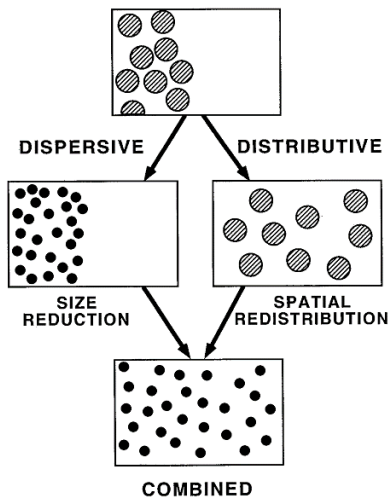


Figure 18: Dispersive and distributive mixing [40]

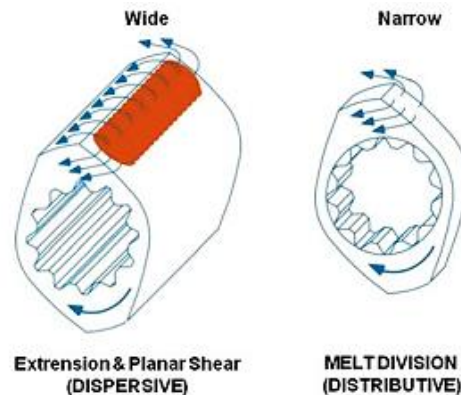


Figure 19: Example of dispersive and distributive mixing elements [41]

High viscosities, high screw speed, low throughput and narrow shearing gaps enhance dispersion. Kneading blocks with wide discs provide maximum shear rates. Applying high shear rates, though, also increases the temperature, while the viscosity decreases. Thus, dispersive mixing has an optimum.

#### Devolatilization Zone

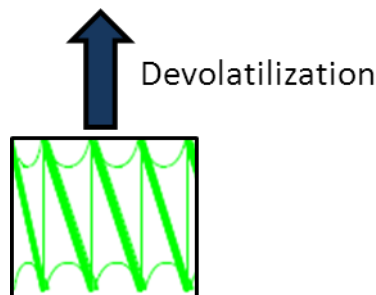
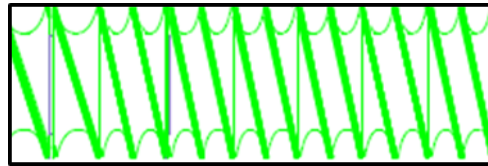


Figure 20: Conveying elements with big pitch in a devolatilization zone

In an optional devolatilization zone, water, solvents, or other volatiles can be removed from the melt. Therefore, the barrel is opened and connected to a vacuum pump. In order not to extract unmolten material

from previous sections or air from the inlet through this zone, the borders must be sealed by completely filled zones to either side.

### Pressure Build-Up Zone



**Figure 21: Illustration of a pressure build-up zone before the die plate**

In order to force the melt through the die plate, a pressure build-up zone is necessary. The required pressure results from throughput, die geometry and the melt viscosity. Low temperature, resulting in higher viscosity increases the ability to build up pressure, but also increases the force needed to press the melt through the die. Conveying elements with smaller pitch are used to accomplish this task. The screw is completely filled in front of the die plate over a certain back-pressure length. This length is the result of the equilibrium between counter-pressure and pressure generation of the pressure build-up zone. Within this back-pressure length a certain degree of back-mixing occurs, resulting in axial mixing. Thus, the RTD broadens and this is a positive effect for dampening out fluctuations in the input concentration. If the backpressure length is too long though, the upstream processing zones could be flooded. To increase axial mixing without the risk of flooding, several zones with back-pressure can be implemented along the screw. Back-pressure occurs upstream of every counter-pressure generating element, like re-conveying elements.

### Extruder Characteristics

The material runs through a certain characteristic processing history in every extrusion. This can be described with an RTD and a certain SE input. Both characteristics are tightly connected, as the SE input is strongly related to the time a material stays in the extruder.

### Residence Time Distribution Characteristics

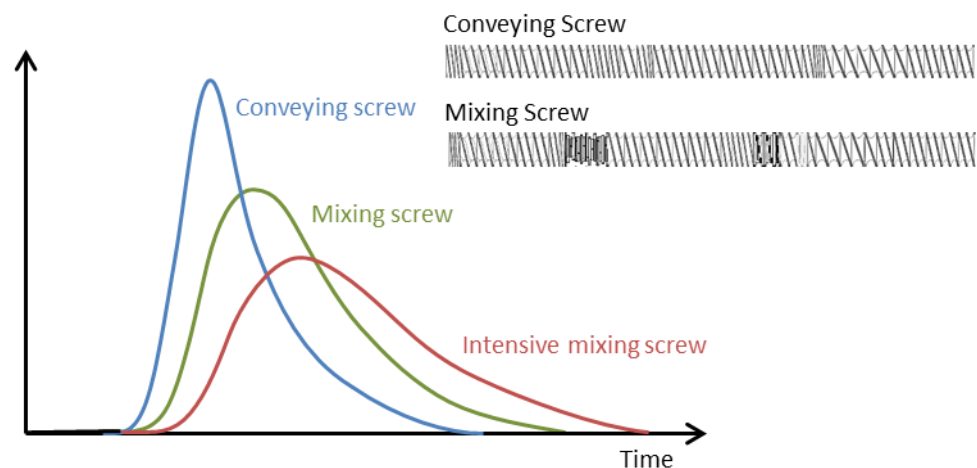


**Figure 22: Residence time distributions for different screw configurations**

In a continuous process, not all particles which enter the system at the same time, leave the system at the same time [16]. Thus, the extrusion process exhibits an RTD. The more kneading or backwards-conveying

elements are included in the screw, the broader the distribution gets, as illustrated in Figure 22. Moreover, the averaged residence time becomes longer. Accordingly, the RTD highly depends on the screw configuration [13]. Throughput and screw speed also influence the RTD. High throughput and screw speed narrow the RTD and reduce the *Mean Residence Time* (MRT). Throughput has a stronger influence than screw speed though, according to Gao et al. [32]. The extruder can be operated in fully filled or starved mode. A fully filled extruder has good pumping efficiency, but bad mixing behavior, due to the shorter residence time. Extruders operated in starved mode, on the contrary, exhibit good mixing behavior, but are less capable of building up pressure [41].

The normalized RTD curve, or residence time density function is defined according to Equation 1.

$$E(t) = \frac{c(t)}{\int_0^{\infty} |c(t)| dt}$$

**Equation 1**      **Normalized RTD function**

$E(t)$  represents the normalized RTD and  $c(t)$  the concentration of API at the time instant  $t$ . Time is defined to be zero at the moment of introduction of the tracer pulse into the extruder. Besides the residence time density function, the cumulative RTD function is also used to characterize extrusion processes. The cumulative RTD function is calculated using Equation 2.

$$F(t) = \int_0^{\infty} c(t) dt$$

**Equation 2**      **Cumulative RTD function**

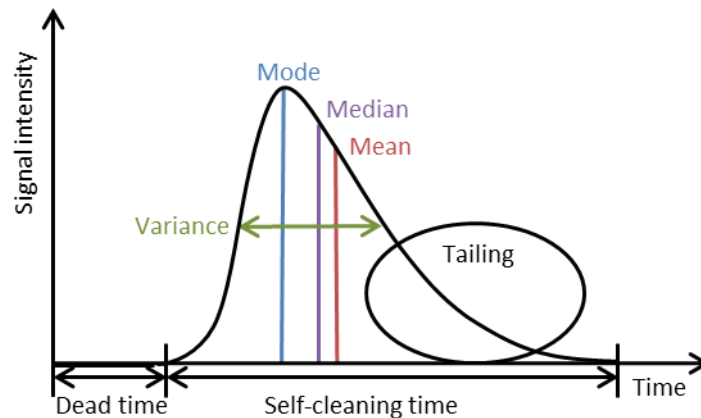


**Figure 23: Residence time density function with dead time and tailing**

The RTD density curve is characterized by certain time constants and shape features, as can be seen in Figure 23. The mode, median residence time and MRT are statistical parameters, which can be used to roughly compare screw configurations. The mode value gives the most frequent residence time. When performing color tracer experiments, this is the moment with the most intense coloring. The median represents the time half the particles need to leave the system and the mean, or first moment of distribution, is the averaged residence time for all particles. The MRT is usually used for simple comparisons and is

governed by the pitch and screw speed, as well as throughput for fully filled sections [13]. Increasing pitch size, throughput and screw speed all decrease the MRT.

$$\bar{x} = \frac{1}{n} \sum_{i=1}^n (x_i)$$

**Equation 3** Mean value, or first moment of a distribution

$$\bar{t}_v = \frac{f \cdot V_{free}}{\dot{V}}$$

**Equation 4** Mean residence time

Expressed in terms of residence time, the MRT is defined as shown in Equation 4.  $f$  is the volumetric filling grade in partially filled zones,  $V_{free}$  the free volume and  $\dot{V}$  the volume flow. The volumetric filling grade is defined according to Equation 5, with  $\dot{V}_{max}$  defined as the maximum volumetric flow the extruder conveys forwards without counter-pressure. One thing to mention is that by inserting Equation 5 into Equation 4 it is possible to see that for partially filled zones along the screw, the throughput does not influence the MRT.

$$f = \frac{\dot{V}}{\dot{V}_{max}}$$

**Equation 5** Volumetric filling grade

The *Dead Time* (DT) of the system represents the time between introducing an input signal to the system and the moment when the system response becomes visible at the outlet of the system. It equals the minimum residence time of the extruder. This is the time frame available for the dispersive mixing in the system. The width of the RTD as a measure for longitudinal mixing is associated with the distributive mixing in the system. The width of the curve can be expressed as the variance  $s^2$ , or second moment of the RTD. Thus, variance is the crucial parameter, which allows evaluation of the dampening capability of the extruder.

$$s^2 = \frac{1}{n-1} \sum_{i=1}^n (x_i - \bar{x})^2$$

**Equation 6** Variance, or second moment of a distribution

The time between the minimal and maximal residence time contains information about the self-cleaning ability due to the self-wiping feature of tightly intermeshing twin-screw extruders.

The shape of the curve indicates how much back-mixing occurs in the system. Back-mixing is caused by longitudinal mixing in back-pressure zones. The RTD shows tailing on the right side, thus, it is positively skewed. The grade of skewness can be evaluated according the following equation:

$$\hat{v} = \frac{1}{n} \sum_{i=1}^n \left( \frac{x_i - \bar{x}}{s} \right)^3$$

**Equation 7 Skewness or third moment of a distribution**

Besides the RTD, Gao, Walsh, Bigio et al. [32] suggest the introduction of RRD and RVD, as discussed in the introduction already, which facilitate the comparison of screw configurations independent from material properties and operating conditions. The RRD gives insight into the transport behavior of the extrusion set-up, relating the RTD to the number of screw revolutions from the moment of adding the tracer pulse. The RVD is useful for evaluating the mixing process in an extruder and will be introduced shortly.

The RVD indicates the physical distribution of the tracer in the extrudate along the extruder length after an impulse input, thus it is a measure of the extrusion process effectiveness. It is defined by Equation 8.

$$G(v) = \frac{c\left(\frac{v}{Q}\right)}{\int_0^{\infty} \left|c\left(\frac{v}{Q}\right)\right| dv}$$

**Equation 8 RVD Definition**

In this equation  $Q$  is the material throughput in L/min and  $v$  represents the extrudate volume after the tracer is added into the extruder. The relation to  $t$  is  $t = v / Q$ . Insight into the mixing process is limited to axial mixing though, and does not contain any information about the uniformity of the extrusion, or the concentration gradient of the components. It is interesting though, that when time zero is set to the moment of first registration of tracer at the outlet, the RVDs are the same for a certain screw configuration at different operating conditions. This suggests, that the physical distribution of a tracer along the extruder is influenced strongly by the screw configuration and less by the throughput and screw speed.

The cumulative RTD can be derived from step-change experiments. The first derivative of a unity step response is equal to the normalized RTD in Equation 1. Figure 24 illustrates a typical step-change response of an extrusion process. Characteristics like the delay time and the settling time are equivalent to the dead time and the maximum residence time in Figure 23. The rise time can be related to the self-cleaning time from the residence time frequency function. The settling time gives the time after which the system reaches a steady state again. Figure 24 also shows a typical behavior of an extrusion process with an overshoot after the step change. This overshoot can be caused by overshooting of the feeder until the controller manages to settle the new feed rate at the set-point.

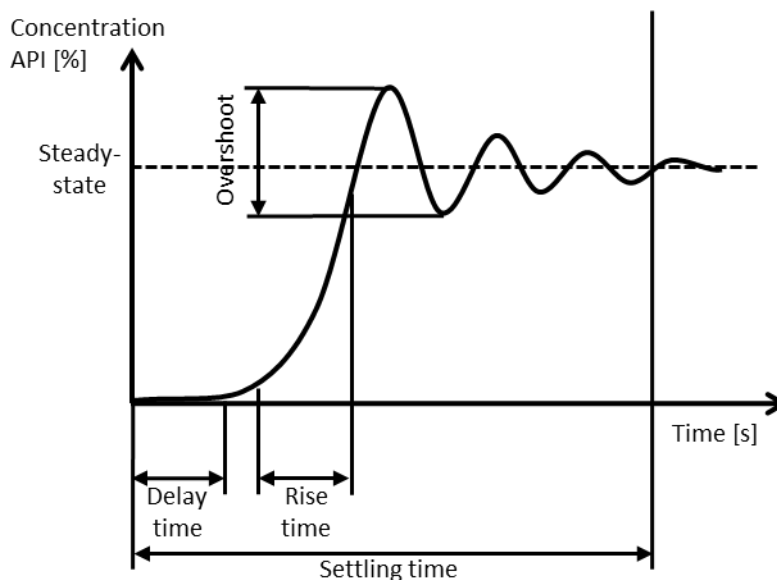


Figure 24: Step response with characteristic parameters [8]

Knowledge about screw configuration's specific RTD does not only facilitate estimation of mixing behavior, but also stress exposure during extrusion. Whilst a broad RTD density function is good for mixing problems, it is not desired if a reaction takes place, or there is danger of material degradation due to high stress. In the case of heat-sensitive products, such as enzymes or vitamins for example, the RTD allows estimation of the degree of degradation.

#### Specific Energy Input

Energy is brought into the extruder via rotation of the screws (mechanical energy) and through heating in the barrels (thermal energy). The SE input gives the energy input per kg of material in the extruder. Therefore, it also depends on the throughput and size of the extruder. The higher the SE input is, the higher the melt temperature in the extruder becomes [13]. The application of long residence times and big shear stress in order to enhance mixing might cause degradation. Thus, a trade-off must be found in order to stay within a sensible process window, as illustrated in Figure 25.

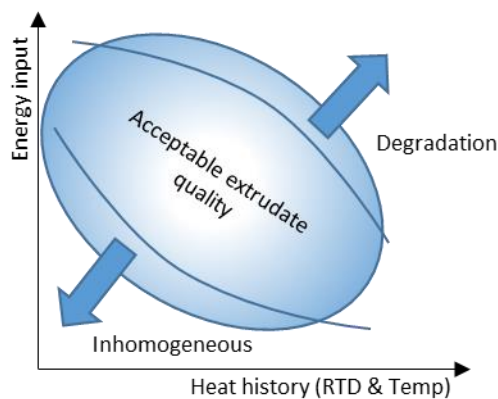


Figure 25: A schematic showing the balance of energy input and heat history with the extreme combinations of these, resulting in either degradation or inhomogeneous material (adapted from [4]).

There are several types of degradation which can occur in an extrusion process [42]. Thermal, oxidative, chemical and mechanical degradation can lead to reduction in molecular chain lengths or undesired reactions. With a broad RTD the exposure of the material to this stress becomes less controllable, as an increasing share of material is exposed to this stress longer than the average.

### 2.1.3 The Downstream Processing Unit

At the extruder outlet, the material is a strand coming from the die plate. In order to get the desired shape for the product, a shaping unit is used. There are many different types of downstream processing units, like calandring, strand cutting, hot-die face cutting, or die molding. Calandring is usually applied when the material is milled again, in order to get a small and homogenous particle size. Strand cutting and hot-die face cutting are used for pelletization. The pellets can either be filled directly into capsules, or are milled and used for tablet pressing. Die molding, or injection molding allows producing different shapes, like rings, rods or certain profiles for example. It is also possible to integrate a gate for out-of-spec products. It ejects product if bad quality is predicted by a real-time controller. Figure 26 gives several options for downstream processing units of an extrusion process.

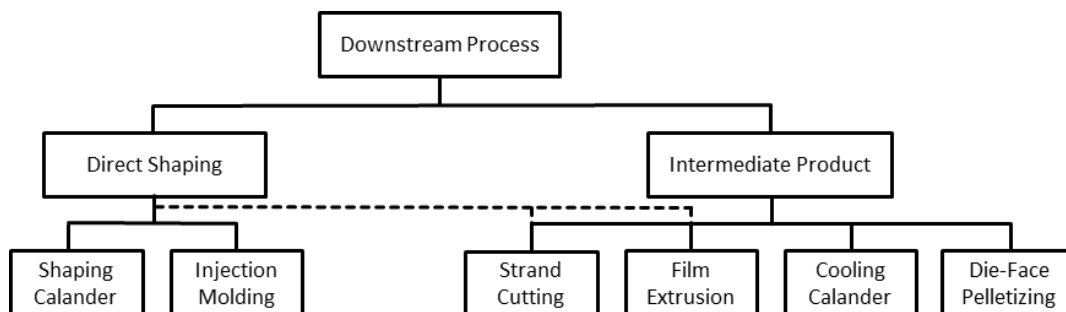
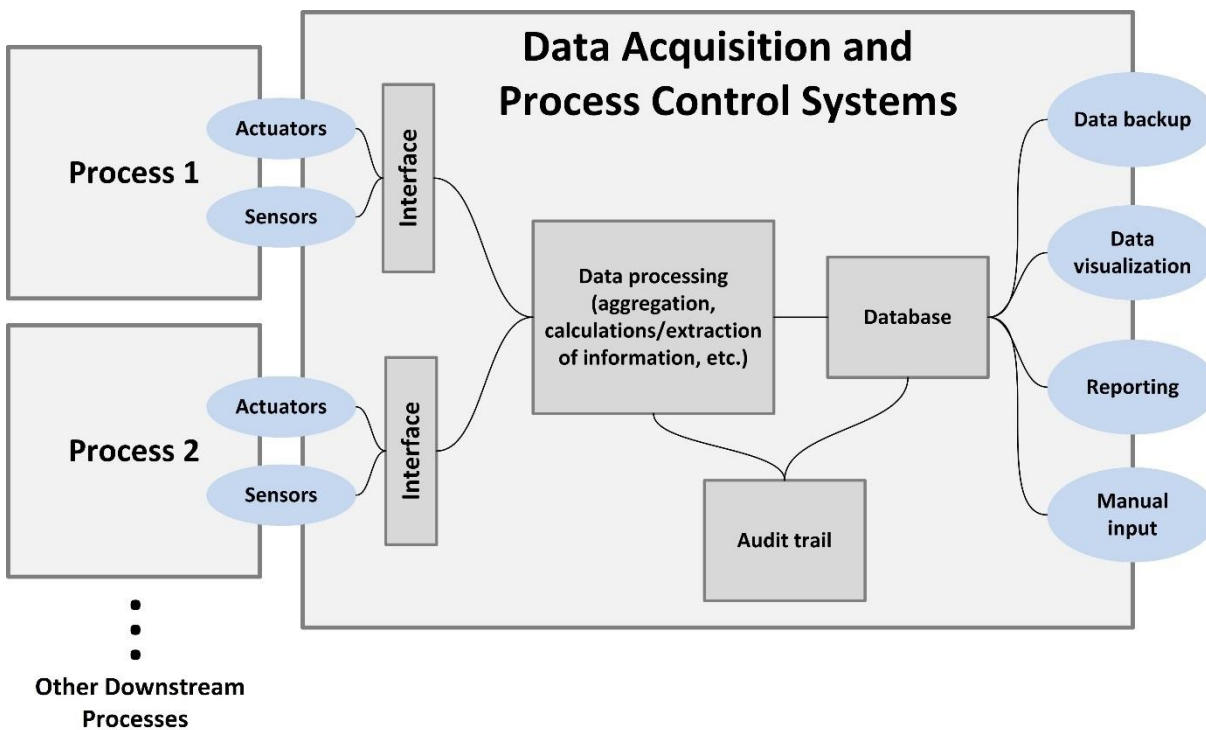


Figure 26: Several downstream processing options for an extrusion line (adapted from [43])

### 2.1.4 Process Monitoring System

In order to control and predict a certain product quality according to GMP requirements, an extrusion line needs in-line monitoring of several material and process parameters. Screw speed, torque, feed rates, API concentration, material pressure, temperature and pellet size, or shape uniformity in downstream processing are a few examples. These parameters are monitored with different sensors from different manufacturers. The sensors collect either univariate data like temperature and pressure or multivariate data like spectra. Sampling intervals vary according to the optimum in a trade-off between noise reduction, relevance for system dynamics and limitations due to computational performance. A sensible process monitoring system has to collect all data from differing interfaces and store them in a time-aligned fashion. For controlling issues, the collected data must be processed and analyzed and a control strategy applied in real-time.

Besides providing a common interface, a process monitoring system should contain a database for offline analysis with visualization tools and the possibility of generating reports and data backups.



**Figure 27: Schematic of a basic data acquisition and process control system for a continuous manufacturing line consisting of several processes (i. e., feeding, extrusion, downstream, etc.) [43]**

A few classical monitoring methods for a melt extrusion process are classical methods like pressure, temperature or torque measurements, spectroscopic methods like Raman, UV/Vis, vibration analysis, NIR or fluorescence, scattering methods such as sound scattering, light scattering and X-ray scattering and, finally, imaging methods such as photography, optical microscopy, or X-ray imaging [44]. The classical methods are used for investigating process parameters or material properties in direct measurement. Spectroscopic methods detect a spectrum, from which it is possible to predict material properties using a chemometric model. The chemometric model is used to extract the desired information, such as composition or conversion from a spectrum. Scattering and imaging methods are used to detect structure, morphology and defects.

For investigating the CU of an API, NIR spectroscopy can be applied. The advantage of NIR spectroscopy is that the method is non-invasive and no sample preparation is necessary for in-line measurements. A downside of NIR spectroscopy is that the detected spectra do not only depend on the detected molecules due to the different absorption properties of different molecule structures, but also on physical properties such as temperature and melt composition. As these properties are influenced by pressure, screw speed and filling grade in the extruder, it is difficult to interpret the spectra without additional knowledge. Still, NIR is reported to be used for determination of melt composition in extrusion processes several times [2], [30], [31], [45].

## 2.2 System Identification

The statistical parameters and the RTD approach given in the previous section are very useful to get an impression of the system and allow easy comparisons between different set-ups. They cannot be used for process prediction or control though.

The behavior of a *Linear Time Invariant* (LTI) system is usually described with a differential equation or a differential equation system. Often these models consist of fundamental physical processes, thus they are mechanistic models. It is often very complex and time-consuming to find general solutions for these equations in order to calculate the output for any input. For LTI systems it is possible though to find a solution equivalent to the impulse response of the system. With this solution it is possible to apply the model for any input signal, when taking every signal for a row of impulse functions. The mathematical operation for this is convolution. The reader might remember, that the RTD is equal to the system response to an impulse input. It is possible to simplify applying the impulse response solution of a differential equation on the input signal in the time domain by transforming them to the frequency domain. In the frequency domain, complex mathematical operations become algebraic and, thus, are easier to solve [46].

For non-LTI systems it is not possible to convert a mechanistic model to the frequency domain. Therefore, another approach must be used. Another method for modeling dynamic systems is to develop black-box models. Black-box models are data-based models, which are not based on physical processes, but merely picture the typical system behavior. This is done by performing system identification. System identification means referring a measured output signal to a given input signal. This is called transient response analysis. Transient response analysis contains methods like impulse response analysis, initial condition response and step response analysis. These methods are easy to apply and provide basic information about a system like input-output gain, dominating time constants and time delays [47]. The result of a transient response analysis is a black-box model defined by the transfer function for the system.

In order to receive a meaningful black-box model from system identification experiments, several considerations must be kept in mind. Figure 28 gives a schematic overview of the system identification loop. The procedure starts by choosing an experimental design. This includes a first selection of input (manipulated) and output (response) variables, input type, including excitation shape, frequency and amplitude based on prior knowledge about operating ranges for the system and the choice of sampling frequency. Then, data is collected and usually pre-treatment performed. This includes removal of high frequency disturbances by smoothing and elimination of outliers by defining cut-off amplitudes for impossible values. In some cases also drift, i.e. low frequency disturbances, can be removed depending on the purpose of the model. Secondly, the type of a model must be chosen. Common process models are transfer function based models like Box-Jenkins and *Autoregressive Moving Average models with external input* (ARMAX), or state-space models. Third, the model structure is determined by the order of the model and the time delay  $\delta$ . There are several criteria for identification of the system order. The  $R^2$  value measures the correspondence between the model and measured data. Thus, it identifies the best-fit model. *Akaike's Information Criterion* (AIC) and *Young's Identification Criterion* (YIC) both additionally take into account that more complex models might contain too many parameters. This causes over-fitting of the modeling data set. Additional parameters are accepted only if the model accuracy increases significantly. Furthermore, the YIC test considers the reliability of estimated parameters via a standard error on parameters' estimates. Often these parameters recommend different model orders though, and the decision which criterion should be trusted must be made from case to case. Especially on processes consisting of

several sub-processes, it might be appropriate to regard a higher-order model representing a network of low-order models.

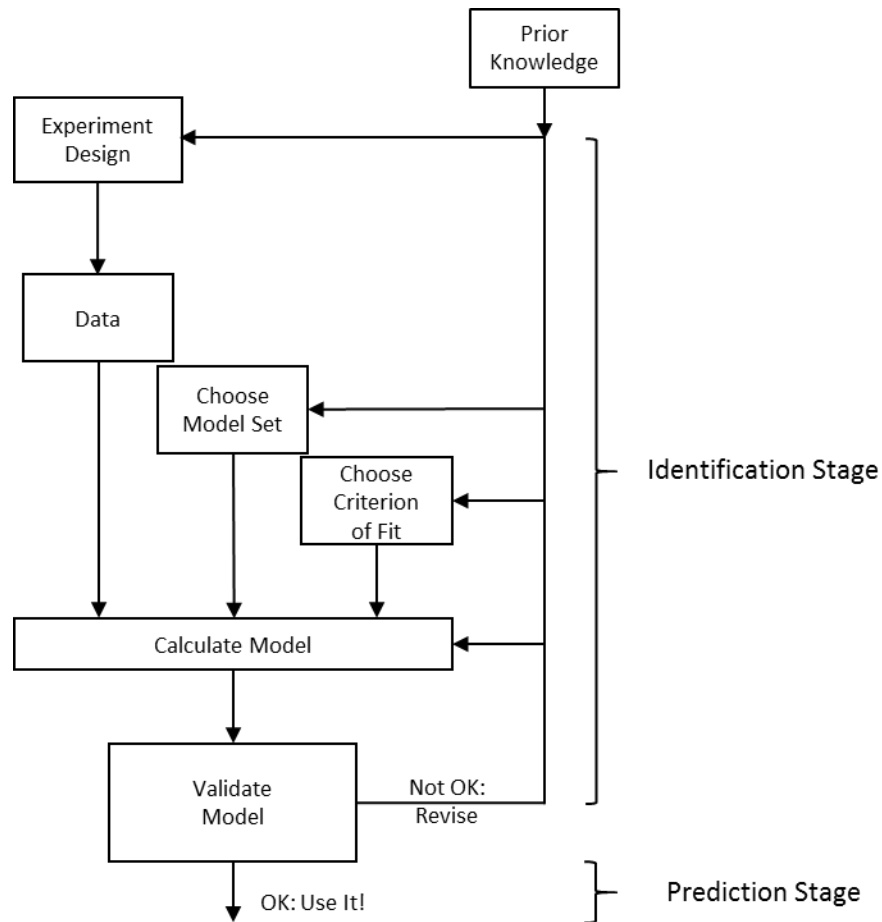


Figure 28: The system identification loop, adapted from [48]

Finally, the model is calculated and fit for validation. Validation is performed to select the best model. Therefore, it is necessary to regard the intended purpose (e.g., for controlling or simulation) and the ability to describe the real system. Validation can be done by looking at poles and zeros of the models, checking the frequency response and confidence intervals of parameters. Moreover, simulations can be performed and checked against real data or model errors tested. Model error testing is performed with auto-correlation and cross-correlation.

In case no appropriate model can be found, the loop has to be repeated starting with a new design of experiments. Reasons for this are selection of wrong model order, bad data set, wrong validation criterion or failure of the numerical procedure to find the best model.

### 2.2.1 Process Parameters in the Extrusion Process

For the first step in the system identification loop, appropriate input and output parameters must be chosen. In the extrusion process, material properties like heat capacity, density of bulk and melt, melting points and flow properties are available. Machine parameters are extruder geometry, screw design, feeder type and die shape, for example. Measurable process parameters are feed rates, temperatures, pressure and screw speed, for example. Figure 29 gives a schematic overview of parameters recorded during an extrusion. Not all these parameters influence the dynamic behavior of the system.

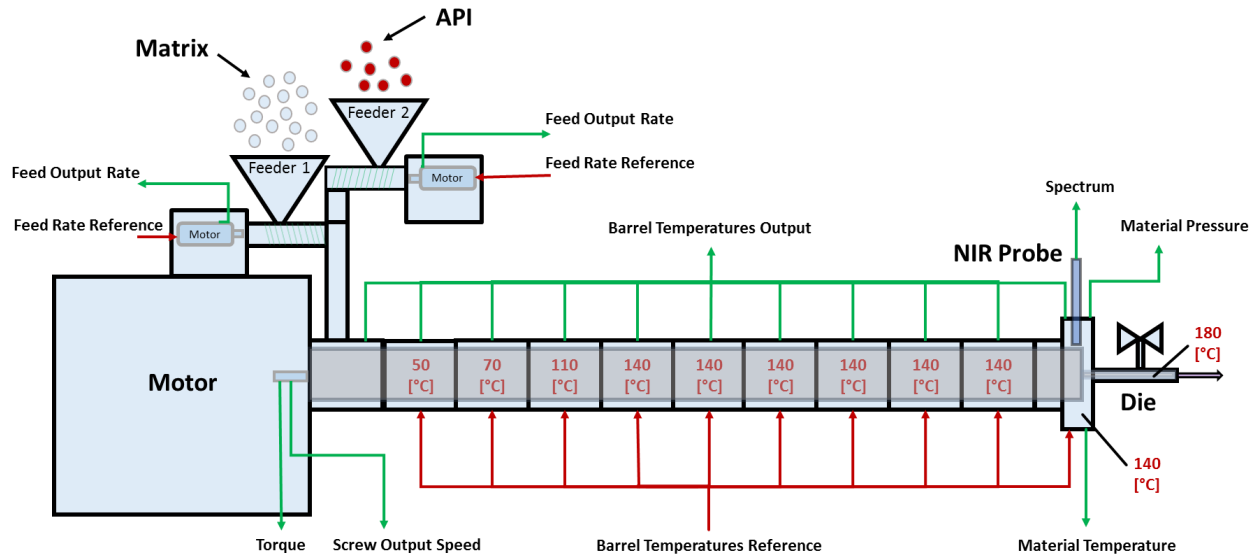


Figure 29: Input and output parameters for the extrusion process, adapted from [8]

In order to receive a useful model, only input parameters which affect the quality attributes must be included into the model. These parameters are then used as manipulated variables. From the output parameters, again, those containing information about the product attribute of interest must be identified. In case of implementing a control algorithm with this kind of system identification, these are the controlled variables. In general, the extrusion process is a multiple-input multiple-output (MIMO) system. If the investigated quality attribute is the degree of degradation for a heat-sensitive API, parameters like screw speed, throughput or SE input and concentration of API must be included in the model. If only the mixing process in the extruder is investigated, then it is appropriate to use the API concentration at the feeder inlet as the manipulated variable. In split-feeding mode, the input concentration can be calculated from the feed rates of the feeders. A possible selection for the response variable is the NIR-estimated API concentration at the end of the extruder. Thus, it is possible to reduce the system to a single-input single-output (SISO) system. Still, it is important to remember that the screw speed, material viscosity and, therefore, also the temperature have influence on the RTD, respectively, impulse response. If a model depends on too many parameters though, the significance is diminished. If too little parameters are chosen, the model is unable to represent the system.

### 2.2.2 Requirements on System Identification Experiments

A basic problem in system identification is the choice of experimental conditions, such as experiment duration, test signal design and sampling frequency [47]. In the following sections, common approaches to setting these conditions and the motivation to do so are given.

#### Test Signal Type and Experiment Length

After the input and output parameters are selected, typically, the type of input signal is chosen. Impulse, step, or sinusoidal signals are common input signal types. Moreover, *Pseudo Random Binary Sequences* (PRBS) are applied to cover a wide frequency range [24]. These input signals excite the system, so that the dynamic behavior can be extracted from the response in the output signal. In the selection of an appropriate input signal, one should take into account which cases are relevant for the specific process. Moreover, it is necessary to ensure enough excitation during the experiment. Thus, the experiment duration is chosen according to an appropriate number of impulse stimuli.

#### Excitation Amplitude and Frequency

The selection of signal amplitude and frequency must be made. Here, relevant time constants, such as dead time and settling time in the process must be considered. Data for modeling the dynamic behavior should cover all relevant frequencies. This includes a frequency matching the minimal characteristic time constant.

The amplitude for the test signal should lie within a range relevant for the process under normal operating conditions. Moreover, it is important to know the range of linear behavior of the system. The lower limit for the signal amplitude is determined by the *Signal-to-Noise Ratio* (SNR).

#### Sampling Frequency

Measurements are periodic observations of a system parameter in a time interval  $T$  (the sampling period). As discussed previously, the sampled function is represented by a sequence of infinitely short pulses with the frequency  $1/T$ . When choosing the sampling frequency, it is necessary to consider the effects of discretization, such as aliasing and loss of information. The sampling theorem by Nyquist and Shannon states that, in order to avoid aliasing, the measurement frequency must be at least twice the highest frequency in the process [47] and four to ten times as fast as the minimum relevant frequency for dynamic behavior [49]. Another aspect is that there should be at least ten data points in each transition phase [49]. Thus, the measurement interval is a function of the dynamics of the system.

If there is no or insufficient previous knowledge available, it is common to perform first-stage experiments to find correlations between process variables and estimate process time delay and the relevant frequency and amplitude ranges.

### 2.2.3 Relevant Models

This sections includes the relevant models for this application. In order to give an introduction, it starts with the basic idea of transfer functions. As an extrusion process line consists of several sub-processes, such as the feeding step, the extrusion process and the estimation of the API content via a chemometric model, those sub-processes are discussed separately.

## The Transfer Function

A transfer function represents the typical reaction of a system on a stimulus. For a certain input  $u$  (stimulus) a systems gives a certain output  $y$  (response).

Every input function can be treated like a sequence of infinitely short impulse stimuli, thus also every response can be considered as a series of impulse responses.

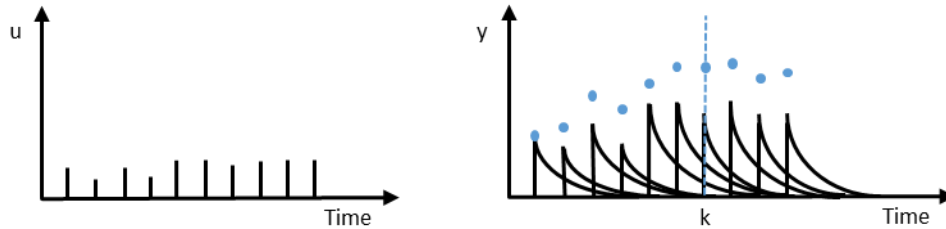


Figure 30: Every response can be regarded as a series of impulse responses

Accordingly, for a linear system, the correlation of the output to the input function is characterized by

$$y(t) = \int_0^{\infty} g(\tau) \cdot u(t - \tau) d\tau + v(t) = g(t) * u(t) + v(t)$$

Equation 9 Convolution equation for a linear system

with  $y(t)$  standing for the response function,  $u(t - \tau)$  for the input function, which is defined for  $(0, \infty]$ ,  $v(t)$  for external inputs like errors and disturbances and  $g(t)$  equals the impulse response, also defined for  $(0, \infty]$ .  $t$  is the current time and  $\tau$  the process time delay. Moreover,  $(*)$  is the mathematical operator for convolution.

Input and output data are discrete measurements with the sampling time instant  $t_k = kT$  instead of continuous functions. Thus, the convolution equation for a linear system in Equation 9 is denoted as

$$y_k = y(kT) = \sum_{l=0}^{\infty} h_l \cdot u_{k-l} + v_k, \quad -\infty < k < \infty$$

Equation 10 Model for discretized input-output data

with the sampling  $k$ , the impulse response  $h(kT) = \{h_k\}_{k=0}^{\infty}$ . For discretized data the  $z$ -transform is applied to transfer this to the frequency domain, where a convolution becomes a multiplication. The  $z$ -transform is performed by applying the following equation for an input sequence  $u_k$ .

$$Z\{u_k\} = U(z) = \sum_{k=0}^{\infty} u_k \cdot z^{-k}$$

Equation 11 Unilateral  $z$ -transform of a sequence  $u_k$

$$z = r e^{j\omega}$$

**Equation 12      The complex variable  $z$  in polar coordinates**

Then, the frequency domain system response  $Y(z)$  is given with

$$Y(z) = H(z) \cdot U(z)$$

**Equation 13      The frequency-domain system response**

for the assumption of zero disturbance  $V$  [47].  $H(z)$  is the transfer function and  $U(z)$  the input data in frequency domain notation.

Another notation for a higher-order transfer function with model orders  $n_A$  and  $n_B$ , process time delay or rather sample delay  $\delta$  and an error term  $\xi_k$  is given in the following equation.

$$y_k = \frac{b_0 + b_1 z^{-1} + b_2 z^{-2} + \dots + b_m z^{-n_B}}{1 + a_1 z^{-1} + a_2 z^{-2} + \dots + a_n z^{-n_A}} \cdot u_{k-\delta} + \xi_k = \frac{B(z^{-1})}{A(z^{-1})} \cdot u_{k-\delta} + \xi_k$$

**Equation 14      The transfer function model**

Such higher-order models typically represent complex systems with several sub-systems. Figure 31 shows schematically that the identified process model contains the internal controller of the feeder, the extrusion process and the chemometric model. The sub-processes can be combined in a serial, parallel, or feedback-coupled networks and result in a total model with high complexity.

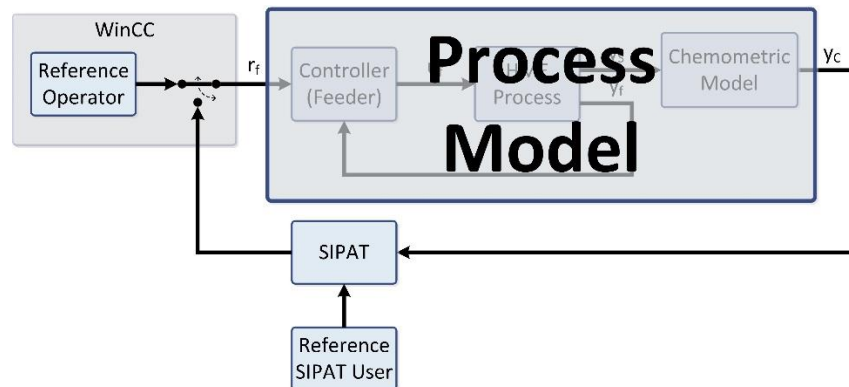


**Figure 31: The process model containing the feeder, extruder and NIR estimation model [8]**

If the coupling between the processes is known, it is possible to estimate the time constant of sub-processes. Curry, Kiani and Dreiblatt [22], for example, considered the extruder as a serial network of the different processing zones in order to gain knowledge over internal principles.

### **The Feeder Model**

The feeder sub-system with an internal controller cannot be manipulated, other than setting a certain feed rate.

The feeder behavior can hardly be considered as a linear system, because the influence of external disturbances on the scale, like airflow, or vibration is significant. These disturbances can neither be

controlled, nor measured. Even though the controllers in gravimetric feeding systems are highly sophisticated, certain disturbances cannot be evened out.

Thus, due to the non-linear dynamics of the feeder, no model can be established. Therefore, the feeder's dynamics cannot be separated from the extrusion dynamics. According to this, the feed rate fluctuations are considered as external disturbances in the overall extrusion process. Still, a characterization of the feeder is done using statistical methods to determine accuracy and constancy.

### The Chemometric Model

A chemometric model is used to predict the API concentration from the detected spectra. The model is calibrated with known API concentration levels. With the measured spectra as input and the known API concentration levels as output, the model can be identified. Figure 32(a) visualizes the identification stage and calibration process of the chemometric model.

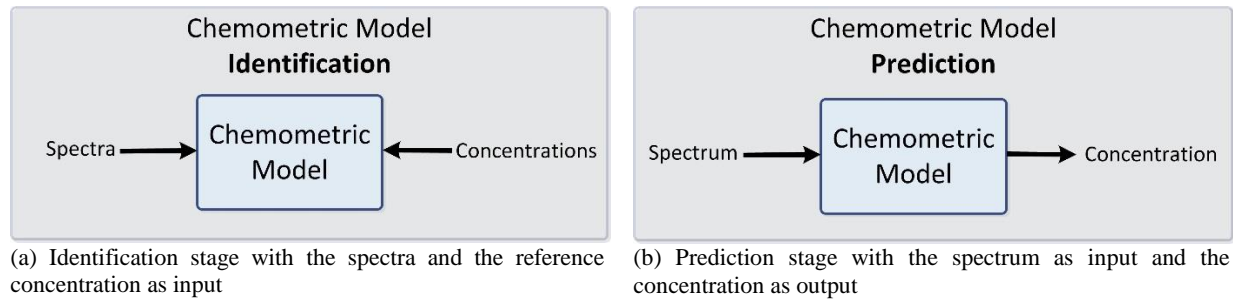


**Figure 32: Identification and prediction stage of the chemometric model [8]**

The calibration is done with in-line experimental data, because the spectra are influenced by sample presentation, melt properties and temperature and, thus, it is difficult to produce reliable off-line samples for calibration. Therefore, spectra from different concentration levels after steady state is reached are used. As NIR spectra consist of highly-correlated variables, those components containing determining information must be identified. *Principal Component Analysis* (PCA) is applied to compute the principal components of the observed spectra. Therefore, PCA reduces the amount of investigated variables, by generating linear combinations of the original variables, which are capable of describing the variance in the data [50]. The PCA approach is used in *Partial Least Square Regression* (PLS-R), to generate a linear model for highly-correlated input and output data. Moreover PLS-R is able to process data sets, with less measurements than input variables. Therefore, the multivariate data is reduced to few influential variables, the latent variables. In this case, they are identified by analyzing the covariance between the input and output data.

The PLS-R model is given in Equation 15.

$$y_k = b_0 + b_1x_{1k} + b_2x_{2k} + \dots + b_{n_{PC}}x_{n_{PC}k} + e_k$$

**Equation 15**      **PLS-R model**

$y_k$  represents the estimated scalar values (e.g., API content).  $x_{1k}$  to  $x_{n_{PC}k}$  are latent variables, which map the  $k$  input data values from the spectrum.  $e_k$  is the model error and  $b_0$  to  $b_{n_{PC}}$  stand for the model parameters. In this case, the model order is known to be zero.

The accuracy of the model is strongly dependent on reliability of the observed spectra. Thus, the location of the NIR probe is crucial for receiving spectra from a sampling volume representative for the whole material. As in-line data is used for calibration, the accuracy of the feeding system is also crucial for the quality of the model.

### **The Process Model**

As indicated previously, the process model contains both gravimetric feeders with their internal controllers, the extrusion process and the chemometric model. The internal feeder controller minimizes the deviations between the input feed rate and the measured feed rate.

The challenges for the modeling procedure are that the behavior of the feeder cannot be modeled separately and might not be reliable for small feed rates. Moreover, with feeding in split-feeding mode, feeding errors sum up and might cause severe deviations of the input API concentration value. Also, the extrusion process itself is highly complex and inhibits non-linear behavior. The API content, for example, influences viscosity and density of the melt. This relationship causes non-linear behavior. Finally, the model is highly dependent on the accuracy of the chemometric model.

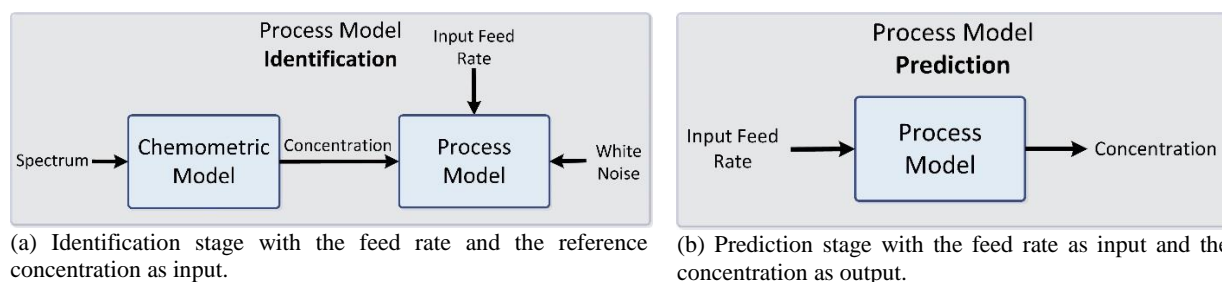


**Figure 33: Process model in identification and prediction stage [8]**

The process model relates the input feed concentration to the NIR-estimated output concentration. There are several possibilities, such as transfer function based models, state-space models and mechanistic models, for establishing this connection.

### **Transfer function based models**

Two transfer function based models will be introduced here, the ARMAX model and the Box-Jenkins model. In general, these models differ in their optimization process for estimating the model parameters in their assumptions for simplifications and in the handling of process disturbances.

The ARMAX model is used for linear models of noisy signals, because it is capable of describing the model error as a moving average of white noise. Auto-regressive (AR) means that the polynomial in the dynamic model function describes the present output in terms of past and present values of the input. The term exogenous (X) indicates that the polynomial in the disturbance model function considers past and present process disturbance values for computing the present output. Thus, the model is able to model the disturbances in the process output with a certain flexibility.

The ARMAX model is defined as follows

$$y_k = \frac{B(z^{-1})}{A(z^{-1})} \cdot u_{k-\delta} + \frac{C(z^{-1})}{A(z^{-1})} \cdot w_k$$

**Equation 16**      **The ARMAX model**

with  $w_k$  being a stochastic white noise process with variance  $\sigma_w^2$ , an expected value  $\mathcal{E}\{w_k\} = 0$  and  $\mathcal{E}\{w_i w_j^T\} = \delta_{ij} \sigma_w^2$ .  $\delta_{ij}$  as the Dirac function.

The definition of the polynomials  $A(z^{-1})$ ,  $B(z^{-1})$  and  $C(z^{-1})$  is given as

$$A(z^{-1}) = 1 + a_1 z^{-1} + a_2 z^{-2} + \dots + a_{n_A} z^{-n_A}$$

$$B(z^{-1}) = b_0 + b_1 z^{-1} + b_2 z^{-2} + \dots + b_{n_B} z^{-n_B}$$

$$C(z^{-1}) = 1 + c_1 z^{-1} + c_2 z^{-2} + \dots + c_{n_C} z^{-n_C}$$

**Equation 17**      **Polynomials in the ARMAX model**

Equation 16 can be rewritten according to

$$y_k = H(z^{-1}) \cdot u_{k-\delta} + G(z^{-1}) \cdot w_k$$

**Equation 18**      **The ARMAX model consisting of a dynamic model  $G(z^{-1})$  and a disturbance model  $H(z^{-1})$**

with the dynamic model  $H(z^{-1}) = B(z^{-1})/A(z^{-1})$  and the disturbance model  $G(z^{-1}) = C(z^{-1})/A(z^{-1})$ . A limitation of the ARMAX model is that the poles are identical in both models, resulting in varying ability to model disturbances along the process. Disturbances, like feeding variations, entering the process at the beginning dominate compared to disturbances occurring later in the process, like measurement noise.

After fitting the model to the input-output data, the estimation of new output is expressed as

$$\hat{y}_k = \boldsymbol{\phi}_k^T \cdot \hat{\boldsymbol{\theta}}$$

**Equation 19**      **Estimation of output with the estimated model parameters  $\hat{\boldsymbol{\theta}}$  and the regressor vector  $\boldsymbol{\phi}_k$**

with the estimated model parameters

$$\hat{\boldsymbol{\theta}} = [\hat{a}_1 \quad \hat{a}_2 \quad \dots \quad \hat{a}_{n_A} \quad \hat{b}_0 \quad \hat{b}_1 \quad \dots \quad \hat{b}_{n_B} \quad \hat{c}_1 \quad \hat{c}_2 \quad \dots \quad \hat{c}_{n_C}]^T$$

**Equation 20**      **Estimated model parameters from the ARMAX model**

and the regressor vector

$$\boldsymbol{\phi}_k = [-\hat{y}_{k-1} \quad \dots \quad -\hat{y}_{k-n_A} \quad u_{k-\delta} \quad \dots \quad u_{k-\delta-n_B} \quad w_{k-1} \quad \dots \quad w_{k-n_C}]^T$$

**Equation 21**      **The regressor vector for the ARMAX model**

MATLAB provides a system identification toolbox, which allows these estimations to be carried out with a predefined process time delay  $\delta$  and fixed polynomial orders  $n_A$ ,  $n_B$  and  $n_C$ . Estimation is performed minimizing the following function.

$$V(\hat{\boldsymbol{\theta}}) = \frac{1}{2} \sum_{k=1}^N (y_k - \hat{y}_k)^2$$

**Equation 22**      **The loss function, which is minimized for parameter estimation in MATLAB**

The Box-Jenkins model is based on the same approach as the ARMAX model, but gives an opportunity to model the process disturbances independently from the dynamic model. It is written as

$$y_k = \frac{B(z^{-1})}{A(z^{-1})} \cdot u_{k-\delta} + \frac{D(z^{-1})}{C(z^{-1})} \cdot w_k$$

**Equation 23**      **The Box-Jenkins model**

with the newly defined polynomials  $C(z^{-1})$  and  $D(z^{-1})$  according to

$$C(z^{-1}) = 1 + c_1 z^{-1} + c_2 z^{-2} + \dots + c_{n_C} z^{-n_C}$$

$$D(z^{-1}) = 1 + d_1 z^{-1} + d_2 z^{-2} + \dots + d_{n_D} z^{-n_D}$$

**Equation 24**      **Polynomials in the Box-Jenkins model**

Again, this model can be rewritten using the dynamic model  $H(z^{-1}) = B(z^{-1})/A(z^{-1})$  and the disturbance model  $G(z^{-1}) = D(z^{-1})/C(z^{-1})$ .

$$y_k = H(z^{-1}) \cdot u_{k-\delta} + G(z^{-1}) w_k$$

**Equation 25**      **The Box-Jenkins model consisting of a dynamic model  $G(z^{-1})$  and a disturbance model  $H(z^{-1})$**

The number of estimated parameters in the Box-Jenkins model is bigger due to the new polynomial  $D(z^{-1})$ .

$$\hat{\boldsymbol{\theta}} = [\hat{a}_1 \ \hat{a}_2 \ \dots \ \hat{a}_{n_A} \ \hat{b}_0 \ \hat{b}_1 \ \dots \ \hat{b}_{n_B} \ \hat{c}_1 \ \hat{c}_2 \ \dots \ \hat{c}_{n_C} \ \hat{d}_1 \ \hat{d}_2 \ \dots \ \hat{d}_{n_D}]^T$$

**Equation 26**      **Estimated parameters from the Box-Jenkins model**

In this case identification with predefined process time delay  $\delta$  and orders is possible in MATLAB. Parameter estimation is performed analogous to the parameter estimation for the ARMAX model using a loss function  $V$ .

### Mechanistic model

In contrast to the transfer function or state-space models, mechanistic models are white-box models. This holds the advantage of gaining insight into the physical mechanisms in the process. The disadvantage is that they cannot be used for controlling or real-time prediction purposes.

An established model for the axial dispersion is the 1D form of the Fokker-Planck equation:

$$\frac{\partial y(t)}{\partial t} = \frac{\partial c}{\partial t} = E \frac{\partial^2 c}{\partial z^2} - v_z \frac{\partial c}{\partial z}$$

**Equation 27**      **1D Fokker-Planck equation**

$c$  represents the concentration of the considered component in the system,  $v_z$  the averaged material velocity along the extruder and  $E$  denotes the diffusion coefficient in fluid systems and the dispersion coefficient in solid systems. Thus, the model assumes the axial dispersion process can be estimated by a plug flow profile with radial homogeneity superimposed by axial mixing diffusivity [51]. Taylor formulated it for different boundary conditions [52]. The most established solution for an RTD with open-open boundary conditions is formulated according to

$$E(\theta) = \frac{1}{2} \sqrt{\frac{Pe}{\pi\theta}} \exp\left\{-\frac{Pe(1-\theta)^2}{4\theta}\right\}$$

**Equation 28** Solution of the Fokker-Planck equation for the RTD formulated by Taylor [52]

where  $\theta = t/\tau$  stands for the dimensionless time with  $\tau$  as the MRT and  $Pe = v_z l/E$  representing the *Peclet number*.  $Pe$  indicates the ratio of convective flows to diffusive, or dispersive flows in the system.  $l$  stands for the distance between the injection and the detection points. According to Gao et al. [30], this model has been applied several times with good agreement also for non-single-phase and non-open-open boundary systems. This can be explained, because for high  $Pe$  the influence of boundary conditions is not significant. Moreover, they state, that this gave good results especially for rise-delayed and long-tailed RTD curves. This applies for the extrusion process also.

Todd [51] formulated a solution for the same equation for a pulse input and analysis at the exit, in order to model the RTD of a twin-screw extruder. This solution is given in the following equation.

$$\frac{C}{C_0} = \sqrt{\frac{Pe}{\pi\theta}} \exp\left\{-\frac{Pe(1-\theta)^2}{4\theta}\right\} - \frac{Pe}{2} \exp(Pe) \left[ \operatorname{erfc} \sqrt{\frac{Pe}{4}} \frac{1+\theta}{\sqrt{\theta}} \right]$$

**Equation 29** Solution of the axial dispersion equation for a pulse input and analysis at the system exit [51]

A formulation for the step change at the entrance of packed beds is given in Han et al. [53] according to Equation 30.

$$\frac{c}{C_0} = \frac{1}{2} \operatorname{erfc} \left[ \sqrt{\frac{Pe}{4\theta}} (1-\theta) \right] + \frac{1}{2} \exp(Pe) \operatorname{erfc} \left[ \sqrt{\frac{Pe}{4\theta}} (1-\theta) \right]$$

**Equation 30** Solution of the axial dispersion equation for a step-change input [53]

These two models can be fit to tracer pulse response data as well as step-change response data. With calculation of  $Pe$  it is possible to gain certain insight into the mixing process.

## 3 Materials, Methods and Experimental Design

This chapter specifies materials and equipment used in the thesis. In addition, the motivation for the choice of measurement methods and measured parameters is discussed shortly. The last part of this section describes the experimental design.

### 3.1 Materials

In this thesis, vegetable *Calcium Stearate* (CaSt) (Werba-Chem GmbH, Austria; mean particle size 16.6  $\mu\text{m}$ ) is chosen as matrix-carrier and paracetamol (GL Pharma GmbH, Austria; mean particle size 44.1  $\mu\text{m}$ ) as API. This selection was made, because knowledge about the behavior of this formulation existed from previous RTD experiments [29]. Another reason is that paracetamol exhibits difficult feeding behavior and, thus, is representative for numerous other cohesive API substances. This way, typical feeding problems can be investigated. Usually, a formulation of paracetamol and CaSt also contains different plasticizers to get a tailored API release profile [54]. In this case though, only the API and the matrix are used to simplify the system. For tracer experiments, red food dye (Color “Sissi”, Schimek, Austria, mean particle size 22.8  $\mu\text{m}$ ) is used. This color is chosen, because it results in good visibility for the video recordings of the outlet stream.

### 3.2 Methods and Process Equipment

#### 3.2.1 Extruder

The extruder used in the experiments is a co-rotating twin-screw extruder (ZSK 18, Coperion GmbH, Germany). The screw diameter is  $D_a = 18 \text{ mm}$  with a ratio of  $D_a/D_i = 1.55$  and a barrel length of  $40 \times D_a$ . Figure 34 illustrates the experimental set-up. The matrix substance CaSt is fed with a twin-screw loss-in-weight feeder (K-CL-KT20, K-Tron, Switzerland) and powder screws with small pitch. Feeding of the API paracetamol is done with a twin-screw loss-in-weight feeder for small feed rates (MT-S Hyg, Brabender Technologie GmbH & Co. KG, Germany) using a powder screw with large pitch size. The API feeder was mounted above the matrix feeder, conveying material into the same downpipe on the first barrel, as depicted in Figure 34.

The extruder has eleven barrels, each one individually tempered with a heating and cooling system, except for the inlet barrel. The barrel temperature profile and screw speed is set at the beginning of the extrusion and left constant over the experiments. The barrels 2, 3 and 9 are left open for atmospheric venting. The die plate is designed especially for the color tracer experiments. Usually, die plates have several holes through which the material exits. Thus, the decision where to measure the RTD has to be made. Due to knowledge from former experiments, the coloring from a color tracer is not identical in all available strands though, so a certain error occurs. This adaption merges all the material into a single strand, at which the RTD is measured. The die plate is tempered with a heating and cooling system.

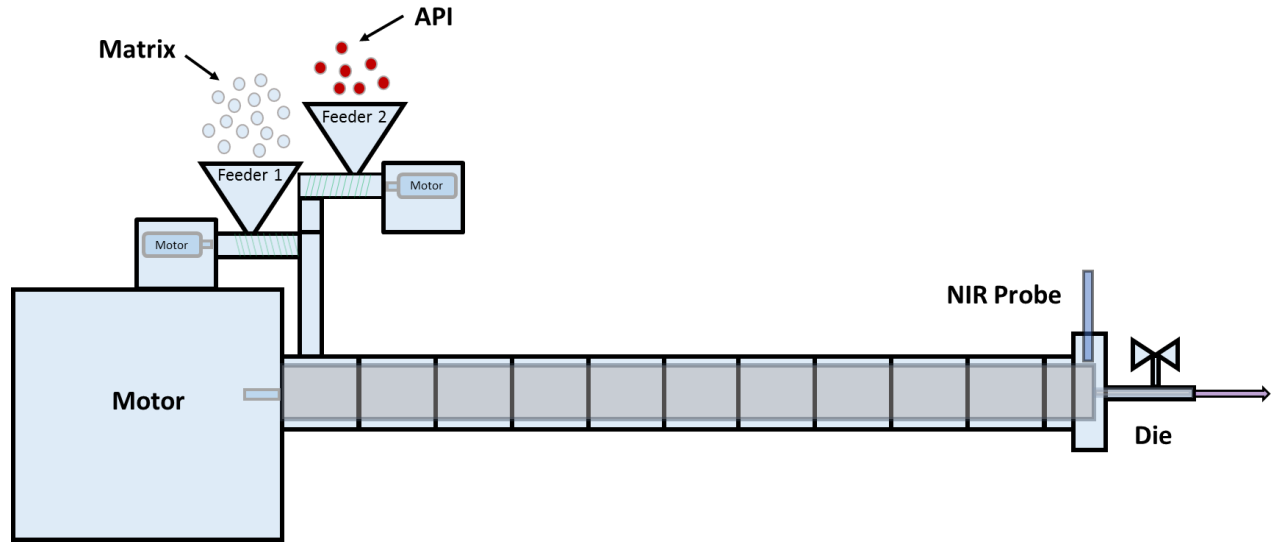


Figure 34: Illustration of the experimental set-up

Sensors for pressure and temperature as well as the NIR probe are attached to the 8-0 adapter between the last barrel and the die. Wahl et al. [29] designed a set-up for NIR spectroscopy with a metal capsule („Apollo“) in the 8-0 adapter, in order to enhance the material exchange in front of the NIR probe. Figure 35 shows the die section, in which the probe is located without the „Apollo“. The melt flow in a cylindrical channel is assumed to be between a plug flow profile (red) and a laminar flow of a Newtonian fluid (black). According to the theory of sampling by Esbensen and Paasch-Mortensen [55], material in a pressure-driven flow through a pipe should be sampled over the entire cross-section. The sample volume using in-line spectroscopic sensors is not able to cover the entire cross-section, though. It depends on the spot size, the penetration depth of the material, the transportation velocity of the material in front of the sensor and the integration time. Wahl et al. [29] calculated the sampling volume according to Equation 31.

$$V_{Sample} = \frac{d^2}{4} \cdot \pi \cdot \lambda + t \cdot d \cdot \int_{R-\lambda}^R v(r) dr$$

Equation 31 Approximation of NIR sample volume according to Wahl et al. [29]

with  $d$  being the diameter of the illuminated spot under the probe,  $\lambda$  the penetration depth,  $v(r)$  the velocity of the material,  $R$  the radius of the die section and  $t$  the integration time. The first term in the formula is determined by the geometry of the probe and the optical melt properties. It represents the volume of material captured by the probe, if there is no flow in the extruder. The penetration depth is estimated to be 500  $\mu\text{m}$  for an opaque CaSt-paracetamol melt with high drug loading [29]. The second term in Equation 31 represents the volume increase of the sampling volume due to the material movement under the probe, assuming a fully developed Newtonian flow. This term is influenced by the flow velocity of the melt and can be influenced by changing the throughput, or by reducing the channel geometry. The sample volume for a pipe flow (without Apollo) is calculated as  $V_{Sample} = 3.6 \text{ mm}^3$  (with  $d = 3 \text{ mm}$ ,  $\lambda = 500 \mu\text{m}$ ,  $R = 9 \text{ mm}$ ,  $t = 0.84 \text{ s}$ , the mass flow  $\dot{M} = 0.5 \text{ kg/h}$  and an averaged density for 20 to 50% API content  $\rho_m = 1150 \text{ kg/m}^3$ ) from Equation 31. The sampling volume with the Apollo ( $R_i = 7.4 \text{ mm}$ ) inserted in the die section

becomes  $V_{Sample} = 4.9 \text{ mm}^3$ . Thus, it can be seen, that reduction of the free cross-section is essential to enhance material renewal in front of the probe.

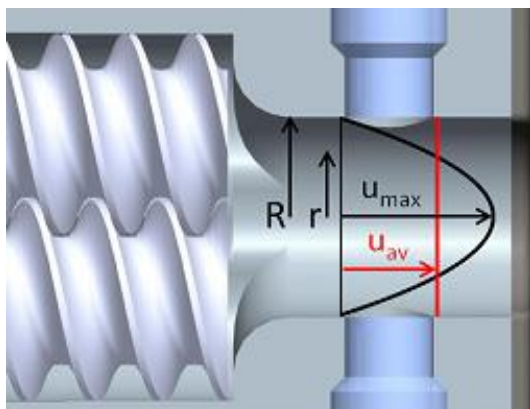


**Figure 35:** Die section of the extruder where a NIR probe is situated. The black flow profile represents the pressure-driven pipe flow of a Newtonian melt with the maximal velocity  $u_{max}$  in the center. The red velocity profile represents the case of perfect plug flow with  $u_{av}$ . (adapted from [29])

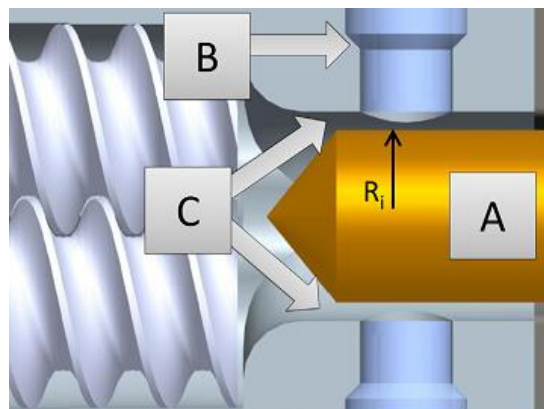


**Figure 36:** Modification of the die section and probe: (A) Filling the large melt volume with a tapered metal cylinder (“Apollo” capsule, radius  $R_i$ ) forming an annular channel at the walls. (B) Turning the  $45^\circ$  face of the probe 1 mm to ensure a nearly planar transition between the probe and the barrel wall. (C) This leads to an annular flow of the melt [29]

### 3.2.2 Light Microscopy

The extruded material was examined under a microscope, in order to gain insight into integration of crystalline paracetamol into the molten matrix substance CaSt. Therefore, the light microscope DM4000 B (Leica Microsystems, Germany) was used. The raw API substance was also examined separately to investigate whether the particle size of the crystals is reduced during the extrusion process.

There is no sample preparation done for pure paracetamol. The powder is simply distributed on an object plate. The preparation of the extruded strands is done by heating the extrudate on an object plate and flattening it with a second glass plate in order to get a planar face for examination under the microscope.

### 3.2.3 Catch Scale for Feeder Evaluation

The feeding accuracy is evaluated in feeding experiments. Therefore, a catch scale was placed under the feeder outlet (Figure 37).

The feed rate is calculated from the amount of powder feed in each measurement interval. The feeding experiments are performed with two different scales. For the experiments with the K-Tron feeder, the New Classic MF – MS8001SE (Mettler Toledo, Switzerland) scale was used. It has a measurement frequency of 10 Hz, a weighing range of up to 8 kg and a resolution of 0.1 g. For the API feeder, the laboratory scale Sartorius AW224 (Sartorius AG, Germany) with a maximal weight of 220 g, a resolution of 0.0001 g and a measurement frequency of 1 Hz was used, because the model from Mettler Toledo is not able to resolve such small feed rates sufficiently. Moreover, it is necessary to place a bucket on the scale to collect the powder and this adds some “dead weight”, which reduces the weighing range of the scale. In case of long-time testing, the collection bucket becomes full and has to be exchanged. For data analysis these disturbances must be excluded.

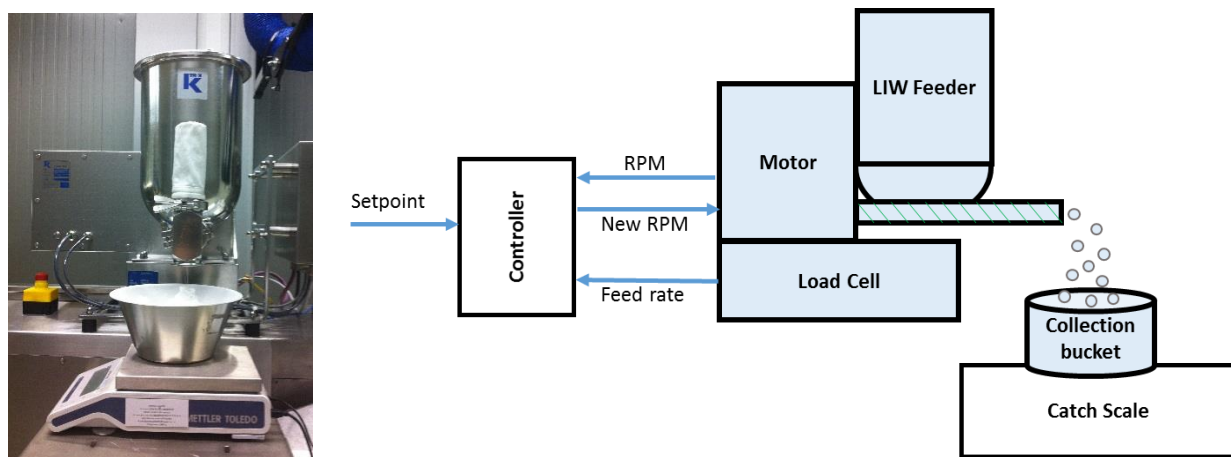


Figure 37: Set-up for feeding experiments

### 3.2.4 Real-Time Monitoring of the Experiments

SIPAT (Siemens AG, Belgium) is used as a PAT software solution. All collected process data was time-aligned as described in the introduction. In addition, the feeders were both integrated in SIPAT. For the API feeder, a manual integration via Modbus and a custom LabVIEW tool is necessary. It is important that the sampling rate from a collector station is lower than the rate from the individual sensors. The sampling rate for each sensor was chosen as a trade-off between minimizing noise and getting enough information about the dynamics of the system. The sampling rate for SIPAT was set at one measurement per second.

### 3.2.5 NIR Spectroscopy

The fibre-optic Dynisco NIR probe is used in transflexion mode with the process spectrometer SentroPAT FO (Sentronic GmbH, Germany). The spectral range is 1100-2200 nm with a resolution of 2 nm. The probe is screwed into the 8-0 connector as described in the extruder set-up above for in-line measurements. The integration time per spectrum was 0.014 s with 60 averaged spectra. Thus, the total integration time is 0.84 s. Such a short sampling time was selected in order to facilitate data collection via SIPAT with 1 Hz recording frequency.

### 3.2.6 Chemometric Model

The software Simca P+ 12.0 (Umetrics, Sweden) is used to develop the chemometric model. An in-line calibration method according to Wahl et al. [29] is applied. Data pre-processing is performed in order to reduce signal noise (statistical filtering of the signal), or to perform a baseline-correction-normalization enhancement [56]. First a *Standard Normal Variate* (SNV) transformation is used, and second, a second-order derivative with Savitzky-Golay smoothing, according to the method from Wahl et al. [29] is applied. Then PLS-R is used to generate the model for the API content prediction. Figure 38 illustrates, that the variation in the API content between 10 to 40% is linear and can be explained by the first (PC1) and second (PC2) principal component of the data set.

As the melt of the pure matrix substance is more translucent compared to the extrudate with API, the optical properties change drastically from 0 to 10 % API content. Figure 39 shows the chemometric model from the publication of Wahl et al. [29]. The reliability for cross-validation with the model below 10 and above 50% is limited. Therefore, a range from 10 to 40% is chosen for the API content in the experiments.

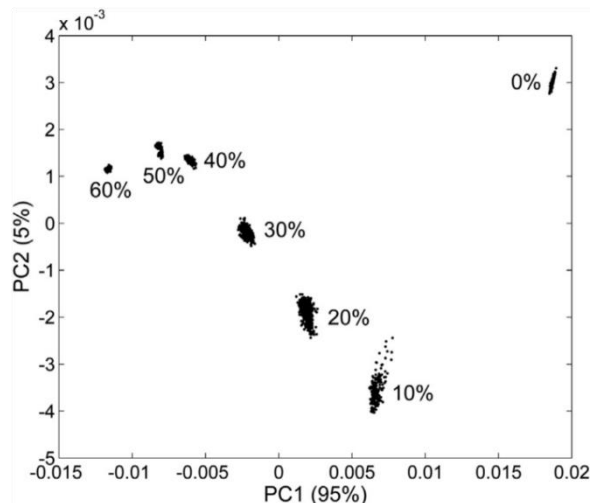


**Figure 38:** PC1 and PC2 of the model spectra. The PCA was performed in the same spectral range as the model [29]

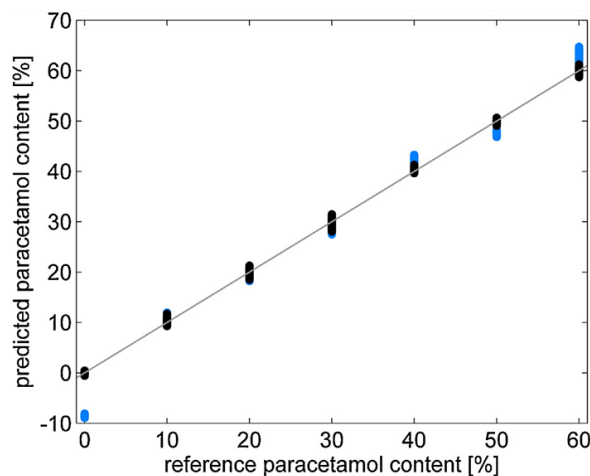


**Figure 39:** Chemometric model in [29] from 0 to 60 % API (paracetamol) content in the melt with  $R^2=0.999$  (black),  $Q^2=0.974$  (blue) and four latent variables. Due to the non-linear behavior at a low API content, the cross validation (blue) of the 0% group failed.

### 3.2.7 Optical RTD Measurements

For analysis of the RTD in the color tracer experiments a digital camera (Finepix HS 25 EXR, Fujifilm, Japan) was used. The experiments were recorded with the video function of the camera and the pictures were analyzed with a MATLAB routine. The camera was placed in front of the extrusion die, as illustrated in Figure 40.

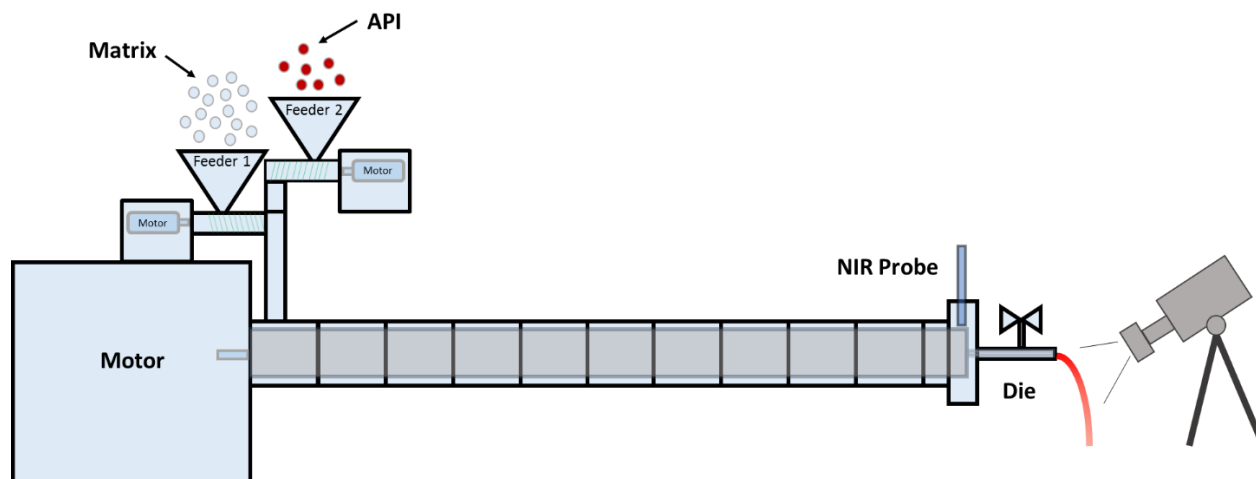


**Figure 40:** Set-up for optical RTD measurements

In order to enhance the visibility of the strand, a black background was mounted on the outlet pipe from the die plate. The outlet stream was monitored with a camera for 15 minutes and the residence time for the color pigments was evaluated by analyzing the brightness of the outlet strand. The more pigments are in the extrudate, the darker it gets. In principle, there is a second approach available to performing the video analysis, by taking the redness of the strand as a measure for the color intensity. The redness is evaluated using the deviations in the *red-green-blue* (RGB) channels from a defined white balance. The brightness approach is chosen in this case, because of the occasional presence of water in the extrudate. The color used in the experiment is water dissolvable and appears almost black when dissolved in a water drop on the strand.

In addition, the API concentration is simultaneously acquired using a NIR probe in the 8-0 adapter of the extruder. As the extrudate has to run through the die plate with the valve afterwards, the residence time for the tracer RTD is expected to be longer than from the NIR estimation.

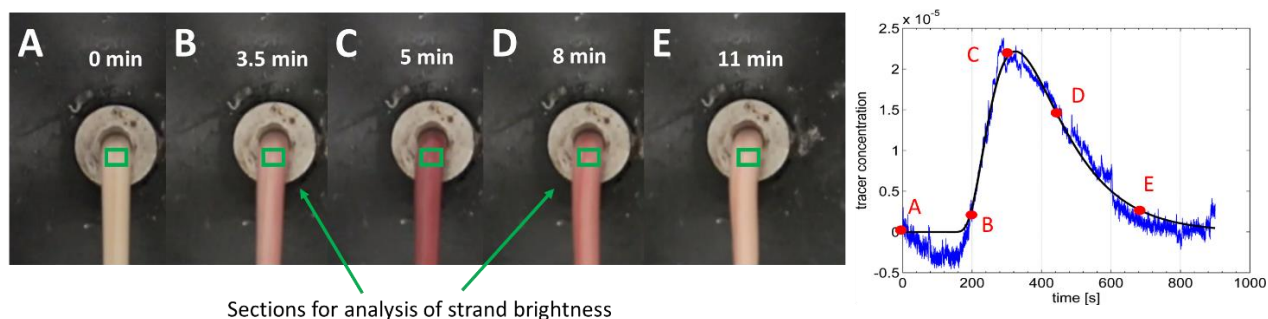


Figure 41: Color tracer experiment with 20% API content and the outlet valve open

### 3.2.8 Data Analysis and System Identification

MATLAB 2010b is used for data analysis and calculations in this thesis. The feeding experiments are evaluated statistically and a frequency analysis is also performed. The color tracer recordings are processed with a MATLAB script written by Patrick Wahl at RCPE GmbH, Graz. The script evaluates the brightness in a certain picture area resulting in a brightness curve. This curve is identical with the RTD of the tracer and is used for a fit with the axial dispersion model as given in the “Relevant Models” section using the “nlinfit” command in MATLAB. This command uses a Levenberg-Marquardt non-linear least squares algorithm for parameter estimation.

The output data from the NIR estimation is used to perform a statistical analysis of the stability and accuracy of the extrusion process and also fitting of the axial dispersion model to the step-change experiments is also done in MATLAB.

The system identification is performed using the system identification toolbox. The input signal is the entrance API concentration, calculated from the feed rates displayed by the two feeders. The output is the API concentration estimated via NIR. Models used for system identification (ARMAX, Box-Jenkins) are explained in “System Identification”.

### 3.3 Experimental Design

The experimental design comprises three main types of experiments. First, the feeding accuracy is of key importance for the success of the experiment. In contrast to the previous work [29], the feeding strategy is chosen as split-feeding of pure substances instead of premixes. The accuracy of both feeders is tested with the catch scale set-up, described in the “Catch Scale for Feeder Evaluation” section. Secondly, a step experiment yields RTDs based on both the NIR concentration measurement and the addition of a color tracer. The RTDs are the basis for the mixing model development. Third, a PRBS input concentration is performed to generate and validate the mixing model by comparison between the model and measured concentration curves at the extruder outlet.

The experimental design is based on previous work from Wahl et al. and Markl et al. at RCPE [8], [29]. The throughput is chosen to be constant at 0.5 kg/h and the concentration varies between 20 and 50% API content.

#### 3.3.1 Feeding Experiments

The absolute feed rates were selected regarding the range in which the feeders they are capable to dose accurately and the capability of the extruder to take in the overall throughput. Table 2 summarizes the feed rates of the feeding units for the required concentrations in order to determine the feeder accuracy. A rule of thumb from the feeding practice is that the screw speed at a set feed rate should lie in the range of 20 to 80% of the maximal screw speed. In previous extrusions, a maximum overall throughput of 0.6 kg/h was found to be doable for this material system. Higher throughputs cause problems in the intake zone.

The concentration levels were chosen according to the range of validity for the chemometric model and aspects like a good SNR. Thus, for the step-change sequence, an API concentration step size of 10% was selected, within a range of 20 to 50%. For the PRBS sequence 20% changes, between 16 and 36% were performed. The concentration level for the PRBS sequence were selected to be different from the levels in the step-change pyramid, in order to have some more concentration points within the range of linearity.

**Table 2** Selected feed rates

<b>Experiment</b>	<b>API concentration [%]</b>	<b>Feed rate API [kg/h] (Brabender)</b>	<b>Feed rate Matrix [kg/h] (K-Tron)</b>
<b>Step</b>	20	0.1	0.4
<b>Step</b>	30	0.15	0.35
<b>Step</b>	40	0.2	0.3
<b>Step</b>	50	0.25	0.25
<b>PRBS</b>	16	0.08	0.42
<b>PRBS</b>	36	0.18	0.32

Figure 42 illustrates the experimental design for the feeding experiments. Data from the concentration pyramid is to be evaluated concerning feeding stability and accuracy. In order to get an impression over the behavior in the PRBS sequence in the extrusion, a short PRBS sequence is also added to the step-change pyramid.

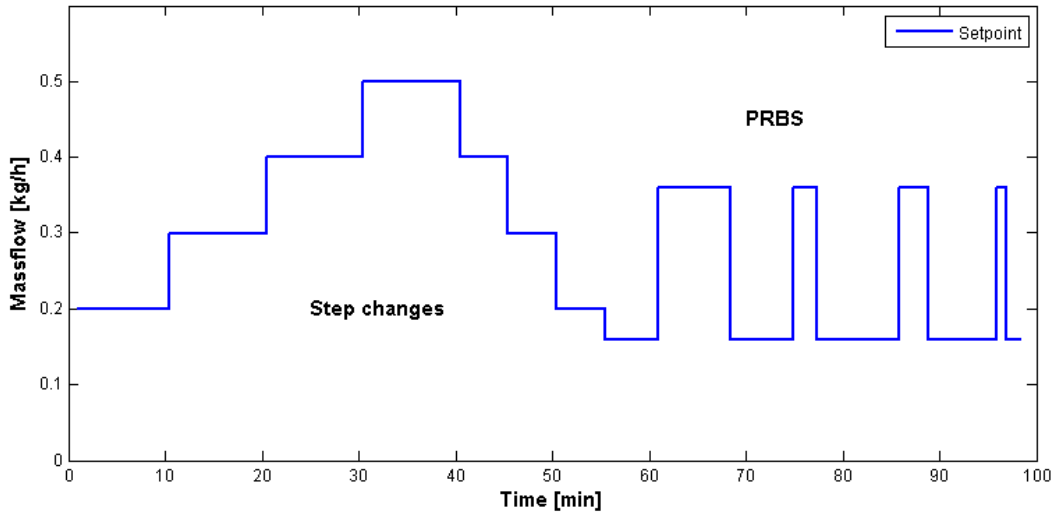


Figure 42: Experimental design for feeding experiments

### 3.3.2 Extrusion Step-Change Experiment

Figure 43 shows the set-point concentration curve. The transition regions of the measured concentrations curve between the constant levels are used to derive the NIR-based RTD. In addition, color tracers are added for optical RTD measurements. The idea is to compare the NIR-based RTD with the optical RTDs. The optical RTD measurements were performed at constant concentration levels and in the transition regions. The tracer addition times are indicated as “o” markers in the concentration curve. This corresponds to a steady-state and unsteady-state measurement.

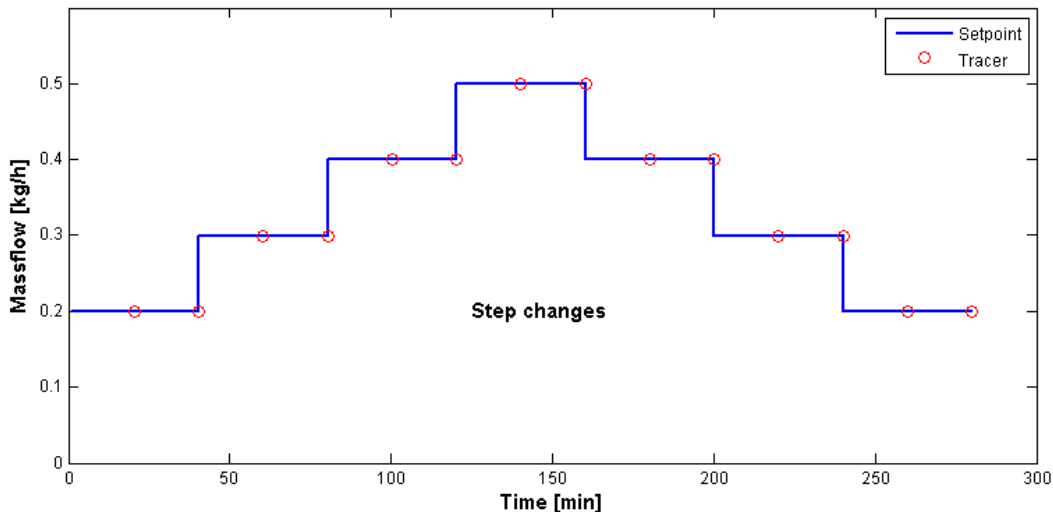


Figure 43: Step experiment design for color tracer experiments with simultaneous NIR estimation

The red tracer color is added to the barrel with the feed inlet at each concentration level as well as simultaneously with each change in concentration. This is done in order to investigate the dynamics during a step change influencing the RTD. In pre-experiments, the wash-out time of the color tracer was found to be below 15 minutes for all concentration levels. Together with 5 minutes of preparation time for the new video recording and the tracer, this sums up to 20 minutes between the tracer inputs. Thus, the length of a step level is 40 minutes.

### 3.3.3 System Identification Experiment

For system identification, a PRBS part is added to the concentration pyramid design from the color tracer experiments. The duration for each step level is shortened to 10 minutes, in order to save time and material. The PRBS is a test signal, which is applied to test the system response on a random frequency input signal with only two signal amplitude levels. This experimental design allows to identify models (e.g., ARMAX, Box-Jenkins), which are valid for wide frequency ranges. Figure 44 shows the experimental design for the concentration pyramid and the PRBS part. The levels of the binary signal are chosen as 16 and 36%. The signal amplitude is selected based on the knowledge that the range of linear relationship between NIR spectra and API concentration lies between 10 and 40% and with the purpose of keeping the SNR as large as possible. The choice of the excitation frequency is made considering minimum residence times from previous experiments [8], [29]. To capture all the dynamics, the interval between the changes is chosen as random multiples of 30 seconds ranging from 30 seconds up to 8 minutes.

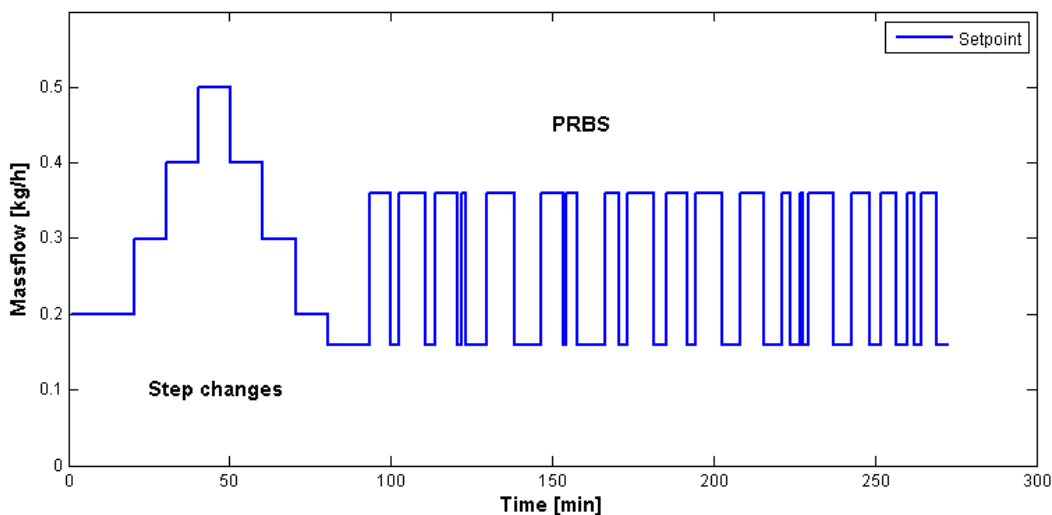


Figure 44: Experimental design for system identification

## 4 Results and Discussion

In this chapter, the results from the individual experiments are shown and analyzed. In addition, possible sources for errors are noted and improvements for further research are proposed. In the final chapter “Summary and Conclusions”, individual results are linked and the key findings are highlighted.

### 4.1 Feeding Experiments

The feeding experiments were performed according to the experimental design (Figure 42). Data from the feeding experiments was evaluated using a self-written MATLAB script. Disturbances like exchanging the collection bucket on the catch scale are filtered out in pre-processing. Moreover, the data is smoothed over different time spans using a moving average filter. The raw catch scale signal showed high fluctuations due to oscillations induced by dropping powder during dynamic weighing. These fluctuations occur due to low eigenfrequencies of both catch scales used in the experiments. The eigenfrequency is a measure for the typical settling time after a stimulus like a powder agglomerate falling on the scale, for example. In addition, the low measurement frequency in one case (API feeding) and the low weight resolution in the other case (matrix feeding) amplify the fluctuations. The smoothed data is plotted together with the set-point and a tolerance band for deviations, in order to get an impression of the feeding performance. For further analysis each feed rate level in the concentration pyramid is analyzed separately, investigating feeder constancy and accuracy. This is done using boxplots for visualization and calculating statistical parameters like arithmetic mean, standard deviation and relative standard deviation for each feed rate level. Finally, a frequency analysis of the feeding data is conducted.

#### 4.1.1 Matrix Feeder (Ktron KT20)

Figure 45 shows the set feed rate and processed feed rate calculated from the scale data and from the feeder display. The graph gives the feed rates for the matrix feeder and thus, has the inverted shape of the experimental design (Figure 42), in which the experimental design was given in API concentration. The thresholds for 5% deviations from the set-point, forming a tolerance band for the feed rates are shown. The tolerance band is selected to be sufficient for an acceptable CU limit as defined in “Introduction”. While the feed rate displayed by the feeder crosses the 5% thresholds only four times, the feed rates calculated from the scale signal shows more than 20 out-of-spec incidents even if smoothed over 60 seconds. Moreover, it is interesting to see, that the deviations indicated by the feeder display are not always visible in the signal from the catch scale. Especially, the big deviation on step 5 is visible only in the feeder display data. For these cases, it can be assumed that the gravimetric control was irritated by an external disturbance, or the internal data processing, e.g. a filter, causes these tremendous deviations.

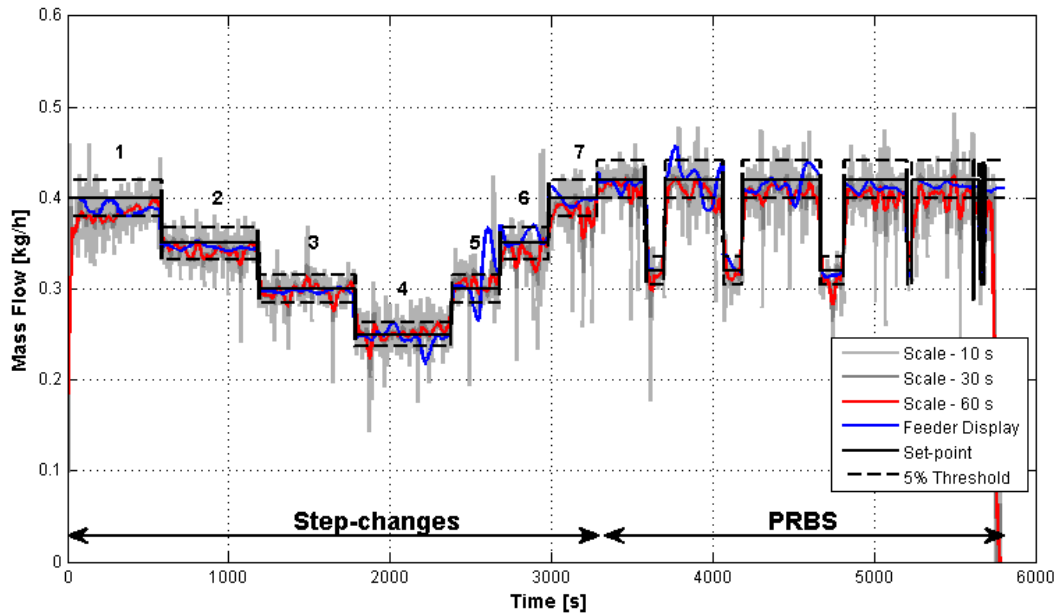


**Figure 45: Matrix feeder and catch scale data comparison including set-point and 5% tolerance band**

Figure 46 shows the boxplots at the step levels for the feeding experiment. In the left graph, the feed rates displayed by the feeder are analyzed. The graph in the middle shows data from the catch scale smoothed over five seconds and the right graph data smoothed over 60 seconds. These smoothing spans are chosen, because it can be assumed that fluctuations over five seconds should be dampened out by the feeder. However, the catch scale fluctuations observed at such short time spans are superimposed feeding oscillations and natural oscillations of the measurement set-up. Thus, the smoothing over 60 seconds is also evaluated to analyze low-frequency fluctuations which pass almost undampened through the process, affecting the product quality. A boxplot is used to visualize an averaged value for a data set, as well as the range of the quartiles. The median value is illustrated with a red line and allows to analyze overall deviations from the set-point. They show significant deviations from the set-point, especially the median at 0.4 kg/h calculated from the scale signal. This tendency can also be observed by looking at the smoothed-over scale signal (red line) in Figure 45, where the feed rate is always smaller than the set-point. The blue boxes in Figure 46 indicate the interquartile range (IQR). This means it indicates the range between the 25% quartile and the 75% quartile. Data from the feeder display shows varying IQR size. However, no connection to the feed rate value is visible. Thus, it can be assumed, that these deviations are caused by external disturbances. Data from the scale, smoothed over five seconds displays relative constant sizes for the IQR. The quartiles are found to be around 2 kg/h above or below the median values. The IQR for data smoothed over 60 seconds is free of noise caused by natural oscillations. For the first five steps it was found to be below 0.5 kg/h, which is quite good. Symmetry of the IQR boxes indicates a normal distribution of the feed rate fluctuations, which means random fluctuations around the set-point. The IQR for the scale signal smoothed over five seconds is quite symmetrical, while smoothing over 60 seconds reveals an asymmetric IQR for steps six and seven. It is not possible, though, to connect this to specific reasons for this behavior. The whiskers above and underneath the blue boxes indicate the spread of the data within 1.5 x IQR. The data smoothed over 60 seconds reveals a trend to shorter whisker length for smaller feed rates and longer step level duration. The red crosses in the plot indicate outliers. Due to the high measurement frequency and the

big data set, many of them are indicated for the data smoothed over five seconds. For the data smoothed over 60 seconds, the highest number of outliers can be found at the steps three and four.

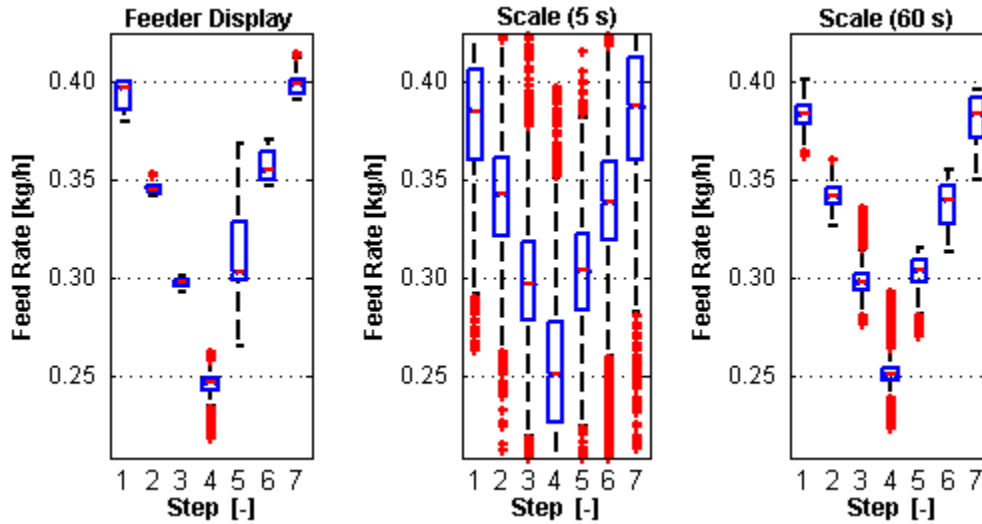


Figure 46: Boxplots for each feed rate level (5 s smoothing) for the matrix feeder

Another statistical evaluation of the feeding accuracy was performed by calculating the arithmetic mean, indicating the feeder accuracy and the standard deviation for each concentration level on the concentration pyramid, which last for 10 minutes and, accordingly, inhibit approximately 6000 data points. The latter indicates the range over which the feed rate spreads. Moreover, an averaged relative deviation from the calculated feed rate to the set feed rate according to Equation 32 is computed.

$$rel.Dev_{m-set} = \frac{\bar{m} - \dot{m}_{Set}}{\dot{m}_{Set}} \cdot 100 \%$$

**Equation 32** Calculation of the relative mean set-point deviation using the mean feed rate and the set feed rate

The calculated feed rate  $\bar{m}$  is the mean feed rate derived from the weight increase on the scale. Again, two smoothing spans (5 and 60 seconds) are evaluated. The results are summarized in Table 3. The values are rounded and, thus, the relative mean set-point deviation differs in some cases for same mean values.

The deviation of the calculated mean from the feeder set-point on the display is maximal at 12 g/h (step five). This step also holds the biggest standard deviation (28.2 g/h) and a relative mean set-point deviation of 3.9%. As this is the only step with such big deviations though, it is very likely that exceptional external influences caused these results. The rest of the steps have a standard deviation below 10 g/h, resulting in absolute values for the relative mean set-point deviations between 0.3 and 1.9%. This accuracy would be satisfactory for solid drug production.

Table 3 Statistical evaluation of the K-Tron feeding experiments

#	$\dot{m}_{Set}$ [kg/h]	Feeder display			Catch scale (5 s)			Catch scale (60 s)		
		$\bar{m}$ [kg/h]	$s$ [kg/h]	$Dev_{\bar{m}-Set}$ [%]	$\bar{m}$ [kg/h]	$s$ [kg/h]	$Dev_{\bar{m}-Set}$ [%]	$\bar{m}$ [kg/h]	$s$ [kg/h]	$Dev_{\bar{m}-Set}$ [%]
1	0.40	0.393	0.0074	-1.81	0.384	0.0372	-4.00	0.383	0.0072	-4.21
2	0.35	0.345	0.0033	-1.31	0.341	0.0314	-2.57	0.342	0.0063	-2.32
3	0.30	0.297	0.0028	-0.86	0.298	0.0334	-0.67	0.298	0.0087	-0.79
4	0.25	0.246	0.0092	-1.57	0.251	0.0424	0.40	0.252	0.0088	0.64
5	0.30	0.312	0.0282	3.90	0.304	0.0429	1.33	0.303	0.0082	1.02
6	0.35	0.357	0.0085	1.92	0.338	0.0560	-3.43	0.338	0.0105	-3.48
7	0.40	0.399	0.0069	-0.31	0.380	0.0524	-5.00	0.381	0.0119	-4.87

Data smoothed over five seconds from the catch scale indicates the biggest deviations from mean value to the set-point for step number seven (20 g/h) and a relative mean set-point deviation for step seven with -5%. The biggest standard deviation was found on step six (56 g/h). Analysis of the data smoothed over 60 seconds results in the same findings. Only the relative standard deviation also has its maximum on step seven (11.9 g/h). This analysis does not indicate an outlier result though, because several steps lie in a similar value range. The deviation of the mean value at different smoothing spans is caused by boundary effects. Data from before the step change affects the data right after the step change. The same occurs at the end of each step data set. The 60 second averaged data shows standard deviations in the same magnitude as the feeder display data. The superposition of the catch scale's natural oscillation and dropping powder cause high fluctuation, as can be seen by high standard deviations for the five second averaged catch scale data, which is approximately 5 times higher than the 60 seconds standard deviation. In general, it can be concluded from all data sets that the feed rate is below the set value for the steps at the highest feed rates and that the accuracy is slightly better for smaller feed rates.

Due to the slow settling times (one second for Mettler Toledo MF – MS8001SE) for the catch scale, combined with the resolution issue discussed before, further investigation with dedicated equipment is recommended to analyze high frequency fluctuations. It is very likely, that the noise is caused by the dynamic behavior of the scale. Besides that, the experiment was conducted in an area exposed to numerous possible external influences like air gusts, for example. The feeder is capable in controlling such disturbances, but the scale is influenced directly.

Finally, a frequency analysis is performed by applying a Fourier transform to the raw data from the first four steps on the concentration pyramid. Such an analysis is done in order to identify dominant frequencies in the feeding process. Therefore, the data is transformed into a frequency domain similar to the approach for the z-transform introduced in Chapter 2.2. In contrast to the z-transform though, a discrete Fourier

transform is usually applied to periodic input signals instead of transient response analysis. The Fourier transform can be performed easily using the fast Fourier transform command in MATLAB. The first four levels are chosen for analysis as they inhibit more data points than the shorter steps or the PRBS part. The measurement rate is 10 Hz. To avoid aliasing of the signals, a frequency analysis is performed up to half the measurement frequency only. The FFT spectra are displayed in a range from 0 to 5 Hz, whereby the upper limit results from the Nyquist-Shannon sampling theorem. Peaks in the data set indicate a dominant frequency. The first peak in the spectrum shifts to the left for higher feed rates. This indicates, that the first peak could represent the feeding screw's rotational speed. Other peaks are visible especially for the feed rate of 0.4 kg/h. The source for these peaks is not easy to identify. Another possible origin of peaks in a frequency spectrum for feeders is the movement of the agitator [36]. Moreover, some peaks might represent resonance frequencies of the scale excited by powder agglomerates falling into the collection bucket. This scale has a typical settling time of one second and according to a rule of thumb, the eigenfrequency for scales is approximately  $1/(2 \cdot \textit{settling time})$ . Accordingly, the eigenfrequency of this scale is around 0.5 Hz. This is visible in the frequency analysis, as a small peak can be found at 0.5 Hz for all feed rates. Otherwise it is not possible to assign the peaks to individual processes. This emphasizes the necessity for further investigation, with a catch scale with a faster settling time, a higher resolution and a higher sampling frequency. Furthermore, it might be possible to characterize agglomeration of a powder on the feeder outlet with such an approach.

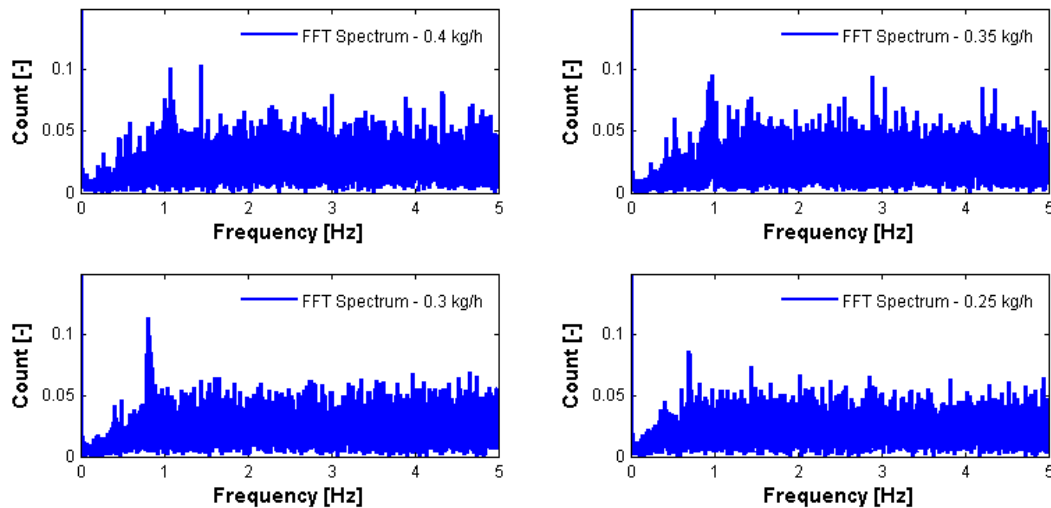


Figure 47: Frequency analysis of the matrix feeding signal for steps one (0.4 kg/h) to four (0.25 kg/h)

### 4.1.2 API Feeder (Brabender MT-S Hyg)

Figure 48 shows the experimental data from the feeding experiment with the API feeder. Again, the values displayed by the feeder and the values calculated from the scale signal are visualized. The measurements are smoothed over different time spans to remove fluctuations from the raw signal. The set-points and tolerance bands accepted in solid drug manufacturing are indicated in black.

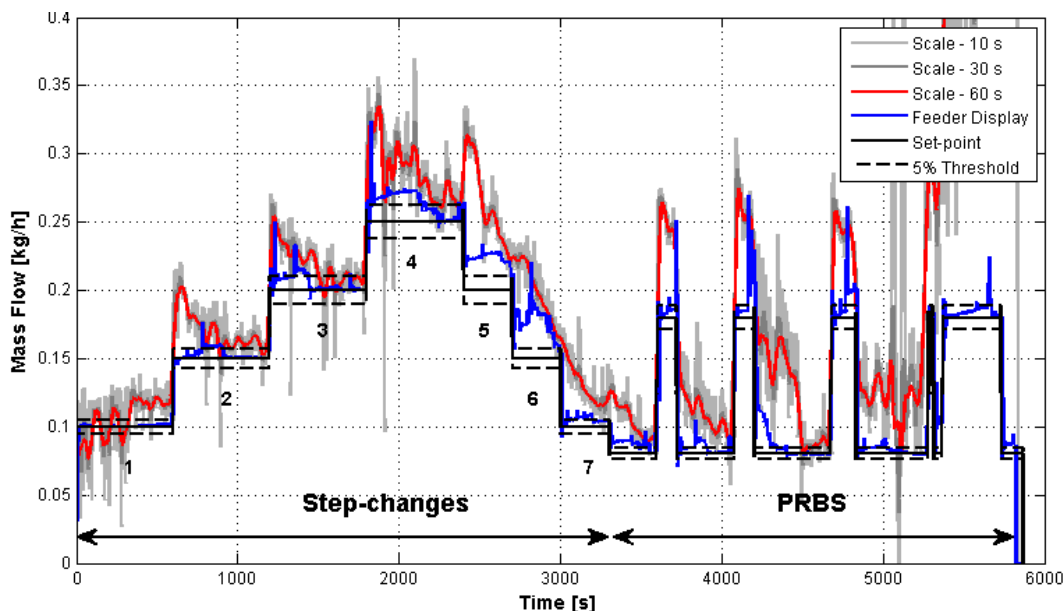


Figure 48: API feeder and catch scale data comparison including set-point and 5% tolerance band

As paracetamol is a very cohesive material, it inhibits a tendency to form bridges and holes in the hopper during the feeding process. Figure 49 shows the formation of a hole in which the agitator was rotating during the experiment. Thus, only a limited amount of material was lying on the screw, available to refill the empty screw flights. In such a case, the controller reacts with increased screw speed and the effect can be compensated for a certain time. When there is no material refilling the screw anymore though, the feed rate finally drops. In order to keep an extrusion running for a longer time it is necessary to break those bridges from time to time. This was done manually by carefully destabilizing these bridges with a wooden stick. As the screw speed was already increased due to the smaller filling level in the screws, the feeder dosed a bigger amount of material than intended. It takes the controller a certain amount of time to adapt the screw speed to the new bulk properties in the hoppers and the mechanism starts all over again.

A general trend visible in Figure 48 is, that the values are too high on average. This trend can also be found in the boxplot in Figure 50. Both the feeder display and the scale data indicate this as the median values are higher than the set-point for every level. Moreover, heavy overshooting can be observed after each step change in Figure 48. After approximately five minutes, the new set-point is reached. At the shorter steps to a lower feed rate, the new set-point is not reached. In the PRBS part, the feeder is, again, not capable of settling at the new feed rate for the short durations for each level. Especially at the second to last PRBS structure, the feeder was unable to control the feed rate anymore. It is assumed, that this happened due to the fast change between high and low feed rate levels combined with a factory-made delayed control of the feeding equipment. In addition, the effect of cohesive powder behavior and the necessity of manual destabilization of bridges in the hopper deteriorates the feeder's raw signals.



**Figure 49:** Cohesive powders tend to build bridges in the hopper, causing formation of an empty hole around the agitator

The boxplots confirm the observation of fluctuation in screw-filling grade, as it indicates that deviations of the median, the IQR and the whisker length increases with increased feed rate. A higher feed rate intensifies the effect of bridging and breaking the bridges, as the material in the hole around the rotating agitator is emptied faster compared to smaller feed rates. The fact that the data on the first step inhibits the best accuracy shows that the continuing deterioration of the controller may cause such large feeding deviations. The boxplot for data from the catch scale shows that the feeder has serious problems when a feed rate is kept constant for a short time only. The controller is unable to compensate neither for the fluctuations brought in by bridge-breaking, nor for the adaption of the control value due to a new set-point. Thus, the median values of steps five to seven indicate severe deviations from the targeted feed rate.

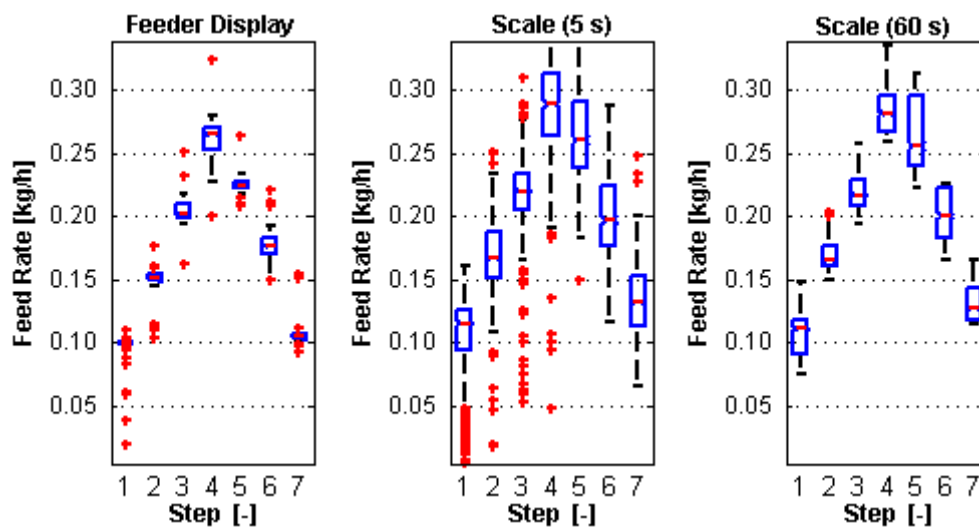


**Figure 50:** Boxplots for each federate level for the API feeder

The results from the statistical data analysis are summarized in Table 4. The statistics from this experiment draw a similar picture in good accordance with the previous results. The largest deviation of the mean for the feeder display data can be found on step six (27 g/h), together with the biggest standard deviation (12 g/h) and relative mean set-point deviation (18%). Again, it can be concluded that the main feeding problems occur right after a set-point change, as the variations for the shorter descending steps are bigger. For step-ups the standard deviation lies between 7 and 10 g/h and the absolute values for the relative mean set-point deviation between 0.37 and 5%. The step-down data features bigger relative mean set-point deviations (6 to 18%) which would be too high for solid drug manufacturing product quality.

Table 4 Statistical evaluation of the API feeding experiments

#	$\dot{m}_{Set}$ [kg/h]	Feeder display			Catch scale (5 s)			Catch scale (60 s)		
		$\bar{m}$ [kg/h]	$s$ [kg/h]	$Dev_{\bar{m}-Set}$ [%]	$\bar{m}$ [kg/h]	$s$ [kg/h]	$Dev_{\bar{m}-Set}$ [%]	$\bar{m}$ [kg/h]	$s$ [kg/h]	$Dev_{\bar{m}-Set}$ [%]
1	0.10	0.100	0.0070	-0.37	0.105	0.0328	4.84	0.105	0.0148	5.36
2	0.15	0.152	0.0059	1.48	0.169	0.0284	12.88	0.169	0.0134	12.89
3	0.20	0.205	0.0067	2.39	0.219	0.0308	9.28	0.219	0.0143	9.49
4	0.25	0.263	0.0102	5.05	0.286	0.0452	14.46	0.285	0.0196	14.12
5	0.20	0.225	0.0074	12.51	0.265	0.0380	32.33	0.264	0.0295	32.08
6	0.15	0.177	0.0120	18.05	0.200	0.0327	33.64	0.200	0.0204	33.33
7	0.10	0.106	0.0080	6.36	0.134	0.0281	33.76	0.132	0.0154	32.24

Analysis of scale data smoothed over five seconds results in similar findings. The step-ups inhibit better accuracy with relative mean set-point deviation between 4 and 14.5% compared to the step-downs (around 33%). Smoothing over 60 seconds confirms these findings. In general, as already mentioned, the feed rates are too high compared to the set-point and the big deviations occur mainly after a step change resulting in bad results for short step duration.

Finally, a frequency analysis for the raw catch scale signal was performed. Again, the analysis is done for the first four steps only, because they inhibit more data points, compared to the other steps and the PRBS part. The measurement rate of the scale was 1 Hz, accordingly, the FFT is calculated to half the frequency range. The typical settling time of the AW224 scale is 2.5 seconds. Thus, the eigenfrequency should be around 0.2 Hz. In this case it is not possible to draw any conclusion though, because the measurement frequency is not sufficient. Only for the highest feed rate of 0.25 kg/h two peaks are visible at 0.41 and 0.57 Hz. It is assumed, that one of them represents the rotation speed of the feeding screw. As the rotational speed of the screw for smaller feed rates is lower, though, and should shift to the left side of the spectrum, it is surprising, that they are not visible in the spectra. As it is not possible to draw conclusions from this data, it is recommended to characterize the frequency behavior of the API feeder with a catch scale with higher sampling and eigenfrequencies in future research.

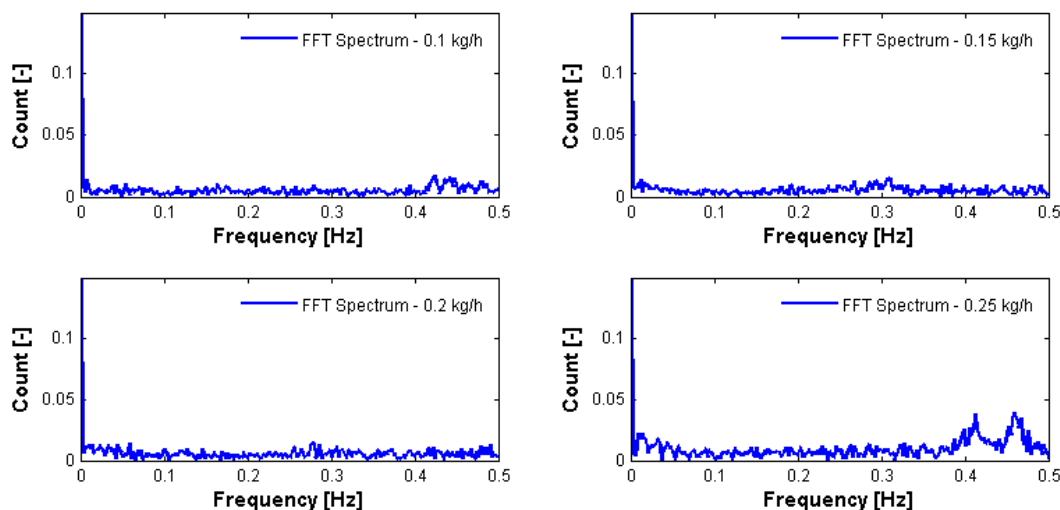


Figure 51: Frequency analysis of the API feeding signal for steps one (0.1 kg/h) to four (0.25 kg/h)

## 4.2 Extrusion Step-Change Experiment

The experimental design described in Section 3.3.2 (Figure 43) was applied. Therefore, the extrusion started with an API concentration of 20%, then the concentration pyramid was executed. Tracer was added in the feed intake barrel twice for each concentration level. When the API concentration was changed, tracer color was added for the first time. Then, a 15-minute video of the extrudate strand was taken. After finishing the video, a sample was taken for microscopy analysis. 20 minutes after the step change, color tracer was added a second time to repeat the RTD measurement in steady state. The color brightness of the outlet strand is analyzed and an RTD calculated. Subsequently, the tracer data for each experiment is fit with the axial dispersion model for an impulse input using the non-linear fitting tool in MATLAB (“nlinfit”).

Figure 52 shows results from the color tracer experiments directly at the steps between different API concentration levels (non-steady state). Figure 53 displays the RTD curves of the color tracer for the steady state at different API concentration levels. In Figure 54, data and an RTD model fit are averaged for each level (e.g., from 30 to 40% and from 40 to 30%) and plotted together for all step changes. Figure 55 gives the same results for the concentration levels.

Analysis of the graphs indicates that higher API content widens the RTD. Surprisingly, this changes for the curve at 50% and steady state because it is narrower than all the others. This could be caused by a change in the rheological behavior above a certain ratio of crystalline particles in the melt. Dispersions can change their rheological character from shear thinning at low concentrations to shear thickening at high concentrations. It may cause enhanced material transport along the wall (wall-slip), as the stickiness of the melt is reduced.

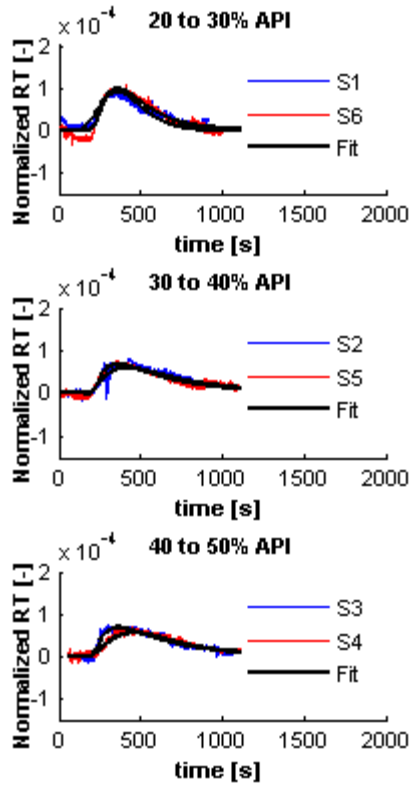


Figure 52: Fit and detected RTD curves during different step changes

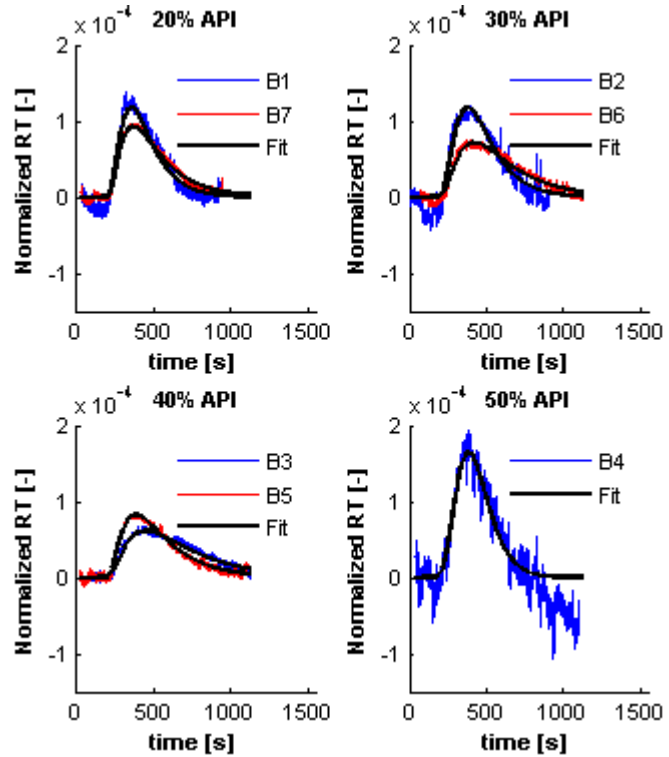


Figure 53: Fit and detected RTD curves for different API concentrations

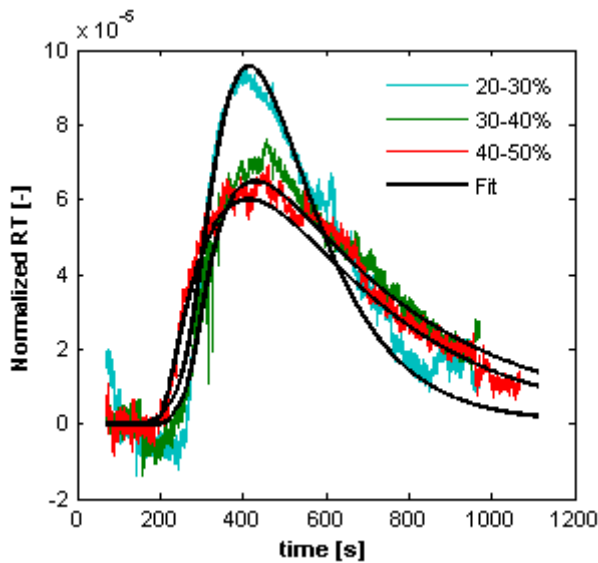


Figure 54: Comparison of RTD curves during different step changes

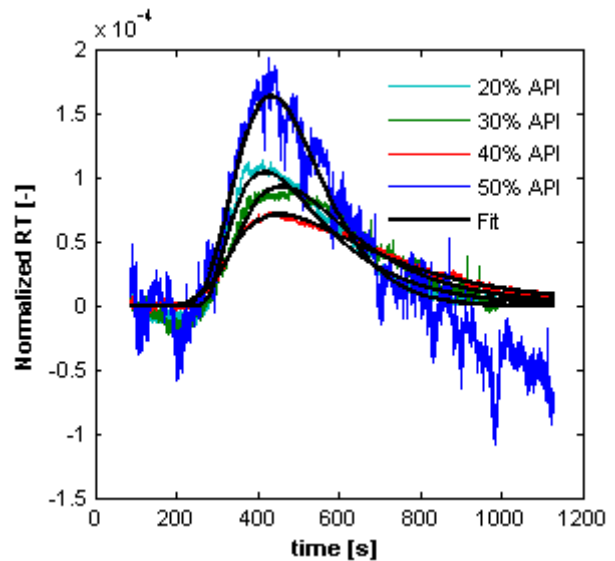


Figure 55: Comparison of RTD curves for different API concentrations

**Table 5 Results from fitting the color tracer data with the axial dispersion experiments**

#	Steady-state						
	1	2	3	4	5	6	7
API content [%]	20	30	40	50	40	30	20
MRT [min]	6.31	7.29	8.28	6.32	7.74	7.49	7.04
DT [min]	3.25	3.72	2.28	3.06	3.49	2.43	3.28
Pe number	7.71	8.43	4.74	20.95	4.69	5.54	4.95

#	During step changes					
	1	2	3	4	5	6
API content [%]	20/30	30/40	40/50	50/40	40/30	30/20
MRT [min]	6.32	8.85	7.47	8.54	8.77	7.12
DT [min]	3.28	2.75	2.35	2.56	3.52	3.39
Pe number	19.36	3.22	2.56	6.26	2.17	5.69

The results from the model-fitting procedure are given in Table 5. The MRT, the dead time (DT) and the  $Pe$  number are estimated. The MRTs obtained from the measured RTDs lie roughly between 6 and 9 minutes. A rough estimation of the MRT can also be done, with the following equation:

$$\bar{t} = \frac{V_{free} \cdot f}{\dot{V}}$$

**Equation 33** Estimation of the mean residence time using the free volume in the extruder, the filling grade and the volume flow.

with  $V_{free}$  being the free volume in the extruder (135 ml),  $f$  the filling grade (estimated with 0.4) and  $\dot{V}$  the volume flow through the extruder. The material density for differing API content is approximated by calculating the mixture density from the two components' densities in solid state. This results in an approximated MRT of 7 to 8 minutes. Regarding that the approximation takes into account neither the difference between melt and solid density, nor any rheological parameters, this shows rather good accordance with the experimental data. As indicated in Figure 55, the MRT increases from 20 to 40% API content and decreases from 40 to 50%. The dead time varies between 2 to 4 minutes. In this case no clear trend can be identified. The  $Pe$  number varies between 4 and 21 for the steady-state data and between 2 and

20 during the step changes. According to the physical meaning of the  $Pe$  number, the convection has stronger influence on the material compared to distributive mechanisms in all cases. Still, the range of variation is surprisingly big. Basically, most of the model fits have a  $Pe$  number below 8.5 and only the step level with the highest API content ( $Pe = 20.95$ ) and the step change from 20 to 30% of API in the melt ( $Pe = 19.36$ ) exceeds these values by more than a factor of two. The influence of the  $Pe$  number on the form of the curve is illustrated in Figure 56.

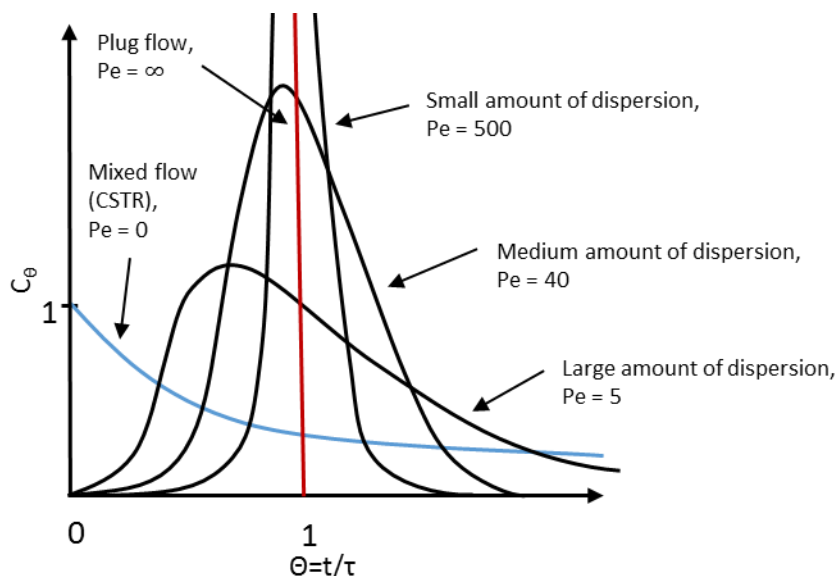


**Figure 56: Influence of the Peclet number ( $Pe$ ) on the shape of the model curve ( $\theta$  = dimensionless time,  $\tau$  = mean residence time,  $t$  = time,  $C_\theta$  = tracer concentration)**

The mixing effect decreases for big  $Pe$  numbers. There is only one measurement of the RTD at an API content of 50% and this might be an extreme result (outlier). The RTD from the first step change (20 to 30%) could also be an extreme value, especially when taking into account the last step change between the same concentration levels with a value of 5.69.

Uncertainties in the results are caused by the fact that due to feeder fluctuations, not only the fraction of crystalline particles in the melt varies, but also the melt density and, accordingly, the total throughput. As the throughput has significant influence on the residence time, as stated by Gao et al. [32], this must be considered in analyzing the data. Moreover, the light source during the experiment was simply the room light, so it could have happened, that a “less bright” coloring of the strand was caused by shadows from people moving in the surroundings. In addition, the strand sometimes got caught on the black background because of its stickiness and was removed with a wooden spatula. During the experiment special care was taken to not move directly through the area used for analysis afterwards, but this might have influenced the picture. Another factor of uncertainty is that the amount of tracer added to the extruder was not measured, but just estimated visually. Using bigger amounts of tracer might cause that instead of reaching a single peak, the color intensity reaches a certain maximum optical intensity level and the curve seems to have a platform instead of a peak.

Analyzing the MRT from the color tracer experiments, the averaged filling grade can be calculated using Equation 33 and a throughput  $\dot{V}$  of 0.5 kg/h. To get an overview over the extrusion run, Figure 57 illustrates

the filling grade together with other process parameters. The set-point and the current API concentration as well as the concentration estimated via NIR are shown in the plot. Moreover, the read-outs from torque and pressure are shown, both smoothed over a span of 31 seconds. The current API concentration is evaluated by combining the feed rates displayed by the two feeders.

$$c_{API} = \frac{\dot{m}_{API}}{\dot{m}_{Matrix} + \dot{m}_{API}}$$

Equation 34 Calculation of API inlet concentrations from feed rates displayed by the feeders

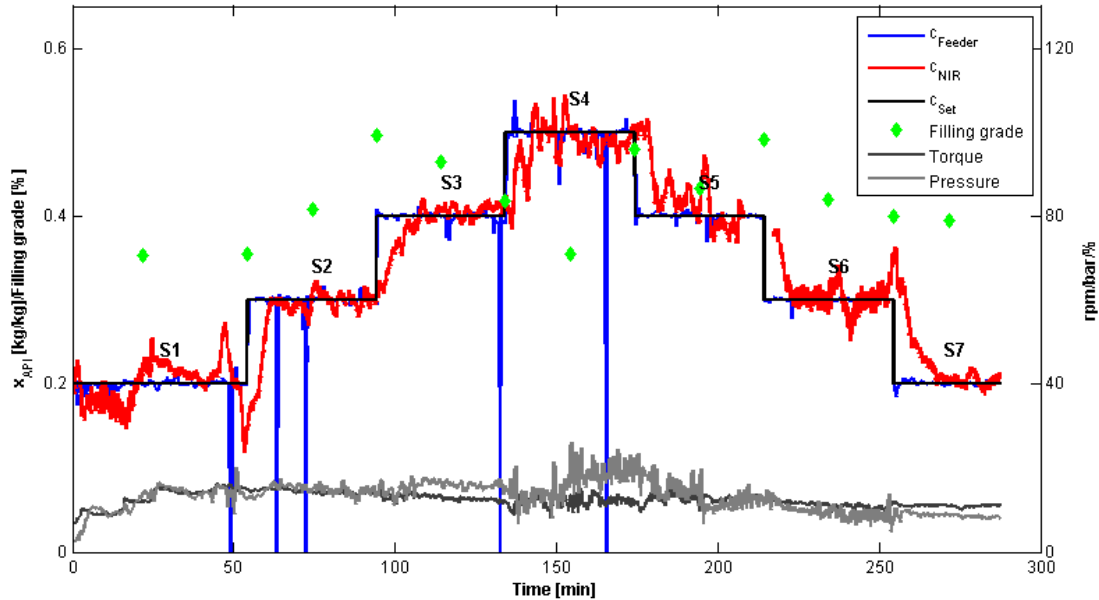
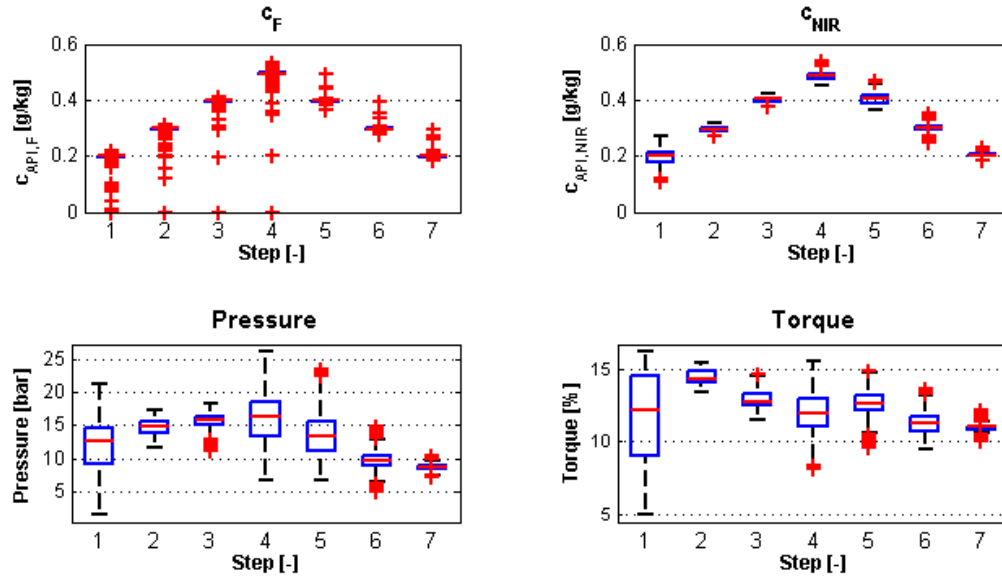


Figure 57: Overview of the extrusion run with color tracer experiments

Several problems with the API feeding system occurred during the experiment due to bad flow behavior of the API paracetamol. If the deviations captured by feeder exceeded a certain limit, it suddenly shut down. These feeding failures can be seen where the feeding API concentration (blue line) jumps to zero. Except for these deactivations, feeding was stable and the feeder display indicated better accuracy than during the feeding experiments. This might be the case, because the feed rate levels were kept constant for a longer time. The stability of the process parameters is analyzed using box plots for each concentration level (Figure 58). The boxes for the API concentration at the inlet are in a very narrow range, indicating deviations from the set-point being small. Thus, it can be assumed that, in this case, the influence of external disturbances on the feeding system was little. For those concentration levels in which feeding problems occurred, there are several outliers under the boxes. Still the IQR is in the same range for the concentration levels across the extrusion run, so the greater majority of data points indicates very good feeding stability. In order to evaluate the accuracy of the API concentration estimated by NIR, the data set analyzed in the boxplot excludes the time during the step change (600 seconds approximated for all levels). Otherwise the median would be distorted to lower, or higher values due to the process time delay. Thus, the median values are in good accordance to the set concentration levels and the feeder data. Looking at the feeder deactivations, it is possible to see, that those are dampened out in the NIR signal, as they do not reach the zero level. . Looking at the variability of the concentration in the IQR though, a more fluctuating concentration is indicated.



**Figure 58: Boxplots for the API concentration calculated from the feeder's displayed feed rates, the API concentration estimated by NIR spectroscopy, the pressure and the torque during the experiments**

The development of pressure and torque were also analyzed statistically to investigate connections with the API concentration. It can be seen that the pressure rises with higher API content, which can be explained with a change in rheological attributes of the melt. The API paracetamol does not melt at the processing temperatures, so there is a higher ratio of crystalline material in the extrudate. The values are not identical for steps with the same API concentration, though. This could be due to a drift in the sensor signal, or an indicator, that the process is not at a steady state. The torque cannot be related to the API concentration from this boxplot.

Evaluation of mixing performance is done with the calculation of the VRR, consisting of the variance in the input divided by the variance of the output. The VRR is calculated for the data between each step and is given in Table 6.

$$VRR = \frac{\sigma_{input}^2}{\sigma_{output}^2}$$

**Equation 35** Variance reduction ratio of mixers [16]

**Table 6** VRR calculated for the steps in the color tracer experiment

Step #	1	2	3	4	5	6	7
<b>VRR</b>	0.0008	0.0123	0.0154	0.0195	0.0001	0.0003	0.0001

First, the VRR is usually calculated from data received with the same measurement method. In this case the inlet concentration is derived from the feed rates indicated at the feeders display. The outlet concentration is derived from the NIR spectra recorded at the extruder's outlet. Accordingly, the measurement methods differ very strongly in sampling method and also the material properties change drastically during the process (solid state at the inlet and liquid-solid dispersion at the outlet). Moreover, the feeder displays a smoothed signal and does not necessarily give the real feed rate, as found in the feeding experiments. Thus, it must be taken into account that, especially after a step change, the real feed rate does not reach the new set-point as fast as is indicated by the feeders.

Second, the NIR probe at the extruder outlet detects spectra from a very limited sample volume of  $4.9 \text{ mm}^3$  only. This sampling volume is investigated every second. With a mass flow rate of  $0.5 \text{ kg/h}$  and an average density of  $1150 \text{ kg/m}^3$ , the sampling volume for the gravimetric control is  $121 \text{ mm}^3/\text{s}$ . Thus, the NIR spectrometer samples less than 5% of the material sampled at the inlet by the gravimetric control of the feeder. Accordingly, the input signal is averaged stronger than the outlet signal. In addition, paracetamol, which is detected by the NIR probe, is embedded in CaSt, forming a solid dispersion with changing optical properties. Besides the variation of paracetamol crystals present in the sampling volume, the penetration depth varies with higher paracetamol content. Thus, the variance of the NIR signal is not caused by a single API crystal passing the probe as it is averaged over a great number of crystals.

In order to get an impression of the API crystal size in the extrudate, incident light microscopy was performed. During extrusion the crystals break down to smaller sizes, as can be seen from Figure 59 and Figure 60. The crystal size after extrusion could be estimated at around  $10$  to  $20 \text{ }\mu\text{m}$ . This is significantly smaller than the NIR probe face and the sampling volume, so the effect of seeing single particles moving past the probe can be eliminated.



Figure 59: Paracetamol crystals, raw material (50 x)

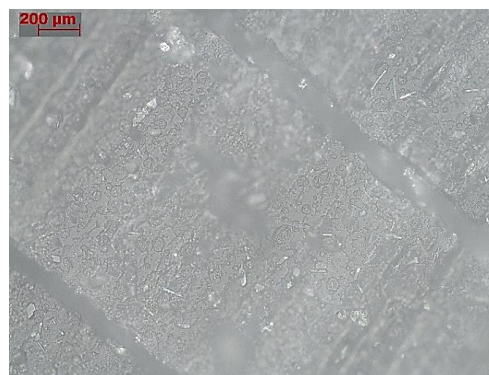


Figure 60: Extrudate with 20% paracetamol (50 x)

Another reason for the instable NIR measurements is the fact that the API concentration also influences the material flow rate in front of the die, as the volume flow and velocity profile changes with melt density at constant mass flow rates. Paracetamol has a higher density than CaSt and, accordingly, the volume flow decreases with increased API content. Therefore, the negative effect of higher API concentration on the sampling volume is increased even further, since in addition to the penetration length, the material exchange in front of the probe is also reduced.

The axial dispersion model is fit to the step changes in the experiment and the resulting model parameters subsequently compared to the color tracer experiments. Figure 61 illustrates the results from the fitting

procedure. In a first step, the “nlinfit” algorithm estimates the  $Pe$  number, the dead time, the mean residence time and the steady state gain from the data. As the algorithm does not converge for the steps two to six, fitting for these steps is done with fixed  $Pe$  numbers taken from the corresponding color-tracer RTD fits. The fitting results are summarized in Table 7.

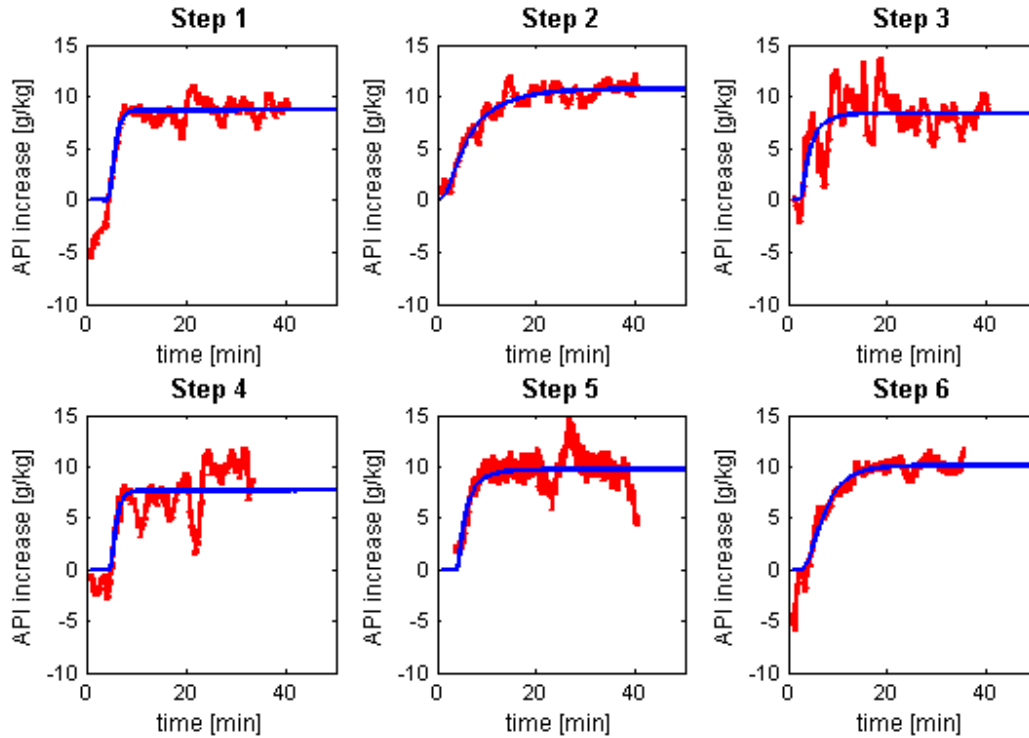


Figure 61: The axial dispersion model fits (blue) to concentration step changes from the experiment (red)

Table 7 Results from the fitting procedure of the step-change data with the axial dispersion model

#	1	2	3	4	5	6
API content [%]	20/30	30/40	40/50	50/40	40/30	30/20
$Pe$ [-]	14.90	3.22	2.56	6.26	2.17	5.69
MRT [min]	4.99	9.28	3.91	5.22	5.37	7.02
DT [min]	2.26	-1.51	1.19	3.41	2.85	0.42
Steady state gain [ $g_{API}/kg$ ]	8.67	10.75	8.41	7.70	9.72	10.12

The  $Pe$  number for the first step change is obtained by fitting. The value (14.9) is very similar to the value from the color tracer experiments (19.36). The MRT values for the API step changes lie between 3.9 and 9.3 minutes. Compared to the MRT values from the color tracer experiments (6 to 9 minutes), this is

approximately the same. There is no clear correlation to the API concentration detectable, as it was in the previous results.

In the concentration curve (Figure 57) it can be seen that feeding problems occurred during steps one, three and five. This also might explain the steady state gain values, which are below ten in four out of six cases. The steady state gain indicates at which level the system reaches the new steady state. More problems occurred when the NIR spectra were not recorded at the beginning of step five due to communication problems with the database. The dead times for the API concentration step changes lie between -1.5 and 3.5 minutes. Again, this is shorter than the results from the color tracer fit (2.3 to 3.5), but in a similar range. The negative value for the dead time for step two represents a problem that is typical for fitting noisy step change data. Random fluctuations in the signal are sometimes detected as an increase caused already by the input. The convergence problems in the step-fitting procedure are common as well, as there are too many fitting solutions and it is hard to find a local minimum for the solution.

As pointed out in the evaluation of feeding experiments, the API feeder shows a high variance which is also seen in the NIR concentration measurements. Thus, the evaluation experiments show partly inconclusive results. However, the developed methodologies can be easily applied to further investigations. Specific attention should be paid to the feeding strategies and their evaluation.

### 4.3 System Identification Experiment

This second extrusion run is performed in order to get data for system identification. This is an alternative way for characterizing the mixing behavior of the extruder compared to the traditional approach in the chemical industry using RTDs. Therefore, transfer function models are generated and afterwards used for simulating the process output. The best transfer function model is then compared to the RTD model from the color tracer experiment in the final section “Comparison and Discussion”.

For the system identification experiments, a special experimental design was chosen. Therefore, the experimental design from the color tracer experiments was adapted. The duration of constant step levels was shortened, to save time and material, but a PRBS sequence was added in order to get additional information about the dynamic behavior. Again, the API concentration indicated by the two feeders, the API concentration estimated via NIR, the set-point for the concentration, torque and pressure are visualized in Figure 62.

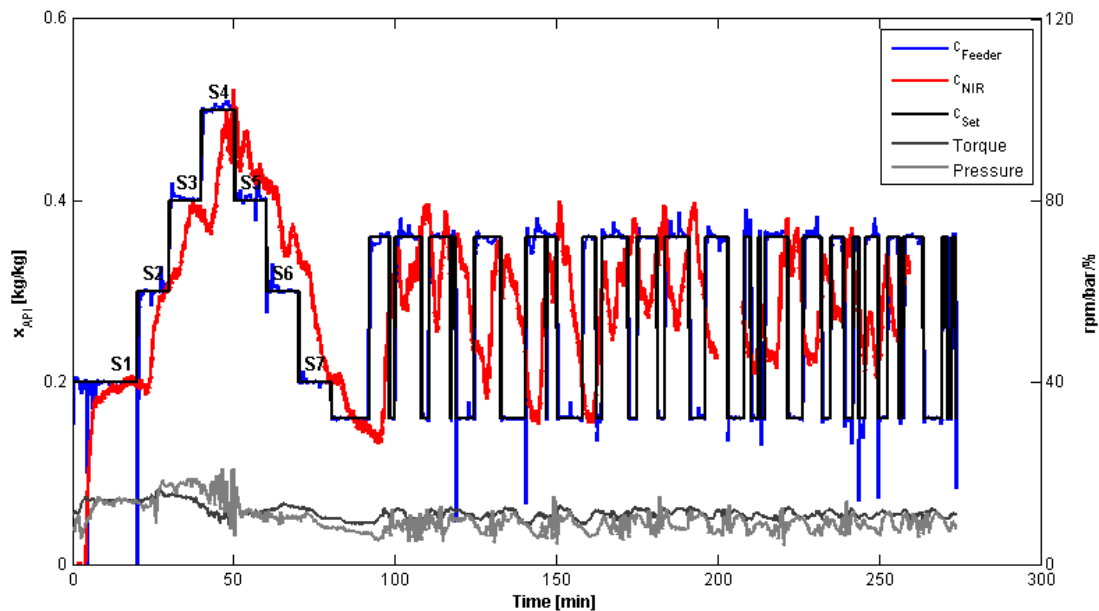


Figure 62: Overview of the system identification experiment

From this overview it can be seen, that the NIR signal shows greater deviations from the set-point compared to the previous color tracer experiments. Especially in the PRBS part, big deviations from the set-point are visible. Obviously, the time needed for the feeders to adapt to the new set-point combined with the mixing effect of the extruder evens out short step sequences. Thus, the system seldom reaches a steady state. This is an indicator that the time steps, especially for the PRBS part, were selected too short. Furthermore, analysis of the feeding experiments already showed that the feeders have great difficulties controlling the feed rate in such a dynamic manner. Therefore, it is not possible to use this data set for system identification. Instead, the data set from the color tracer experiment is used for identification. The system identification data set is used for comparison of the modeling approaches. For future experiments, it is important to use longer time constants in the experimental design. Short-term fluctuation like a feeder shut-down can still be modeled sufficiently, even if the shortest time unit is longer than a typical shut-down. The longest timeframe should be selected sufficiently long, to guarantee reaching the steady state at least a few times

during the extrusion run. This contains the dead time plus the maximal residence time in the system. For this extrusion set-up, this would be approximately 15 minutes. Thus, the color tracer experiment with constant concentration levels held over 40 minutes is expected to be good for identifying low frequency dynamics. High-frequency dynamics, though, might not be modeled sufficiently.

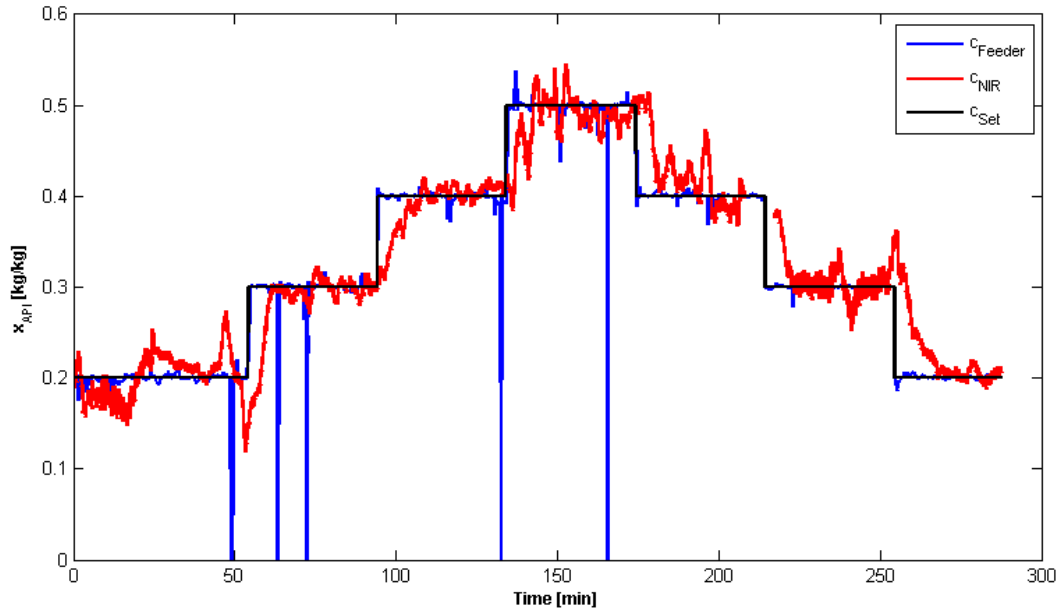
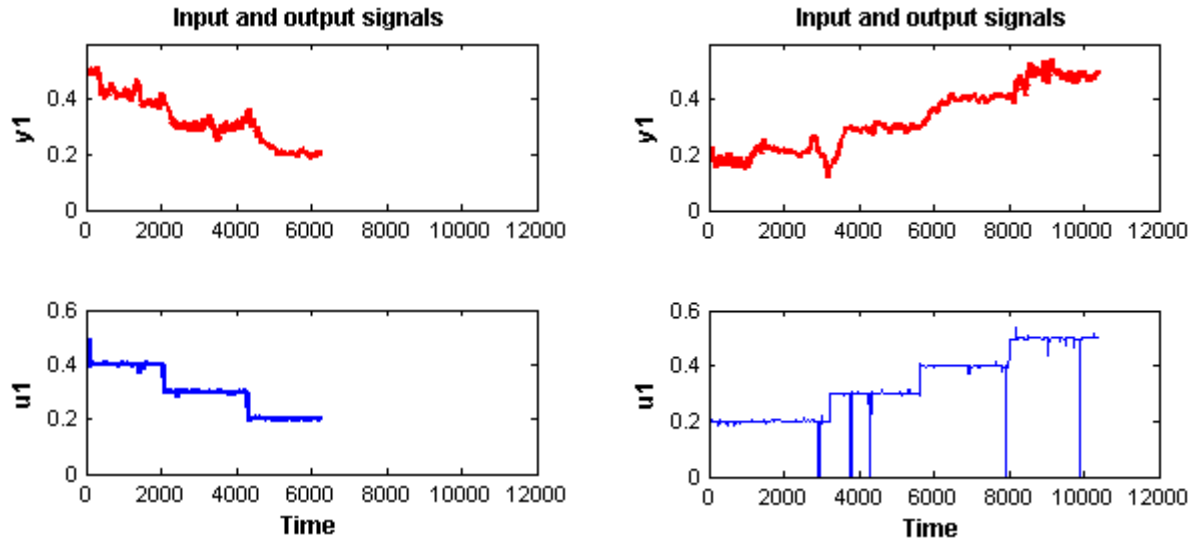


Figure 63: Color tracer experiment used for system identification

The data set from the color tracer experiment is shown in Figure 63. For system identification the color tracer data set is divided into two parts, as can be seen in Figure 64. The input is the API concentration as indicated by the feeders' displays and the output is the concentration estimated via NIR. The division is done at the end of the step with the highest API content. During the step-downs, a communication error between the NIR software and SIPAT occurred and caused missing values. Because of MATLAB's inability of to handle empty entries in the data set for system identification, the missing data was cut out at that point. The shorter data set, containing the step-downs from the pyramid was selected as the validation data set, because the feeding was more stable during that phase. Due to the numerous shut-downs during the step-ups in the concentration pyramid, they are not suitable as the identification set. Thus, it is used for validation. The system identification procedure consists of the following steps:

- Generation of data,
- model selection,
- model order selection,
- model parameter estimation,
- model validation,
- comparison of models and selection of the best model.



**Figure 64:** Identification (left) and validation (right) data sets for system identification with the input  $u_1$  being the API concentration as indicated by the feeders and the output  $y_1$  the concentration estimated via NIR at the extruder outlet

The two models (ARMAX and Box-Jenkins) introduced in the theory part are applied to the modeling data set. The first step in model order estimation is the selection of the process time delay. This was estimated by performing a cross-correlation analysis (“xcorr” command) between the input and the output API concentration. Figure 65 illustrates the cross-correlation analysis, resulting in an estimated process time delay of 239 samples. With one sample per second this equals to a dead time of 4 minutes and is a little bit longer compared with the color tracer experiment dead time, which is approximately 3 minutes on average. This could indicate that clogging occurs in front of the NIR probe.

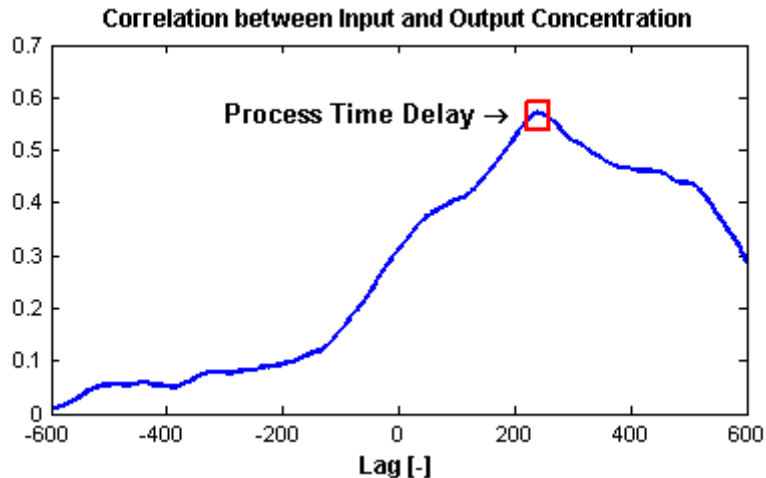


**Figure 65:** Process time delay estimation by performing correlation analysis

The model order selection was performed using a self-written MATLAB script varying the orders for each polynomial from zero to five and evaluating the AIC and “goodness of fit” for each model order. The best model orders for both models are saved. The maximal possible model order was selected to be five, because a higher order is very likely to overfit the data. The model order of a system consisting of coupled sub-processes equals the product of the order of the sub-systems. The AIC evaluates the best fit for the lowest

possible model order as described in the “System Identification” chapter. The “goodness of fit” command in MATLAB simply identifies the data with the best accordance to the data.

### ARMAX Model

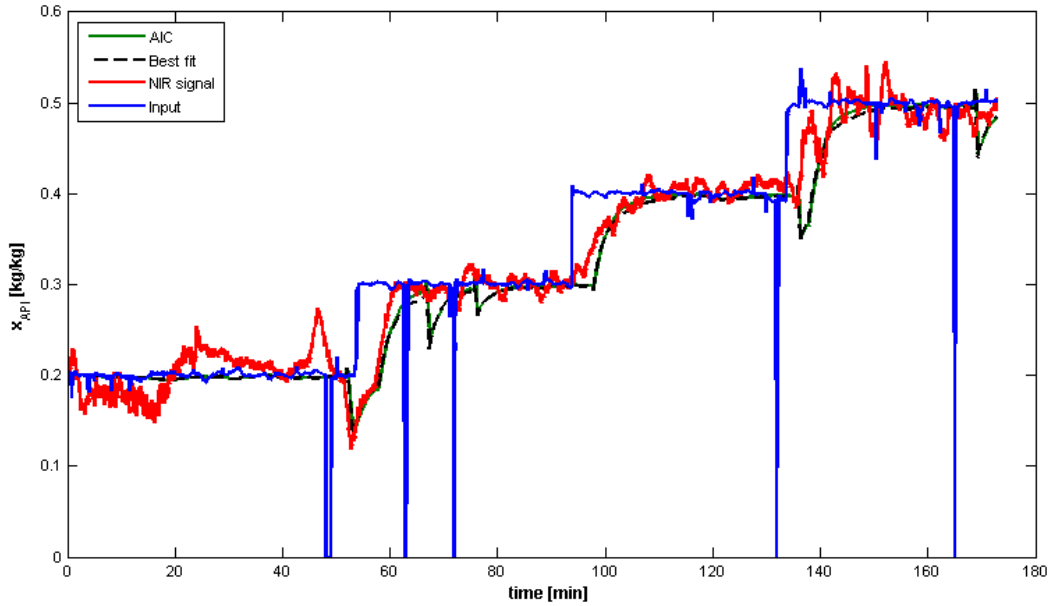


**Figure 66: The ARMAX model with the model order selected using the AIC and the “best-fit” criterion used for simulating the output of the validation data set**

Figure 66 displays the simulated API concentration using the dynamic model in reference to the measured API concentration from the experiment. The model order selection with the AIC resulted in  $n_A = 3$ ,  $n_B = 5$  and  $n_C = 5$ . The fit to the estimation data is evaluated with 97.1%. The “best-fit” criterion provided the orders:  $n_A = 3$ ,  $n_B = 4$  and  $n_C = 2$  and a fit value of 97.17%. As the AIC tests the model according to the aspect of keeping the model as simple as possible and results in approximately the same model, this model structure is selected for the ARMAX model.

Thus, estimation of the polynomials for the ARMAX model (Equation 16) results in:

$$\begin{aligned}\hat{A}(z^{-1}) &= 1 - 1.988 z^{-1} + 1.332 z^{-2} - 0.3415 z^{-3} \\ \hat{B}(z^{-1}) &= -0.03851 + 0.08524 z^{-1} - 0.03858 z^{-2} - 0.0405 z^{-3} + 0.03457 z^{-4} \\ \hat{C}(z^{-1}) &= 1 - 1.052 z^{-1} + 0.3134 z^{-2} + 0.04022 z^{-3} - 0.0206 z^{-4} + 0.04806 z^{-5}\end{aligned}$$

**Equation 36 Estimated polynomials for the ARMAX model**

The polynomials are combined into a dynamic model  $\hat{G}(z^{-1})$  and a disturbance model  $\hat{H}(z^{-1})$ .

$$\hat{G}(z^{-1}) = \frac{-0.03851 + 0.08524 z^{-1} - 0.03858 z^{-2} - 0.0405 z^{-3} + 0.03457 z^{-4}}{1 - 1.988 z^{-1} + 1.332 z^{-2} - 0.3415 z^{-3}}$$

$$\hat{H}(z^{-1}) = \frac{1 - 1.052 z^{-1} + 0.3134 z^{-2} + 0.04022 z^{-3} - 0.0206 z^{-4} + 0.04806 z^{-5}}{1 - 1.988 z^{-1} + 1.332 z^{-2} - 0.3415 z^{-3}}$$

**Equation 37** ARMAX dynamic and disturbance models with estimated polynomials

$$\hat{y}_k = \hat{H}(z^{-1}) \cdot u_{k-239} + \hat{G}(z^{-1}) \cdot w_k$$

**Equation 38** Estimated ARMAX model

Together with the process time delay  $\delta = 239$  seconds, estimated in the correlation analysis, this results in Equation 38. Figure 67 gives the simulated output for the dynamic and the disturbance ARMAX model.

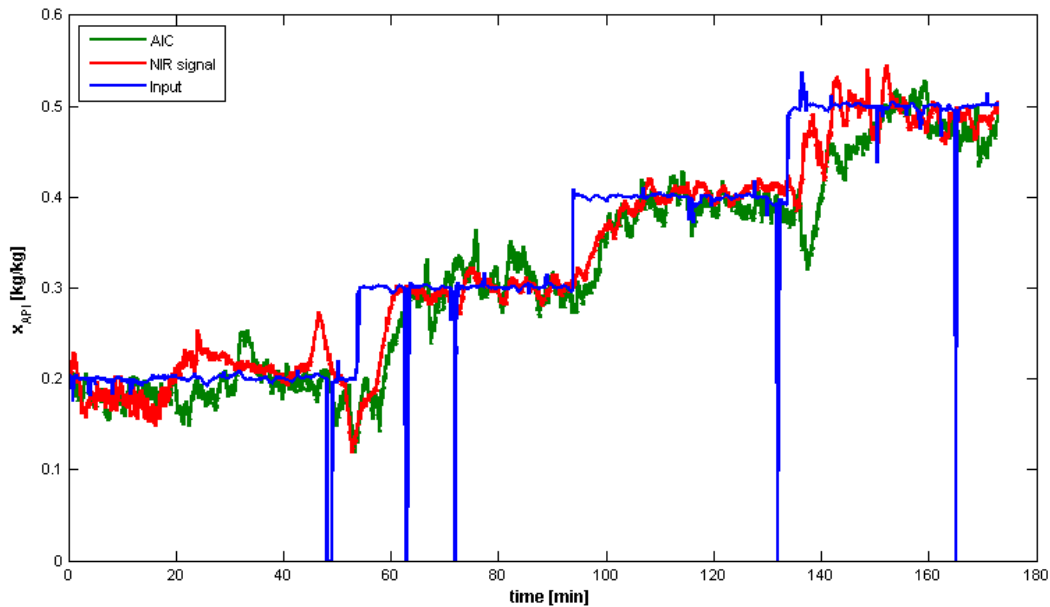


**Figure 67:** Simulated output for the dynamic and the disturbance ARMAX models

### **Box-Jenkins Model**

Estimation of model orders delivered the two Box-Jenkins models given in Figure 68. According to the AIC, the polynomial orders should be chosen as  $n_A = 4$ ,  $n_B = 4$ ,  $n_C = 4$ , and  $n_D = 4$ . The model estimated with these orders gives an accordance of 97.18% with the estimation data. The “best-fit” criterion suggests the orders  $n_A = 3$ ,  $n_B = 1$ ,  $n_C = 5$ , and  $n_D = 3$  with a fit to estimation data accordance of 97.19%. The illustration shows again, that both models are very similar, but in this case the model order estimated with the AIC seems to reflect the data better. Accordingly, this model structure is selected for the Box-Jenkins model.

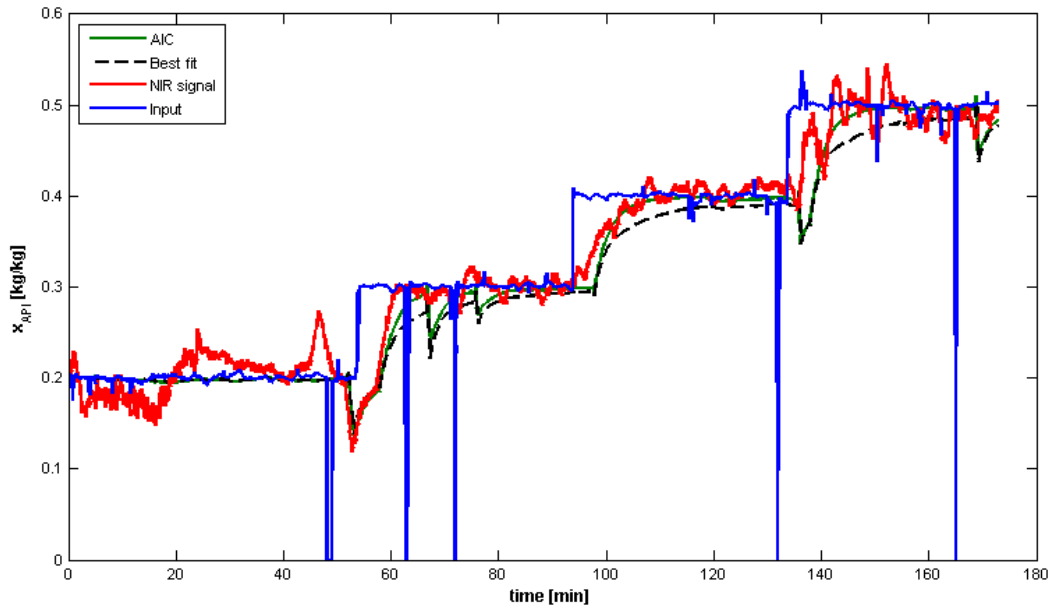


**Figure 68:** The Box-Jenkins model with the model order selected using the AIC and the “best-fit” criterion used for simulating the output of the validation data set

The polynomial orders  $n_A$ ,  $n_B$ ,  $n_C$ , and  $n_D$  for the Box-Jenkins model and the polynomial parameters  $a_1$  to  $a_{n_A}$ ,  $b_0$  to  $b_{n_B}$ ,  $c_1$  to  $c_C$  and  $d_1$  to  $d_{n_D}$  are combined into the following polynomials.

$$\begin{aligned}\hat{A}(z^{-1}) &= 1 - 0.6813 z^{-1} + 0.07923 z^{-2} + 0.3039 z^{-3} - 0.6876 z^{-4} \\ \hat{B}(z^{-1}) &= -0.03062 + 0.03243 z^{-1} + 0.0259 z^{-2} - 0.01351 z^{-3} \\ \hat{C}(z^{-1}) &= 1 - 3.444 z^{-1} + 4.399 z^{-2} - 2.449 z^{-3} + 0.4945 z^{-4} \\ \hat{D}(z^{-1}) &= 1 - 2.522 z^{-1} + 2.037 z^{-2} - 0.4236 z^{-3} + -0.08002 z^{-4}\end{aligned}$$

**Equation 39** Estimated polynomials for the Box-Jenkins model

Again, the estimated polynomials are combined into a dynamic model  $\hat{G}(z^{-1})$  and a disturbance model  $\hat{H}(z^{-1})$ .

$$\begin{aligned}\hat{H}(z^{-1}) &= \frac{-0.03062 + 0.03243 z^{-1} + 0.0259 z^{-2} - 0.01351 z^{-3}}{1 - 0.6813 z^{-1} + 0.07923 z^{-2} + 0.3039 z^{-3} - 0.6876 z^{-4}} \\ \hat{G}(z^{-1}) &= \frac{1 - 2.522 z^{-1} + 2.037 z^{-2} - 0.4236 z^{-3} + -0.08002 z^{-4}}{1 - 3.444 z^{-1} + 4.399 z^{-2} - 2.449 z^{-3} + 0.4945 z^{-4}}\end{aligned}$$

**Equation 40** Box-Jenkins dynamic and disturbance models with estimated polynomials

Finally, the estimated Box-Jenkins model is given in Equation 41 containing the estimated dynamic and disturbance models and the delay sample time  $\delta$ .

$$\hat{y}_k = \hat{H}(z^{-1}) \cdot u_{k-239} + \hat{G}(z^{-1})w_k$$

**Equation 41**      **Estimated Box-Jenkins model**

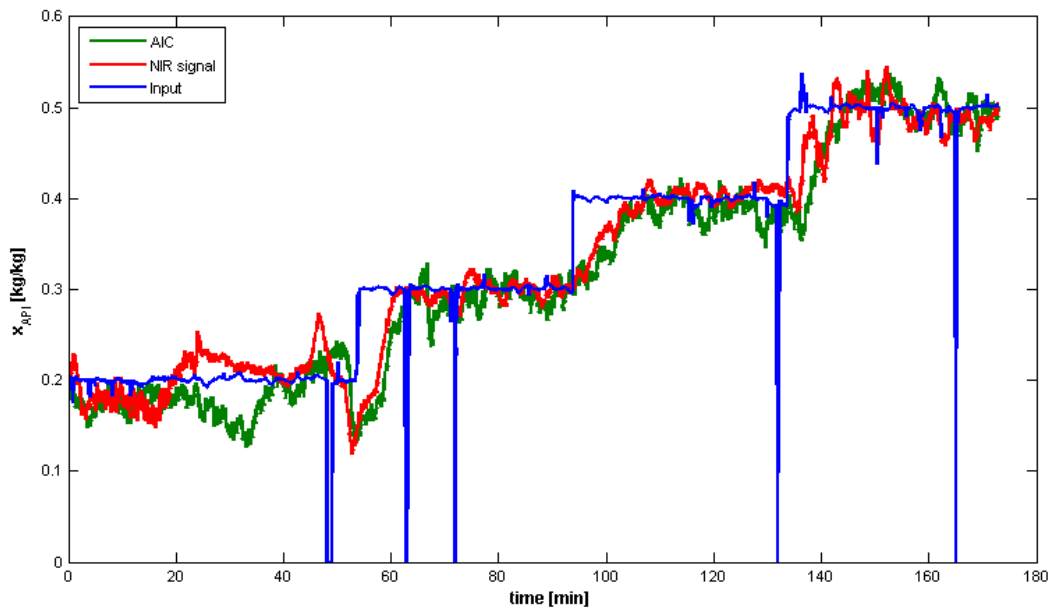


**Figure 69: Simulated output for the dynamic and the disturbance Box-Jenkins models**

Figure 69 illustrates the result for a simulation of the validation data set. Comparing it to the curves from the ARMAX model (Figure 67) and the Box-Jenkins model, the advantage of a disturbance model independent from the dynamic model can be seen. This allows to reach better accordance of the fit to the data, because no trade-off must be made. Thus, the Box-Jenkins model will be used in the comparison to the RTD model.

## 4.4 Comparison and Discussion

The color tracer experiment resulted in RTDs derived for different API concentration levels. In order to allow a comparison of this RTD data to the transfer function obtained from the system identification procedure, the RTDs are averaged. As there was a drastic change in the RTD curve from 40 to 50% API content, averaging is done only over the RTDs from the steps between 20 and 40%. This is necessary, because system identification assumes the process to behave linearly within the data range. This is not the case, as the RTDs (MRT, dead time and width of the curve) changed over the API concentration levels during the color tracer experiments. Still, for comparison purposes this effect is neglected. The comparison of the two approaches to model the dampening behavior of the extruder is performed by simulating an API concentration output by applying both models to an input sequence. As it was not possible to perform system identification using the originally planned experimental design, the data from this experiment is used to compare both methods to experimental data. This way, a conclusion can also be drawn, on how capable the models are to model high-frequency dynamics, even though generated to data containing low-frequency changes only.

Convolution is used for applying the averaged RTD from the color tracer experiments (steps from 20 to 40% API content) to the input sequence. Therefore, the appropriate MATLAB command (“conv”) is used. Application of the transfer function models on the input sequence is conducted with the simulation command (“sim”) in MATLAB. Both output curves are plotted together with the output measured in the experiment and the input sequence, which equals the API concentration at the inlet calculated from the displayed feed rates. Figure 70 illustrates the results from the model comparison.

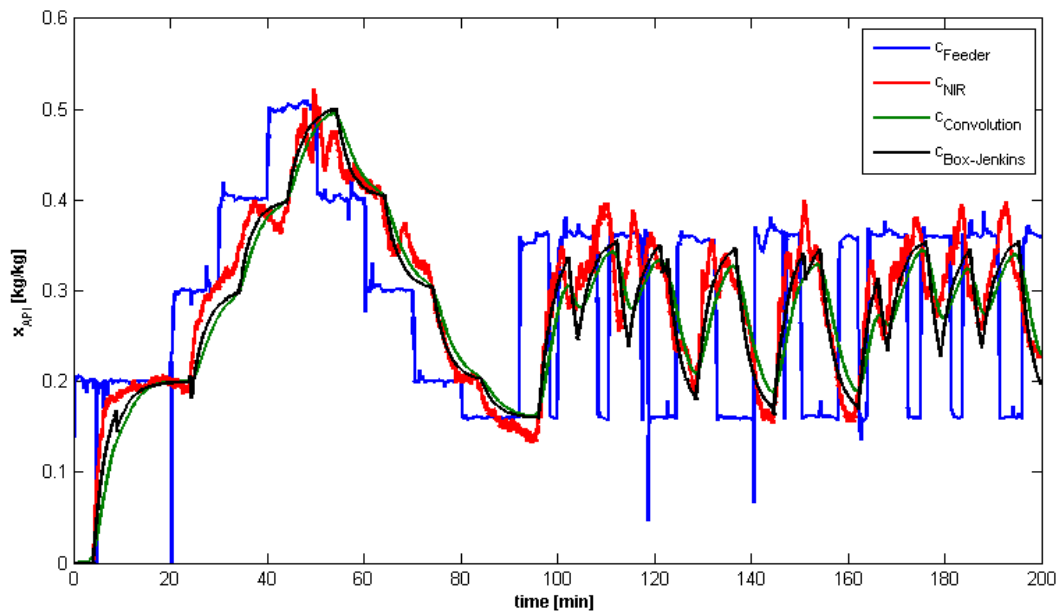


Figure 70: Comparison of modeling approach using the RTD and a Box-Jenkins model without the disturbance model

For the Box-Jenkins model only the dynamic model is calculated. It can be seen that the concentration curves resulting from the convolution with the RTD are a little bit flatter compared to the Box-Jenkins and the experimental data. This means that the RTD curve is broader than the impulse response of the dynamic system represented by the Box-Jenkins model. This could be explained with the fact, that the NIR probe

was installed a little bit upstream of the extruder outlet. Thus, the material passing the probe is “younger” than the material recorded during the color tracer experiment, which might cause a narrower RTD. As there was only a pipe installed downstream of the NIR probe, it can be assumed that the flow regime from this point on, was a laminar pipe flow. Thus, a widening effect on the RTD is not very likely. Anyways, a second approach to explain the difference between the models can be given, looking at the color tracer experiment. It is not known, whether the detectable color intensity of the extrudate reaches a maximal saturation level. In case too much tracer color was added, the peak of the RTD curve might have been flattened, because a maximum intensity level was crossed. In that case, the RTD would appear wider than it is, due to the normalization of the curve, which was performed afterwards. Therefore, in future experiments it is important to determine the amount of color tracer before adding it to the process, so that a normalization can be done with that information.

Looking at the deviations from both models from the data, it is important to keep in mind, that it was found in the color tracer experiments that the API concentration influences the dynamic behavior of the system. These changes in MRT and dead time, for example, at different concentration levels cannot be modeled with this approach.

## 5 Summary and Conclusions

The impact of feed rate fluctuations on the CU of hot melt extruded pharmaceutical products and capabilities to dampen this fluctuation by mixing during extrusion have been investigated. The work comprises the evaluation of feeding performance, mixing behavior and systems identification.

The feeding fluctuations are evaluated in feeding experiments with a catch scale. Therefore, the set feed rate, feed rates indicated at the feeders' displays and data from a catch scale under the feeder outlet are compared. The chosen feeding strategy is a split-feeding approach with pure raw substances. The feeders' accuracies were found to be good regarding the feed rates indicated by the feeders' displays. The relative deviation of the mean value to the set-point is below 2% for the matrix feeder and 5% for the API feeder, when the feed rate was kept constant for a time longer than the feeder's settling time. Data from the catch scale revealed certain deviations from the displayed feed rates, resulting in less accuracy and pronounced high frequency fluctuations. The obtained relative deviation values were up to 5% for the matrix feeder and up to 14% for the API feeder. It was found that the API feeder had a rather long settling time, which influenced the values for the accuracy significantly for short steps. In general, the API feeder showed worse performance compared to the matrix feeder, due to the difficult flow behavior of the cohesive API. Furthermore, the analysis of the catch scale data smoothed over five seconds showed that the dynamic of the catch scale has a significant influence on the results. Catch scale data smoothed over 60 seconds showed better agreement with the feeder data. However, high frequency fluctuations are fully neglected at this time scale. Thus, in order to get insight into high-frequency feeding dynamics, it is necessary to further investigate the feeder performance with dedicated equipment.

The mixing behavior of the extruder was investigated with RTDs. The RTDs are determined in color tracer experiments and NIR step responses. The RTD curves from the color tracer experiments were evaluated using video analysis. This analysis revealed a dependency of the RTD on the API content. From 20 to 40% of API content, the RTD becomes broader indicating more intensive mixing in the extruder. For the highest API concentration at 50%, the RTD was found to be narrower than for all the other concentrations. This could be due to a change in the rheological behavior of the extrudate, when a certain API concentration is exceeded. Paracetamol and CaSt form a two-phase flow in the extruder, with a CaSt melt embedding the API crystals. A higher share of API might cause wall-slip due to reduced stickiness of the extrudate. An axial dispersion model was fit to the color tracer RTD curves and resulted in  $Pe$  numbers between 2.2 to 8.5 (two outliers with 19 and 21). The  $Pe$  number sets the convective transport in relation to the dispersive transport in the system and these values indicate a large amount of dispersion taking place in the extruder.

The NIR measurements enabled the comparison of the input API variance (feed rate read-outs of the feeders) with the output API variance by calculating the VRR. The VRR shows a misleading result. It indicates segregation in the extruder, because the output variance exceeds the input variance. However, this is not the case, of course, and illustrates that it is not possible to calculate the VRR using two different measurement methods and sample volumes.

The system identification experimental data was found not to be suitable for the identification procedure due to process instabilities. Thus, the system identification was done using the data from the color tracer experiment. The system identification procedure delivered two transfer function models, an ARMAX

model and a Box-Jenkins model. Applying the models to a validation data set, the Box-Jenkins model was found to be better suited to picture the dynamic behavior of the process.

The Box-Jenkins and the averaged RTD curves are used simulate the product concentration by applying the to the feeder data from the system identification experiment. In that way, the simulation results could be compared to experimental data from a completely independent experiment. Both models were found to be capable of simulating the output concentration in good accordance to the experimental data and with each other.

The results from this thesis can be used to describe the dampening behavior of an extruder set-up with simple models and key figures. The key figures allow to compare screw designs quantitatively and select an appropriate design for given feeder accuracies. The mixing models can be integrated in the process monitoring system, for example, predicting the product concentration in real time for fluctuating input concentrations. Thus, the results can be applied for process development and control purposes.

## 6 Appendix

### 6.1 List of Tables

Table 1	Theoretical modeling methodologies for continuous blending. [21]	6
Table 2	Selected feed rates	43
Table 3	Statistical evaluation of the K-Tron feeding experiments	49
Table 4	Statistical evaluation of the API feeding experiments	53
Table 5	Results from fitting the color tracer data with the axial dispersion experiments	56
Table 6	VRR calculated for the steps in the color tracer experiment	59
Table 7	Results from the fitting procedure of the step-change data with the axial dispersion model	61

### 6.2 List of Equations

Equation 1	Normalized RTD function	20
Equation 2	Cumulative RTD function	20
Equation 3	Mean value, or first moment of a distribution	21
Equation 4	Mean residence time	21
Equation 5	Volumetric filling grade	21
Equation 6	Variance, or second moment of a distribution	21
Equation 7	Skewness or third moment of a distribution	22
Equation 8	RVD Definition	22
Equation 9	Convolution equation for a linear system	30
Equation 10	Model for discretized input-output data	30
Equation 11	Unilateral $z$ -transform of a sequence $uk$	30
Equation 12	The complex variable $z$ in polar coordinates	31
Equation 13	The frequency-domain system response	31
Equation 14	The transfer function model	31
Equation 15	PLS-R model	32
Equation 16	The ARMAX model	34
Equation 17	Polynomials in the ARMAX model	34
Equation 18	The ARMAX model consisting of a dynamic model $G(z - 1)$ and a disturbance model $H(z - 1)$	34
Equation 19	Estimation of output with the estimated model parameters $\theta$ and the regressor vector $\phi k$	34
Equation 20	Estimated model parameters from the ARMAX model	34
Equation 21	The regressor vector for the ARMAX model	34
Equation 22	The loss function, which is minimized for parameter estimation in MATLAB	35
Equation 23	The Box-Jenkins model	35
Equation 24	Polynomials in the Box-Jenkins model	35
Equation 25	The Box-Jenkins model consisting of a dynamic model $G(z - 1)$ and a disturbance model $H(z - 1)$	35
Equation 26	Estimated parameters from the Box-Jenkins model	35
Equation 27	1D Fokker-Planck equation	35
Equation 28	Solution of the Fokker-Planck equation for the RTD formulated by Taylor [52]	36
Equation 29	Solution of the axial dispersion equation for a pulse input and analysis at the system exit [51]	36

Equation 30	Solution of the axial dispersion equation for a step-change input [53] .....	36
Equation 31	Approximation of NIR sample volume according to Wahl et al. [29] .....	38
Equation 32	Calculation of the relative mean set-point deviation using the mean feed rate and the set feed rate .....	48
Equation 33	Estimation of the mean residence time using the free volume in the extruder, the filling grade and the volume flow. ....	56
Equation 34	Calculation of API inlet concentrations from feed rates displayed by the feeders.....	58
Equation 35	Variance reduction ratio of mixers [16] .....	59
Equation 36	Estimated polynomials for the ARMAX model .....	66
Equation 37	ARMAX dynamic and disturbance models with estimated polynomials.....	67
Equation 38	Estimated ARMAX model .....	67
Equation 39	Estimated polynomials for the Box-Jenkins model.....	68
Equation 40	Box-Jenkins dynamic and disturbance models with estimated polynomials.....	68
Equation 41	Estimated Box-Jenkins model .....	69

### 6.3 Literature

- [1] Food and Drug Administration, *Guidance for Industry: PAT— A Framework for Innovative Pharmaceutical Development, Manufacturing and Quality Assurance*, no. September. United States of America, 2004.
- [2] C. A. Mckelvey, L. Schenck, M. Lowinger, and G. M. Troup, “Applying Extrusion to Pharmaceutical Formulation Design,” *Soc. Plast. Eng. Annu. Tech. Conf.*, 2008.
- [3] M. A. Repka, N. Langley, and J. DiNunzio, *Melt Extrusion - Materials, Technology and Drug Product Design*, 1st ed. New York: American Association of Pharmaceutical Scientists, 2013.
- [4] S. Shah and M. A. Repka, “Melt Extrusion in Drug Delivery: Three Decades of Progress,” in *Melt Extrusion - Materials, Technology and Drug Product Design*, 1st ed., M. A. Repka, N. Langley, and J. DiNunzio, Eds. New York: American Association of Pharmaceutical Scientists, 2013.
- [5] K. Plumb, “Continuous Processing in the Pharmaceutical Industry,” *Chem. Eng. Res. Des.*, vol. 83, no. 6, pp. 730–738, Jun. 2005.
- [6] “Uniformity of Dosage Units (04/2012:20940),” in *European Pharmacopoeia 7.8*, no. 1, 2013, pp. 4101–4103.
- [7] H. Berthiaux, K. Marikh, and C. Gatumel, “Continuous mixing of powder mixtures with pharmaceutical process constraints,” *Chem. Eng. Process. Process Intensif.*, vol. 47, no. 12, pp. 2315–2322, Nov. 2008.
- [8] D. Markl, “Demonstration of a Hot Melt Extrusion Process with SIPAT,” Graz University of Technology, 2012.
- [9] J. Breitenbach, “Melt extrusion: from process to drug delivery technology.,” *Eur. J. Pharm. Biopharm.*, vol. 54, no. 2, pp. 107–17, Sep. 2002.
- [10] Siemens AG, “SIPAT the software heart of PAT - White Paper.”
- [11] F. De Frenne, “User Manual, SIMATIC SIPAT Version 3.1.1. Siemens AG.”

- [12] P. Wahl, D. Markl, D. F. Treffer, D. M. Koller, G. Koscher, E. Roblegg, and J. Khinast, "Full PAT Solution for Real-Time Process Control of a Pharmaceutical Hot Melt Extruder (HME)," in *8th World Meeting on Pharmaceutics, Biopharmaceutics and Pharmaceutical Technology*, 2012.
- [13] K. Kohlgrüber, *Der gleichläufige Doppelschneckenextruder - Grundlagen, Technologie, Anwendungen*. München: Carl Hanser Verlag, 2007, p. 367.
- [14] J. P. Beaudry, "Blender efficiency," *Chem. Eng. J.*, vol. July, pp. 112–113, 1948.
- [15] C. F. Harwood, K. Walanski, E. Luebcke, and C. Swanstrom, "The performance of continuous mixers for dry powders," *Powder Technol.*, vol. 11, no. 3, pp. 289–296, May 1975.
- [16] P. V. Danckwerts, "Continuous Flow Systems - Distribution of Residence Times," *Chem. Eng. Sci.*, vol. 2, no. 1, pp. 1–13, 1953.
- [17] G. R. Ziegler and C. a. Aguilar, "Residence time distribution in a co-rotating, twin-screw continuous mixer by the step change method," *J. Food Eng.*, vol. 59, no. 2–3, pp. 161–167, Sep. 2003.
- [18] A.-Z. M. A. Abouzeid, T. S. Mika, K. V. Sastry, and D. W. Fuerstenau, "The Influence of Operating Variables on the Residence Time Distribution for Material Transport in a Continuous Rotary Drum," *Powder Technol.*, vol. 10, pp. 273–288, 1974.
- [19] R. G. Sherritt, J. Chaouki, A. K. Mehrotra, and L. a. Behie, "Axial dispersion in the three-dimensional mixing of particles in a rotating drum reactor," *Chem. Eng. Sci.*, vol. 58, no. 2, pp. 401–415, Jan. 2003.
- [20] O. S. Sudah, A. . Chester, J. . Kowalski, J. . Beeckman, and F. . Muzzio, "Quantitative characterization of mixing processes in rotary calciners," *Powder Technol.*, vol. 126, no. 2, pp. 166–173, Jul. 2002.
- [21] L. Pernenkil and C. L. Cooney, "A review on the continuous blending of powders," *Chem. Eng. Sci.*, vol. 61, no. 2, pp. 720–742, Jan. 2006.
- [22] J. Curry, A. Kiani, and A. Dreiblatt, "Feed Variance Limitations for Co-Rotating Intermeshing Twin Screw Extruders," in *Continuous Mixer and Extruder Users' Group Meeting*, 1991, no. September, pp. 259–286.
- [23] L. Wang, S. Smith, and C. Chessari, "Continuous-time model predictive control of food extruder," *Control Eng. Pract.*, vol. 16, no. 10, pp. 1173–1183, Oct. 2008.
- [24] T. A. Haley and S. J. Mulvaney, "On-line system identification and control design of an extrusion cooking process : Part I . System identification," *Food Control*, vol. 11, 2000.
- [25] G. M. Troup, C. A. Mckelvey, L. Schenck, M. Lowinger, B. Rudeen, A. Sinha, J. P. Higgins, and W. Point, "Process Analytical Technology for Improved Process Understanding and Control of a Hot Melt Extrusion Process," in *Proceedings of the society of plastics engineers annual technical conference*, 2009.
- [26] A. Kumar, G. M. Ganjyal, D. D. Jones, and M. a. Hanna, "Digital image processing for measurement of residence time distribution in a laboratory extruder," *J. Food Eng.*, vol. 75, no. 2, pp. 237–244, Jul. 2006.

- [27] R. E. Altomare and P. Ghossi, "An analysis of residence time distribution patterns in a twin screw cooking extruder.," *Biotechnol. Prog.*, vol. 2, no. 3, pp. 157–63, Sep. 1986.
- [28] D. Bigg and S. Middleman, "Mixing in a Screw Extruder. A Model for Residence Time Distribution and Strain," *Ind. Eng. Chem. Fundam.*, vol. 13, no. 1, pp. 66–71, 1974.
- [29] P. R. Wahl, D. Treffer, S. Mohr, E. Roblegg, G. Koscher, and J. G. Khinast, "Inline monitoring and a PAT strategy for pharmaceutical hot melt extrusion.," *Int. J. Pharm.*, vol. 455, no. 1–2, pp. 159–68, Oct. 2013.
- [30] Y. Gao, F. J. Muzzio, and M. G. Ierapetritou, "A review of the Residence Time Distribution (RTD) applications in solid unit operations," *Powder Technol.*, vol. 228, pp. 416–423, Sep. 2012.
- [31] L. Schenk, G. M. Troup, M. Lowinger, L. Li, and C. McKelvey, "Chapter 42 - Achieving a HME design space for the production of solid solutions," in *Chemical Engineering in the Pharmaceutical Industry: R&D to Manufacturing*, D. J. am Ende, Ed. John Wiley & Sons, Inc., 2011, pp. 819 – 836.
- [32] J. Gao, G. C. Walsh, D. Bigio, R. M. Briber, and M. D. Wetzel, "Residence-Time Distribution Model for Twin-Screw Extruders," *AiChE J.*, vol. 45, no. 12, pp. 2541–2549, 1999.
- [33] S. Sacher, P. R. Wahl, D. Markl, D. Treffer, J. C. Menezes, G. Koscher, E. Roblegg, and J. G. Khinast, "PAT for Pharmaceutical Extrusion : Monitoring and Supervisory Control," in *AiChE Annual Meeting Proceedings*, 2012, no. October, pp. 1–19.
- [34] G. Vetter, "Dosierverfahren für Prozesskomponenten - Systematik und Dosiergenauigkeit," in *Handbuch Dosieren*, 2. Auflage., G. Vetter, Ed. Essen: Vulkan-Verlag, 2001, pp. 2–38.
- [35] E. K. Kim and J. L. White, "Transient Compositional Effects From Feeders in a Starved Flow Modular CoRotating Twin Screw Extruder," *Polym. Eng. Sci.*, vol. 42, no. 11, pp. 2084–2093, 2002.
- [36] W. E. Engisch and F. J. Muzzio, "Method for characterization of loss-in-weight feeder equipment," *Powder Technol.*, vol. 228, pp. 395–403, Sep. 2012.
- [37] J. G. Khinast, R. Baumgartner, and E. Roblegg, "Nano-extrusion: a One-Step Process for Manufacturing of Solid Nanoparticle Formulations Directly from the Liquid Phase.," *AAPS PharmSciTech*, 2013.
- [38] J. Breitenbach, "Melt extrusion : from process to drug delivery technology," *Eur. J. Pharm. Biopharm.*, vol. 54, pp. 107–117, 2002.
- [39] J. Kirchhoff, "Mixing and Dispersing: Principles," in *Co-Rotating Twin-Screw Extruder - Fundamentals, Technology and Applications*, 1st ed., K. Kohlgrüber, Ed. Munich: Carl Hanser Verlag, 2008.
- [40] E. L. Paul, V. A. Atiemo-obeng, and S. M. Kresta, *Handbook of Industrial Mixing*. Edmonton, Canada: John Wiley & Sons, Inc., 2004.
- [41] C. Martin, "Twin Screw Extrusion for Pharmaceutical Processes," in *Melt Extrusion - Materials, Technology and Drug Product Design*, 1st ed., M. A. Repka, N. Langley, and J. DiNunzio, Eds. New York: American Association of Pharmaceutical Scientists, 2013.

- [42] J. Hepperle, "Polymerschädigung Einführung," in *VDI Wissensforum - Optimierter Betrieb und Scale-up von Doppelschnecken-Extrudern*, 2012.
- [43] D. Treffer, P. Wahl, D. Markl, G. Koscher, E. Roblegg, and J. Khinast, "Hot Melt Extrusion as a Continuous Pharmaceutical Manufacturing Process," in *Melt Extrusion - Materials, Technology and Drug Product Design*, First Edit., M. A. Repka, N. Langley, and J. DiNunzio, Eds. New York: American Association of Pharmaceutical Scientists, 2013.
- [44] A. Gryczke, "Hot-Melt Extrusion Process Design Using Process Analytical Technology," in *Melt Extrusion - Materials, Technology and Drug Product Design*, 1st ed., M. A. Repka, N. Langley, and J. DiNunzio, Eds. New York: American Association of Pharmaceutical Scientists, 2013.
- [45] G. M. Troup and C. Georgakis, "Process systems engineering tools in the pharmaceutical industry," *Comput. Chem. Eng.*, vol. 51, pp. 157–171, Apr. 2013.
- [46] W. Haager, *Regelungstechnik*. Wien: övb & hpt VerlagsgmbH & Co. KG, 2001.
- [47] R. Johansson, *System Modeling & Identification*, 2nd Editio. Lund: Prentice Hall, 2011, p. 534.
- [48] L. Ljung, *System Identification - Theory for the User*, 2nd Editio. Upper Saddle River, NJ: Prentice Hall, Inc., 1999, p. 609.
- [49] D. Berckmans, J.-M. Aerts, V. Exadaktylos, and S. Viazzi, "Biological response measurements for process management." KU Leuven, Leuven.
- [50] W. Kessler and R. W. Kessler, "Ausgewählte kapitel zur Chemometrie in der Prozessanalytik und Probennahme," in *Prozessanalytik*, 1st ed., R. W. Kessler, Ed. Weinheim: Wiley-VCH Verlag GmbH & Co. KGaA, 2006.
- [51] D. B. Todd, "Residence Time Distribution in Twin-Screw Extruders," *Polym. Eng. Sci.*, vol. 15, no. 6, pp. 437–443, 1975.
- [52] G. Taylor, "Dispersion of soluble matter in solvent flowing slowly through a tube," *Proc. R. Soc. Lond. A. Math. Phys. Sci.*, 1953.
- [53] N.-W. Han, J. Bhakta, and R. G. Carbonell, "Longitudinal and lateral dispersion in packed beds: Effect of column length and particle size distribution," *AIChE J.*, vol. 31, no. 2, pp. 277–288, Feb. 1985.
- [54] E. Roblegg, E. Jäger, A. Hodzic, G. Koscher, S. Mohr, A. Zimmer, and J. Khinast, "Development of sustained-release lipophilic calcium stearate pellets via hot melt extrusion.," *Eur. J. Pharm. Biopharm.*, vol. 79, no. 3, pp. 635–45, Nov. 2011.
- [55] K. H. Esbensen and P. Paasch-Mortensen, "Process Sampling: Theory of Sampling - the Missing Link in Process Analytical Technologies (PAT)," in *Process Analytical Technology*, 2nd ed., K. A. Bakeev, Ed. Chichester: John Wiley & Sons Ltd., 2010.
- [56] M. Jamrógiewicz, "Application of the near-infrared spectroscopy in the pharmaceutical technology.," *J. Pharm. Biomed. Anal.*, vol. 66, pp. 1–10, Jul. 2012.